INFORMATION TO USERS

This manuscript has been reproduced from the microfilm master. UMI films the text directly from the original or copy submitted. Thus, some thesis and dissertation copies are in typewriter face, while others may be from any type of computer printer.

The quality of this reproduction is dependent upon the quality of the copy submitted. Broken or indistinct print, colored or poor quality illustrations and photographs, print bleedthrough, substandard margins, and improper alignment can adversely affect reproduction.

In the unlikely event that the author did not send UMI a complete manuscript and there are missing pages, these will be noted. Also, if unauthorized copyright material had to be removed, a note will indicate the deletion.

Oversize materials (e.g., maps, drawings, charts) are reproduced by sectioning the original, beginning at the upper left-hand corner and continuing from left to right in equal sections with small overlaps.

ProQuest Information and Learning
300 North Zeeb Road, Ann Arbor, MI 48106-1346 USA
800-521-0600

UMI®

STRAIN RELAXATION IN INGAASP FILMS ON INP SUBSTRATES

By

XIAOHUA WU, B.ENG.

M.ENG.

A Thesis

Submitted to the School of Graduate Studies

In Partial Fulfillment of the Requirements

For the Degree

Doctor of Philosophy

McMaster University

© Copyright by Xiaohua Wu, July 2000

STRAIN RELAXATION IN INGAASP FILMS ON INP SUBSTRATES

DOCTOR OF PHILOSOPHY (2000) McMaster University

(Materials Science and Engineering) Hamilton, Ontario

TITLE: Strain Relaxation in InGaAsP Films on InP Substrates

AUTHOR: Xiaohua Wu, B.Eng. (Shanghai Jiao Tong University, Shanghai, China)

M.Eng. (Shanghai Jiao Tong University, Shanghai, China)

SUPERVISOR: Professor G.C.Weatherly

NUMBER OF PAGES: xv, 171

Abstract

Transmission electron microscopy (TEM), atomic force microscopy (AFM) and scanning electron microscopy (SEM) have been used to study the strain relaxation mechanisms in $In_{1-x}Ga_xAs_yP_{1-y}$ films grown on (100) InP substrates using gas-source molecular beam epitaxy (MBE).

Highly anisotropic strain relief behavior was found in 2% tensile strained $In_{0.25}Ga_{0.75}As$ and $In_{0.72}Ga_{0.28}P$ films. In the first stages of film growth, the strain in $[0\bar{1}1]$ cross-section was relieved by twinning, while it occurred by cracking in the orthogonal [011] cross-section. In the $In_{0.25}Ga_{0.75}As$ film cracking was a transitory phenomenon. Crack healing was observed in the 500 nm thick film. Cracks were observed to penetrate into the substrate and deviate from an $(0\bar{1}1)$ to $(1\bar{1}1)$ or $(\bar{1}\bar{1}1)$ planes. A critical stress intensity argument was developed to explain substrate cracking. A dislocation analogue for a surface crack was developed to successfully account for the experimental value of the ratio of crack opening displacement to normal surface displacement associated with cracks in $In_{0.72}Ga_{0.28}P$ films.

The 90° partial dislocations were found to form prior to the formation of either cracks and or 60° dislocations in $In_{0.25}Ga_{0.75}As$ films, which is consistent with the critical thickness and nucleation calculations. Elastic strain energy computations show that the 90° partial dislocations also provide the most effective relief of elastic strain energy for films with smaller thickness, while cracks are the most effective strain relaxation mechanism for thicker films. It has also been shown both experimentally and theoretically that the twin thickness increases with an increase in the film thickness.

The free surface plays an important role in determining the equilibrium position of

misfit dislocations in thin epitaxial films. The computations based on a force argument show that the core of the dislocation lies close to the interface when the film is softer than the substrate. On the other hand, when the film is elastically stiffer than the substrate, the core of the dislocation is predicted to lie at some distance from the interface in the softer substrate. This prediction agrees with the experimental observations that the 90° partial dislocations bounded by stacking faults are frequently observed to locate inside the InP substrate over a range of a few hundred angstroms.

The composition modulation in $In_{1-x}Ga_xAs_yP_{1-y}$ films was found to be associated with the chemical spinodal in this alloy. Films with compositions lying within the chemical spinodal at growth temperature show fine scale composition modulation contrast. The composition modulation scales with the size of the strain-induced surface facets.

Acknowledgements

I am grateful to my supervisor, Professor G.C. Weatherly for his guidance and encouragement throughout the Ph.D. program. I have benefited greatly from his scientific stimulation.

I would like to thank Dr. B. Robinson for growing the films used in this study. A. Duft and F. Pearson are acknowledged for their help in atomic force microscope and energy dispersive x-ray analysis.

I would also like to thank Drs. D.S. Wilkinson and J.S. Preston for serving on my Ph.D. supervisory committee.

Special thanks to my wife for her constant support and encouragement.

Table of Contents

Abstract		iii
Acknowledgements		v
Table of contents		vi
List of figures		x
List of tables		xv
Chapter 1	Introduction	1
Chapter 2	Review	7
2.1	Strain relaxation via cracking	7
2.1.1	Critical thickness for the formation of a crack	7
2.1.2	Fracture mechanics of cracks	9
(A)	Single surface crack in the film	11
(B)	Single surface crack penetrating into the substrate	12
(C)	Surface crack array in the film	13
2.1.3	Equilibrium crack spacing	15
2.2	Strain relaxation via plastic flow	16
2.2.1	Misfit dislocations and microtwins	16
2.2.2	Elastic energy of the strained film with misfit dislocations and twins	23
2.2.3	Equilibrium position of misfit dislocations	27
2.3	Surface instability and composition modulation	32
2.3.1	Strain relaxation via surface morphological instability	32
2.3.2	Composition modulation in InGaAsP films	36

Chapter 3	Experimental techniques	39
3.1	Molecular beam epitaxy	39
3.2	Transmission electron microscopy	39
3.2.1	Sample preparation	39
(A)	<011> cross-section TEM sample	40
(B)	(100) plan-view TEM sample	41
3.2.2	TEM diffraction contrast	44
3.2.3	Setting up a two-beam image	46
3.2.4	High-resolution TEM	47
(A)	Phase contrast	47
(B)	The fast Fourier transform (FFT)	49
3.3	Other characterization techniques	49
Chapter 4	Cracking phenomena in $In_{0.25}Ga_{0.75}As$ films on InP substrates	50
4.1	Observations	50
4.2	Discussion	61
4.2.1	Single crack behaviour	64
4.2.2	Multiple cracking and substrate cracking	66
4.2.3	Anisotropy of cracking	68
4.2.4	Crack healing	71
Chapter 5	The surface topography of cracks in strained InGaP films	76
5.1	Observations	76
5.2	Discussion	81
5.2.1	Single crack in an infinite medium	81

5.2.2 Single crack at the film surface 84

Chapter 6 Strain relaxation by 60° perfect dislocation, 90° partial dislocations/twinning and cracking 90

6.1 Observations 90

6.2 Critical thickness for the formation of 60° perfect dislocation, 90° partial dislocation and cracks 96

6.3 Nucleation of 60° perfect dislocation and 90° partial dislocation 99

6.4 Elastic energy of the film with 60° perfect dislocations, 90° partial dislocations and cracks 107

6.5 Strain relaxation via twinning 117

Chapter 7 Equilibrium position of misfit dislocations in thin epitaxial films 123

7.1 Introduction 123

7.2 Force on dislocation 125

7.3 Equilibrium position of misfit dislocation 131

7.4 Application to III-V films 137

Chapter 8 Composition modulations in tensile strained InGaAsP films 141

8.1 Observations 141

8.2 Application of the TEM to composition modulation contrast In III-V compound semiconductors 149

8.3 Composition modulation and surface faceting 154

Chapter 9 Summary and conclusions 157

Appendix The interaction of dislocations with the interface and free surface 159

References 166

List of Figures

Figure 1.1	Composition diagram for $In_{1-x}Ga_xAs_yP_{1-y}$ alloys. Three lines represent the alloy compositions, which are lattice-matched (f = 0), 0.6% tensile strained (f = +0.6%), and 2% tensile strained (f = +2%) to InP. The curves are the chemical spinodal at 480°C. The alloy compositions used for this study are indicated by the solid circles.	4
Figure 2.1	Three modes of fracture: I. opening mode; II. sliding mode; III. tearing mode.	10
Figure 2.2	Geometry of surface cracks: (a) single crack in the film; (b) single crack penetrating into the substrate; and (c) multiple cracks in the film	14
Figure 2.3	Slip on a {111} plane of a zinc-blende type crystal. A perfect (a/2)<110> dislocation can split into two Shockley partial (a/6)<112> dislocations.	19
Figure 2.4	Schematic illustrations of the film with an array of perfect dislocations at the interface (a), an array of partial dislocations at the interface bounding stacking faults (b), and an array of twins comprised of m partials (c).	26
Figure 2.5	Schematic illustration of two semi-infinite media containing a misfit dislocation.	29
Figure 2.6	Strain relaxation by surface morphological instability. (a) An elastic half-plane subjected to tensile stress σ; (b) A square wave surface profile has wavelength λ and amplitude e; (c) A sinusoidal surface $y = e \sin(kx)$ with $k = 2\pi/\lambda$; and (d) A faceted surface.	35
Figure 3.1	Schematic diagram of McMaster GS-MBE system.	40
Figure 3.2	<011> cross-section TEM sample preparation.	42
Figure 3.3	Two-beam conditions of (a) bright field, (b) centered dark field and (c) weak beam dark field images when the objective aperture is on axis.	48
Figure 3.4	Lattice images of two-beam (a), and many-beam (b).	50

Figure 4.1 Cracks in [011] cross-section of 20 nm layer sample. (a) g = $0\bar{2}2$ image showing V-shaped cracks. (b) g = 200 image showing that the strain was relaxed at the tips of cracks but the areas between the crack tips are still strained. (c) HRTEM image of a crack showing that the crack deviates from {011} plane onto the {111} plane after penetrating a distance of 10 – 15 nm into the substrate. 54

Figure 4.2 (100) plan-view image with g = $0\bar{2}2$ of 20 nm layer sample showing dislocations emanating from the crack tips. The dark-light contrast associated with the cracks is caused by surface strain relaxation effects. 56

Figure 4.3 g = 200 dark field image showing planar defects (twins and stacking faults) in $[0\bar{1}1]$ cross-section of 20 nm layer sample. 56

Figure 4.4 SEM images of epilayer surface showing cracks and roughness contrast. The density of cracks decreases with an increase in layer thickness. No cracks were observed in the 500 nm thick layer: (a) h = 20 nm; (b) h = 100 nm; (c) h = 200 nm; and (d) h = 500 nm. 58

Figure 4.5 The change of the structure with the change in layer thickness: (a) h = 20 nm, g = 200; (b) h = 100 nm, g = $0\bar{2}2$; (c) h = 100 nm, g = $0\bar{2}2$; (d) h = 500 nm, g = $0\bar{2}2$. Note the increased dislocation activity seen in [011] cross-section as the film thickness increases. 59

Figure 4.6 STEM image of crack in 100 nm thick sample, showing the total crack length (c) and crack opening (δ_0). The EDX spectrum from region in the substrate of 100 nm thick sample, showing Ga and As signals. 62

Figure 4.7 Plots of ΔE [equation (4.2.9)] vs. c/h at different stress levels for film thickness: (a) h = 20 nm; (b) h = 100 nm; (c) h = 200nm. 70

Figure 4.8 Weak beam dark field images showing a high density of stacking faults and perfect dislocations in 500 nm thick layer: (a) g = $1\bar{1}1$; and (b) g = $0\bar{2}2$. 72

Figure 4.9 SEM image of the surface of 200 nm thick layer showing short cracks and crack terminations. 72

Figure 5.1 g = 400 cross-section TEM images. (a) The crack arrests on $(1\bar{1}1)$ plane after penetrating into substrate along $(0\bar{1}1)$ in $[011]$ cross-section; (b) The crack arrests on $(0\bar{1}\bar{1})$ plane after penetrating into the substrate along $(0\bar{1}1)$ in [011] cross-section; (c) Planar defects and surface undulation in $[0\bar{1}1]$ cross-section. 77

Figure 5.2 AFM image and surface profile. (a) 8 cracks (indicated by arrows) running along [011] direction. The normal surface displacement associated with the cracks is visible. (b) Surface profile along the direction perpendicular to the [011] direction. 79

Figure 5.3 AFM image and surface profile. (a) A crack running along [011] direction. The crack opening displacement is visible. (b) Surface profile along the direction perpendicular to the [011] direction. 80

Figure 5.4 The geometry of the crack in an infinite medium (a); and the dislocation analogue (b). 82

Figure 5.5 The geometry of the surface crack (a); and the dislocation analogue (b). 85

Figure 6.1 The change of the structure with the change in film thickness in $[0\bar{1}1]$ cross-section: (a) h = 10 nm, g = 200; (b) h = 100 nm, g = 200; (c) h = 200 nm, g = 022; (d) h = 500 nm, g = 022. 91

Figure 6.2 HRTEM image of planar defects in $[0\bar{1}1]$ cross-section. (a) HRTEM image, together with the inset FFT image of the area indicated by the box; (b) IFFT image formed using {111} and {200} reflections in FFT image in (a); (c) Enlargement of the area of the tip of planar defect 1. A (a/6)$[2\bar{1}\bar{1}]$ partial dislocation is identified by the Burgers circuit. (d) Geometry of the planar defects 1 and 2 in (a). 94

Figure 6.3 HRTEM image of a twin in 200 nm thick film. The twin thickness is five (111) planes. 95

Figure 6.4 Critical thickness h_c vs. misfit f for a 60° perfect dislocation, a 90° partial dislocation and a crack. 100

Figure 6.5 E_{hl} vs. half-loop radius r for the homogeneous nucleation in the tensile strained film (a) and the compressive strained film (b). 104

Figure 6.6 E_{hl} vs. half-loop radius r for the heterogeneous nucleation in the tensile strained film (a) and the compressive strained film (b). 106

Figure 6.7 The calculation of total elastic energy of the system with 60° perfect dislocation 90° partial dislocation arrays:. (a) E_{total}/E_0 vs. d for h = 100 nm and f = 0.02; (b) d_{eq} vs. h. Solid triangles in (b) are the observed 90° dislocation spacing. 109

Figure 6.8 $(E_{total}/E_0)_{min}$ vs. h for 60° perfect dislocations, 90° partial dislocations + stacking faults and cracks. 111

Figure 6.9 The stress intensity K as a function of s (solid line) for the crack array shown in Fig.2.2c, and two approximate expressions (dot line and dash line). 113

Figure 6.10 The calculation of the total elastic energy of the system with a crack array. (a) E_{total}/E_0 vs. d [equation (6.4.8b)] for h = 100 nm and f = 0.02; (b) d_{eq} vs. h. Solid triangles in (b) are the observed crack spacing. 116

Figure 6.11 The calculation of total elastic energy of the system with twins: $(E_{total}/E_0)_{min}$ vs. twin thickness m for (a) h = 20 nm; (b) h = 100 nm and (c) h = 200 nm and (d) h = 500 nm. 120

Figure 6.12 $(E_{total}/E_0)_{min}$ vs. h for 90° partial dislocations + stacking faults and twins. 121

Figure 7.1 $[0\bar{1}1]$ cross-section TEM bright field image (**g** = 022) of 100 nm thick, 2% tensile strained $In_{0.25}Ga_{0.75}As$ film on InP substrate. The 90° partial dislocations bounded by stacking faults penetrate some distance into the substrate. 124

Figure 7.2 Schematic illustration of film-substrate media containing a misfit dislocation **b**. 126

Figure 7.3 The dependence of dislocation equilibrium position on the ratio of shear modulus at various misfit f. (a) d/b vs. μ_f/μ_s for the isolated dislocation located in the substrate; (b) μ_s/μ_f for the isolated dislocation located in the film. 134

Figure 7.4 The dependence of dislocation equilibrium position on the ratio of shear modulus at various film thickness h. (a) d/b vs. μ_f/μ_s for the isolated dislocation located in the substrate; (b) μ_s/μ_f for the isolated dislocation located in the film. 135

Figure 7.5 Equilibrium position d/h vs. μ_f/μ_s for an edge dislocation (dash-dot line) and a screw dislocation (dash line) lying in the substrate. 136

Figure 7.6 The dependence of the total force (F) on the dislocation position (d) for the isolated 90° dislocation located in the substrate. The solid line: without the force due to stacking fault; the dash line: with the force due to stacking fault. 138

Figure 7.7 Comparison of dependence of the equilibrium position (d/b) on the ratio of shear modulus μ_f/μ_s at various misfit for the isolated dislocation located in the substrate. The dash lines: edge dislocation; the solid lines: 60° dislocation. 140

Figure 8.1 $[0\bar{1}1]$ cross-section TEM images of 0.5 μm thick, 0.6% tensile strained $In_{0.45}Ga_{0.55}As$ film capped by lattice-matched $In_{0.53}Ga_{0.47}As$. **g** = 200 for all images. 142

Figure 8.2 $[0\bar{1}1]$ cross-section TEM images of 2 μm thick, 0.6% tensile strained $In_{0.45}Ga_{0.55}As$ film. **g** = 200 for all images. Note that distance between the top of the image and interface are 1 μm for (d), 1.6 μm for (e) and 2 μm for (f). 146

Figure 8.3 $[0\bar{1}1]$ cross-section TEM image of 0.5 μm thick, 2% tensile strained $In_{0.25}Ga_{0.75}As$ film. **g** = 200. 147

Figure 8.4 $[0\bar{1}1]$ cross-section TEM images of 0.5 μm thick, 2% tensile strained $In_{0.5}Ga_{0.5}As_{0.5}As_{0.5}$ film.(a) **g** = 022; and (b) **g** = 200. 148

Figure 8.5 AFM images showing different surface morphologies of 0.5 μm thick, 2% tensile strained layer of $In_{0.25}Ga_{0.75}As$ (a); and $In_{0.5}Ga_{0.5}As_{0.5}As_{0.5}$ (b). 150

Figure 8.6 $[0\bar{1}1]$ cross-section TEM images of 2 μm thick, 0.6% tensile strained $In_{0.45}Ga_{0.55}As$ film showing microstwins and dislocations.(a) **g** = 022 DF; and (b) **g** = 022 WBDF. 156

Figure A1 A dislocation **b** near an interface. Burgers vector **b** resolved into two components $\mathbf{b}_x$ and $\mathbf{b}_y$. Note that dislocation line direction **l** is taken out of the paper. 160

List of Tables

Table 4.1 Summary of measurement of crack spacing with different layer thickness. 55

Table 4.2 Properties of III-V compounds. 63

Table 5.1 Summary of AFM observations on 100 nm thick $In_{0.72}Ga_{0.28}P$ film. 78

Table 6.1 Summary of measurement of 90° partial dislocation spacing with different film thickness. 96

Table 6.2 The values of the Schmid factor. 103

Table 6.3 Summary of the equilibrium twin thickness m with different film thickness. 118

Table 8.1 The atomic scattering amplitude at $\theta = \theta_B$ for **g** = 200 at 100 kV. 151

Chapter 1

Introduction

The introduction of strain into epitaxial films can lead to enhanced performance in quantum well lasers such as lower threshold currents and higher differential gain due to the strain induced changes in the electronic band structure (Zory 1993). However, the growth of perfect, planar, strained epitaxial films offers a number of interesting materials processing challenges in semiconductor device fabrication before the full benefits of strain may be realized. One of the problems encountered in the growth of lattice-mismatched materials of high structural quality is strain relaxation. The most extensively studied strain relaxation mechanism is plastic flow - the development of misfit dislocations along the substrate - film interface and the formation of microtwins (Frank *et al.* 1949; Matthews and Blakeslee 1974; Wegscheider *et al.* 1989). Recently, a purely elastic strain relaxation mechanism has been demonstrated, both theoretically and experimentally - the strain energy stored in the film can be relaxed by creating surface instabilities (Srolovitz 1989; Grilhe 1993; Okada *et al.* 1997). A third strain relief mechanism in tensile strained layers is cracking (Matthews and Klokhlom 1972; Murray *et al.* 1996; Dieguez *et al.* 1997). The study of strain relaxation mechanisms in heteroepitaxial strained films has been an actively pursued research area and has extended the frontiers of materials science, physics, and semiconductor device performance in the last decade.

In the present thesis, $In_{1-x}Ga_xAs_yP_{1-y}$ ($0 \leq x \leq 1$, $0 \leq y \leq 1$) tensile strained films grown by molecular beam epitaxy (MBE) on (100) InP substrates were chosen for study because of the importance of this system in fiber-optic communication. Throughout this thesis, transmission

electron microscopy (TEM) is most extensively used to characterize strain relaxation related phenomena such as cracking, misfit dislocation, and microtwin formation, surface morphology changes, and composition modulations.

In quaternary $In_{1-x}Ga_xAs_yP_{1-y}$ alloy, the composition of the alloy is specified by only two composition parameters x (Ga content in group III) and y (As content in group V) due to the stoichiometry between group III and group V elements. The composition of an alloy can be represented as a point in the diagram shown in Fig. 1.1. The four corners of the diagram are InP (x = 0, y = 0), InAs (x = 0, y = 1), GaAs (x = 1, y = 1) and GaP (x = 1, y = 0).

$In_{1-x}Ga_xAs_yP_{1-y}$ compounds have the zinc-blende structure with a space group of $F\bar{4}3m$ Z-4. This structure consists of two fcc sublattices that are shifted relative to each other by a quarter of the <111>-body diagonal and then superimposed. Each sub-lattice is occupied by a different group of atoms (i.e. group III or group V). In this structure, only one lattice parameter (a) is needed to determine the unit cell. The lattice constant (a) of $In_{1-x}Ga_xAs_yP_{1-y}$ alloy is known to obey Vegard's law (Nahory *et al.* 1978): i.e. a linear variation of (a) with alloy composition. Throughout this thesis, all other material parameters such as the elastic constants and surface energy of $In_{1-x}Ga_xAs_yP_{1-y}$ alloys are assumed to follow Vegard's law. Vegard's law for any quantity, Q is given by:

$$Q_{In_{1-x}Ga_xAs_yP_{1-y}} = (1-x)(1-y)Q_{InP} + (1-x)yQ_{InAs} + xyQ_{GaAs} + x(1-y)Q_{GaP} \quad (1.1)$$

The materials parameters of any quaternary $In_{1-x}Ga_xAs_yP_{1-y}$ alloy can thus be estimated from data for four binary alloys, which is available in the literature.

The misfit (f) of an $In_{1-x}Ga_xAs_yP_{1-y}$ alloy film on an InP substrate is defined by

$$f = \frac{a_{InP} - a_{In_{1-x}Ga_xAs_yP_{1-y}}}{a_{In_{1-x}Ga_xAs_yP_{1-y}}} \qquad (1.2)$$

where a_{InP} and $a_{In_{1-x}Ga_xAs_yP_{1-y}}$ are the lattice constants of InP and $In_{1-x}Ga_xAs_yP_{1-y}$ in their natural states at room temperature. The lattice constant of $In_{1-x}Ga_xAs_yP_{1-y}$ can be obtained using equation (1.1) with a_{InP} = 5.8688Å, a_{InAs} = 6.0584Å, a_{GaAs} = 5.6533Å and a_{GaP} = 5.4512Å respectively (Adachi, 1982). The thermal mismatch strain on cooling from the growth temperature (480°C) to room temperature (~ 0.05%) is much smaller than the lattice mismatch strain considered in this thesis (f = +2%, +0.6%), so this effect is ignored throughout the thesis. The alloy compositions which are lattice-matched (f = 0), 2% tensile strain (f = +2%), 0.6% tensile strain (f = +0.6%) calculated using equations (1.1) and (1.2) are represented by three lines shown in Fig. 1.1. The chemical spinodal for the $In_{1-x}Ga_xAs_yP_{1-y}$ alloys (discussed in section 2.3.2) at 480° is also shown in Fig.1.1. The compositions used for this study are indicated by the solid circles.

In Chapter 2, the three strain relaxation mechanisms and the origin of the composition modulations are reviewed. Chapter 3 briefly describes the experimental techniques used in this thesis. Experimental results and discussion are presented in Chapters 4, 5, 6, 7, and 8. Chapter 9 summarizes the contribution of this thesis.

In Chapter 4, the strain relaxation of a series of $In_{0.25}Ga_{0.75}As$ films grown on (100) InP substrates (lattice mismatch f = +2%) has been studied. The mechanisms of strain relief (in the first stages of growth) occurred by cracking on $(0\bar{1}1)$, and by twinning on (111) and $(\bar{1}11)$ planes. Cracking was a transitory process with the density of cracks being highest in a

Figure 1.1

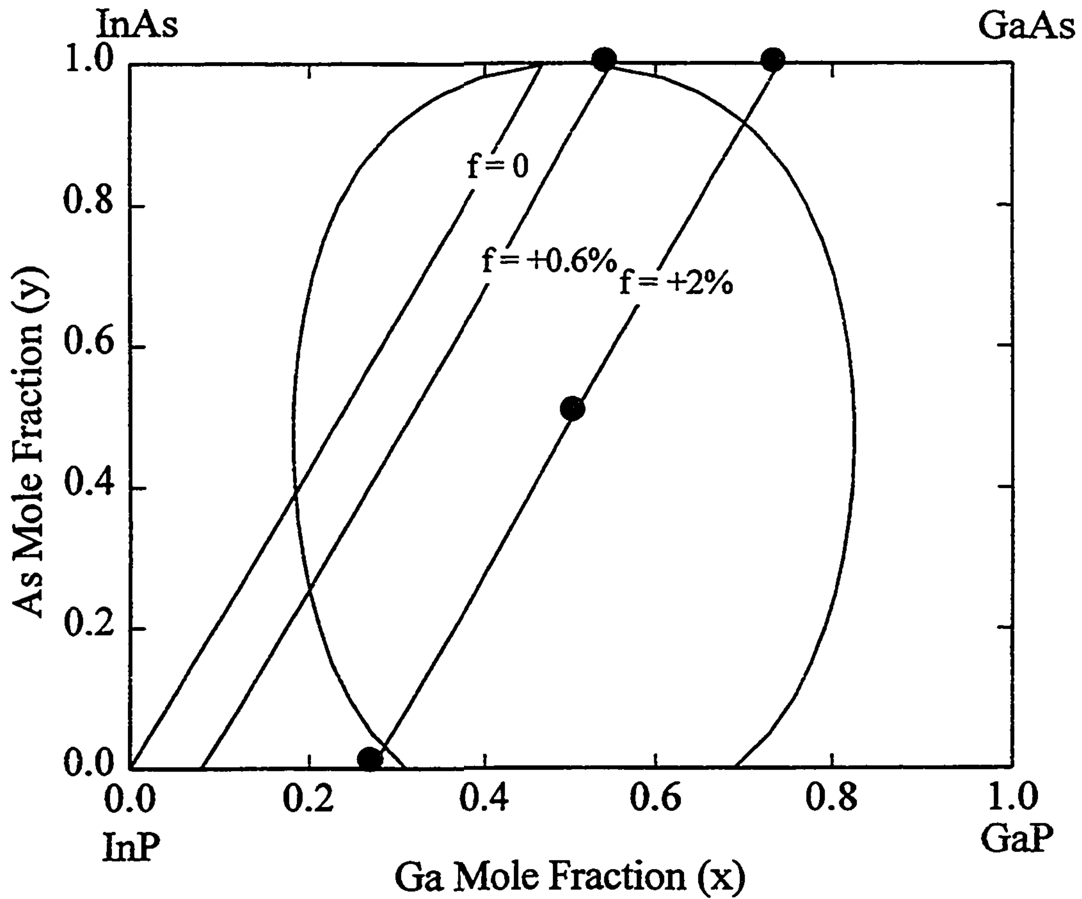

Composition diagram for $In_{1-x}Ga_xAs_yP_{1-y}$ alloys. Three lines represent the alloy compositions which are lattice-matched (f = 0), 0.6% tensile strained (f = +0.6%), and 2% tensile strained (f = +2%) to InP. The curves are the chemical spinodal at 480°C. The alloy compositions used for this study are indicated by the solid circles.

20 nm thick film, while a 500 nm thick film was crack-free. These results are discussed in the context of different cracking models.

In Chapter 5, cracks in a 2% tensile strained $In_{0.72}Ga_{0.28}P$ film grown on an InP substrate were studied. A dislocation analogue (i.e. replacing the crack by an array of equivalent infinitesimal edge dislocations) is employed to account for the ratio of the crack opening displacement to the normal surface displacement associated with the crack.

In Chapter 6, the comparison of strain relaxation via cracking, 60° perfect dislocations and 90° partial dislocations/twinning are presented. It has been shown both experimentally and theoretically that 90° partial dislocations are formed prior to the formation of cracks and 60° dislocations. 90° partial dislocations also provide a most effective relief of elastic strain energy for the film with smaller thickness, while cracks are the most effective strain relaxation mechanism for thicker films. In addition, the twin thickness is found to increase with an increase in the film thickness. The latter experimental result has also been theoretically predicted.

Chapter 7 describes theoretical work considering the role of the free surface in determining the equilibrium position of misfit dislocations in thin epitaxial films. When the film is elastically stiffer than the substrate, the core of the dislocation is predicted to lie at some distance from the interface in the softer substrate. On the other hand when the film is softer than the substrate, the core of the dislocation is always predicted to lie close to the interface.

In Chapter 8, the correlation between compositional modulations and surface morphology has been studied. The experimental results are discussed in terms of the role of

stress in promoting faceting and the position of the film composition relative to the chemical spinodal in the quaternary In-Ga-As-P system.

Chapter 2

Review

2.1 Strain relaxation via cracking

2.1.1 Critical thickness for the formation of a crack

Strain relaxation by cracking was first reported in 1972 (Matthews and Elokholm 1972), but very few studies have been done on the cracking mechanism. Only recently has cracking in III-V epilayers attracted more attention due to the increasing technological interest in growing highly strained structures (Tsuchiya *et al.* 1994; Murray *et al.* 1996; Dieguez *et al.* 1997).

Consider an x, y, z - coordinate system in which the x-axis is parallel to the growth direction and the plane containing the y and z-axes is parallel to the film- substrate interface plane. If the film thickness is much less than the thickness of the substrate, all the misfit is confined in the film. The film is then under biaxial strain $\varepsilon_{yy} = \varepsilon_{zz} = f$ where f is the misfit. Since $\sigma_{xx} = 0$, the strain in the growth direction of the film is derived for an isotropic material as $\varepsilon_{xx} = -2\nu f/(1-\nu)$ where ν is the Poisson's ratio. The biaxial stresses in the film are

$$\sigma_{yy} = \sigma_{zz} = 2\mu \frac{1+\nu}{1-\nu} f \qquad (2.1.1)$$

where μ is the shear modulus.

For cracks to propagate in the film, the film thickness must exceed the Griffith crack length. The relationship between the tensile stress σ perpendicular to the crack plane and the Griffith crack length, h_g, is given by (Lawn 1993)

$$\sigma = \sqrt{\frac{2E\gamma}{\pi h_g}} = \sqrt{\frac{4\mu(1+\nu)\gamma}{\pi h_g}} \qquad (2.1.2)$$

where E = 2μ(1+ν) is the Young's modulus, and γ is the surface energy of the crack. Substituting equation (2.1.1) into equation (2.1.2), the following expression for the critical thickness for the formation of the crack is obtained (Matthews and Klokholm 1972):

$$h_c = \frac{(1-\nu)^2\gamma}{\pi\mu(1+\nu)f^2} \qquad (2.1.3)$$

Equation (2.1.3) was found to agree well with the experimental results of yttrium iron garnet films grown an rare earth-gallium or aluminum garnet substrates (Besser *et al.* 1971).

Murray *et al.* (1996) studied crack formation in $In_x(GaAl)_{1-x}As$ epilayers grown under tension on an InP (001) substrate. They proposed the following simple theoretical model based on an energy balance criterion to predict the critical thickness for crack initiation. The elastic energy per unit length relieved by the crack is given by (Murray *et al.* 1996):

$$E_e = 2\mu\frac{1+\nu}{1-\nu}f^2h^2 \qquad (2.1.4)$$

The surface energy per unit length increased by the formation of crack surfaces is

$$E_s = 2\gamma h \qquad (2.1.5)$$

The critical thickness is obtained by setting $E_e = E_s$, giving (Murray *et al.* 1996)

$$h_c = \frac{(1-\nu)\gamma}{\mu(1+\nu)f^2} \qquad (2.1.6)$$

The elastic energy relieved per unit length of crack given by equation (2.1.4) is rather arbitrary. The authors simply assumed that only energy stored within a range h of the crack is relieved (where h is the crack length). The fracture mechanics calculation developed in

Chapter 4 shows that equation (2.1.4) underestimates the elastic energy relieved by the crack. In Chapter 4, a critical thickness for the formation of cracks in thin films is derived based on a fracture mechanics approach.

2.1.2 Fracture mechanics of cracks

There are three basic modes of crack surface displacement, as shown in Fig. 2.1. Mode I (opening mode) corresponds to a normal separation of the crack walls under the action of tensile stresses; mode II (sliding mode) corresponds to longitudinal shearing of the crack walls in a direction normal to the crack front; mode III (tearing mode) corresponds to lateral shearing parallel to the crack front. Obviously, it is a very good assumption that cracks in tensile strained films are subjected to pure mode I loading if the crack is perpendicular to the stress axis. The stress fields at the tip of a crack subjected to mode I loading in plane stress or plane strain for a homogeneous, isotropic elastic solid are given by

$$\sigma_{ij} = \frac{K}{\sqrt{2\pi r}} f_{ij}(\theta) \qquad (2.1.7)$$

where r and θ are polar coordinates centered at the crack tip, $f_{ij}(\theta)$ is a function of θ, given in many texts on fracture, and K is the stress intensity factor. Throughout the thesis, K instead of K_I is used to indicate mode I stress intensity factor since only mode I crack is considered in this thesis

The elastic energy release rate is denoted by G. Physically, G may be viewed as the energy made available for the crack extension processes at the crack tip, as a result of the work from displacements of the loading force and/or reductions in strain energy in a body

Figure 2.1

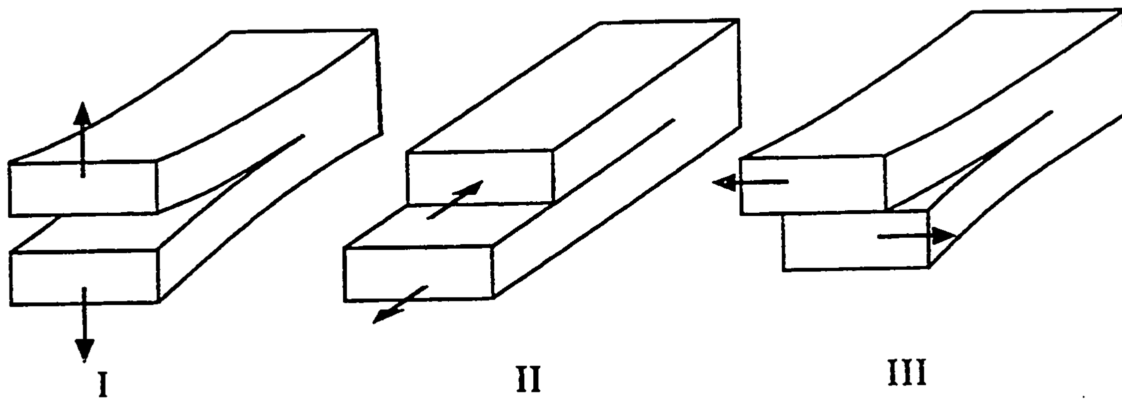

The three modes of fracture: I. opening mode; II. sliding mode; III. tearing mode.

accompanying a unit increase in crack area. The relation between G and K is given by (Tada *et al.* 1985; Hutchinson and Suo 1992; Lawn 1993):

$$G = \frac{K^2}{\overline{E}} \tag{2.1.8}$$

where $\overline{E} = E$ for plane stress, $\overline{E} = E/(1-\nu^2)$ for plane strain and E is Young's modulus. Therefore, if an expression for K is available, the total elastic energy relieved by cracks (E_e) along the crack propagation direction x can be calculated as

$$E_e = \int G dx = \int \frac{K^2}{\overline{E}} dx \tag{2.1.9}$$

The total elastic energy relieved by cracks along a crack propagation direction x could also be calculated as (Ye *et al.* 1992)

$$E_e = \frac{\sigma}{2} \int \delta(x) dx \tag{2.1.10}$$

where δ(x) is the crack opening displacement, and the integral is taken over the surface of the crack.

The values of K and the crack opening displacement for various surface cracks are given by Tada *et al.* (1985) and can be summarized as follows.

(A) Single surface crack in the film (Fig. 2.2a)

$$K = 1.122\sigma\sqrt{\pi c} \tag{2.1.11}$$

Crack opening area (shadow area in Fig.2.2a):

$$A = 1.258\frac{\sigma\pi c^2}{\overline{E}} \tag{2.1.12}$$

Crack profile:

$$\delta(x) = \frac{4\sigma}{\overline{E}}\sqrt{c^2 - x^2}\,D\left(\frac{x}{c}\right) \tag{2.1.13}$$

$$\text{where } D\left(\frac{x}{c}\right) = 1.454 - 0.727\left(\frac{x}{c}\right) + 0.618\left(\frac{x}{c}\right)^2 - 0.224\left(\frac{x}{c}\right)^3 \tag{2.1.14}$$

Thus, the crack opening displacement at the free surface is

$$\delta_0 = \delta(0) = 1.454\frac{4\sigma c}{\overline{E}} \tag{2.1.15}$$

(B) Single surface crack penetrating into the substrate (Fig. 2.2b)

$$K = \sigma\sqrt{\pi c}\,\frac{2}{\pi}\sin^{-1}\left(\frac{h}{c}\right)F\left(\frac{h}{c}\right) \tag{2.1.16}$$

$$\text{where } F\left(\frac{h}{c}\right) = 1.3 - 0.18\left(\frac{h}{c}\right)$$

Crack opening area (shadow area in Fig.2.2b):

$$A = \frac{\sigma\pi c^2}{\overline{E}}\frac{2}{\pi}\left[\sin^{-1}\left(\frac{h}{c}\right) + \frac{h}{c}\sqrt{1-\left(\frac{h}{c}\right)^2}\right]G\left(\frac{h}{c}\right) \tag{2.1.17}$$

$$\text{where } G\left(\frac{h}{c}\right) = 1.258 + 0.196\left(1 - \frac{h}{c}\right)^{(5/2)}$$

Crack opening at free surface:

$$\delta_0 = \frac{4\sigma c}{\overline{E}}\frac{2}{\pi}\left[\sin^{-1}\left(\frac{h}{c}\right) + \frac{h}{c}\cosh^{-1}\left(\frac{c}{h}\right)\right]H_0\left(\frac{x}{c}\right) \tag{2.1.18}$$

$$\text{where } H_0\left(\frac{h}{c}\right) = 1.681 - 0.227\left(\frac{h}{c}\right)\left[1 + \left(1 - \frac{h}{c}\right)\left(\frac{h}{c}\right)^{(-3/4)}\right]$$

Crack opening at interface:

$$\delta_b = \frac{4\sigma c}{E}\frac{2}{\pi}\left[\sqrt{1-\left(\frac{h}{c}\right)^2}\sin^{-1}\left(\frac{h}{c}\right) - \frac{h}{c}\ln\left(\frac{h}{c}\right)\right]H_b\left(\frac{x}{c}\right) \qquad (2.1.19)$$

where $H_b\left(\frac{h}{c}\right) = 1.681 - \left[1 - 0.215\left(\frac{h}{c}\right)^{0.320}\left(1-\frac{h}{c}\right)^{0.565}\right]$

(C) Surface crack array in the film (Fig. 2.2c)

The stress intensity factor is given as a function of s, where s = 2c/(2c+d) (Bowie 1973):

$$K = Q(s)\sqrt{1-s}\sigma\sqrt{\pi c} \qquad (2.1.20)$$

with

$$Q(s) = \frac{1}{\sqrt{\pi}}\left[1 + \frac{1}{2}(1-s) + \frac{3}{8}(1-s)^2 + \frac{5}{16}(1-s)^3 + \frac{25}{128}(1-s)^4 + \frac{63}{256}(1-s)^5 + \frac{231}{1024}(1-s)^6\right]$$
$$+22.501(1-s)^7 - 63.502(1-s)^8 + 58.045(1-s)^9 - 17.577(1-s)^{10} \qquad (2.1.21)$$

It has been shown (Tada *et al.* 1985) that the stress intensity factor K can be approximately expressed by a simple function for $d \le 5c$, i.e. $0.29 \le s \le 1$ as follows

$$K = \sqrt{\frac{1-s}{\pi s}}\sigma\sqrt{\pi c}, \quad 0.29 \le s \le 1, \text{ i.e. } d \le 5c \qquad (2.1.22)$$

Following this approximation, Thouless (1990) and Thouless *et al.* (1992) used two expressions for K for the multiple crack case in a study of the equlibrium crack spacing in brittle films.

$$K = 1.122\sigma\sqrt{\pi c}, \quad 0 \le s \le 0.2, \text{ if } d \ge 8c$$

$$K = \sqrt{\frac{1-s}{\pi s}}\sigma\sqrt{\pi c} \quad 0.2 \le s \le 1, \text{ if } d \le 8c \qquad (2.1.23)$$

Figure 2.2

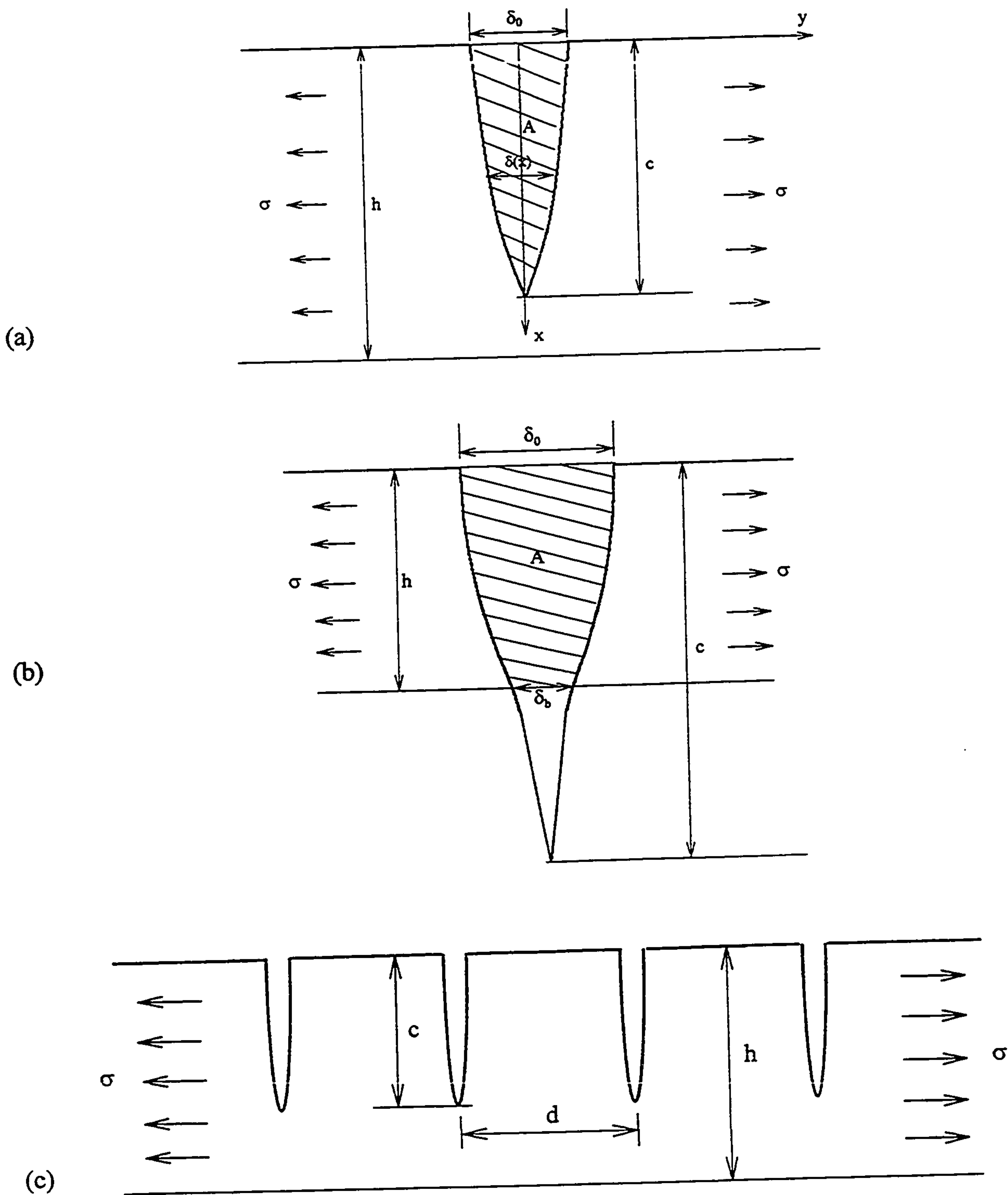

Geometry of surface cracks. (a) Single crack in the film, (b) Single crack penetrating into the substrate, and (c) Multiple cracks in the film.

A more accurate expression for K for $d \geq 5c$ is given in Chapter 6. In Chapter 5, a dislocation analogue (i.e. replacing the crack by an array of equivalent infinitesimal edge dislocations) is employed to account for the ratio of the crack opening displacement to the normal surface displacement associated with the crack. Some comparisons of recent results from the dislocation analogue (Gao *et al.* 1999) with classical fracture mechanics is presented in Chapter 5 as well.

2.1.3 Equilibrium crack spacing

Consider a surface crack array with spacing d in the film (Fig.2.2c). The elastic energy per unit area relieved by cracks terminated at the interface can be calculated using equations (2.1.8), (2.1.9) and (2.1.23), giving (Thouless 1990; Thouless *et al.* 1992)

$$E_e = 1.98\frac{\sigma^2 h^2}{\bar{E}d}, \qquad d \geq 8h$$

$$E_e = \frac{\sigma^2}{\bar{E}d}\left(\frac{d}{2}h - 0.0316d^2\right), \qquad d \leq 8h \qquad (2.1.24)$$

The total energy per unit area in the film is given by

$$E_{total} = E_0 - E_e + E_s \qquad (2.1.25)$$

where $E_0 = \frac{\sigma^2 h}{2\bar{E}}$ is the strain energy per unit area in the uncracked film and $E_s = \frac{\Gamma_f h}{d}$ is the energy per unit area assuming the mode I fracture resistance is Γ_f (Thouless *et al.* 1992). In a purely elastic fracture process $\Gamma_f = 2\gamma$, where γ is the surface energy of the cracks. The first expression in equation (2.1.24) holds for the single surface crack case, i.e. the cracks making up the array are assumed not to interact with each other when they are separated by more than

8 times the film thickness. The second expression in equation (2.1.24) can be used to study the equilibrium crack spacing d_{eq}. The value of d_{eq} can be obtained by solving $(\partial E_{total}/\partial d) = 0$, giving (Thouless *et al.* 1992)

$$d_{eq} = 5.6\sqrt{\frac{\Gamma_f h\bar{E}}{\sigma^2}} \qquad (2.1.26)$$

Equation (2.1.26) predicts that the equilibrium crack spacing increases as $h^{1/2}$, which implies that the density of cracks decreases with an increase in the film thickness. The relationship between d_{eq} and h predicted by equation (2.1.26) is well confirmed by the experimental results of [110] $PrBa_2Cu_3O_{7-x}$ films grown on [110] $SrTiO_3$ substrates (Thouless *et al.* 1992). In Chapter 4, Thouless's approach is adopted to predict the cracking phenomena found in InGaAs films grown on InP substrates and the crack density change with change in the film thickness is discussed in relation to the experimental results.

2.2 Strain relaxation via plastic flow

2.2.1 Misfit dislocations and microtwins

In the zinc-blende structure of $In_{1-x}Ga_xAs_yP_{1-y}$, the usual slip systems are (a/2)<110>{111}, i.e. perfect dislocations have Burgers vector **b** = (a/2)<110>. For a lattice-mismatched $In_{1-x}Ga_xAs_yP_{1-y}$ film grown on a (100) InP substrate, {111} slip planes make [011] or $[0\bar{1}1]$ intersections with the interface; thus, misfit dislocations at the interface typically form a cross grid configuration along these directions.

The three main types of perfect dislocations with Burgers vector **b** = (a/2)<110> are edge-, screw, and 60°-mixed dislocations. The Burgers vectors of edge type dislocations do

not lie on the slip plane; they would be sessile and must move by climb. This edge type dislocation also has the highest core energy. The screw type dislocation cannot relieve tetragonal mismatch. Therefore, the 60° dislocation is the most probable type of misfit dislocation in this structure (Maree *et al.* 1987; Hull and Bean 1992).

The misfit dislocations can be brought about either by glide of grown-in threading dislocations (Matthews and Blakeslee 1974) or by the nucleation of dislocation half loops at the film surface and expansion to the interface (Maree *et al.* 1987). The early studies assumed that all misfit dislocations were formed via threading dislocations. This may have been a reasonable assumption for semiconductor substrates in the 1970's. With the increasing purity of semiconductor substrates, there are no significant dislocations pre-existing in the substrate. The density of pre-existing threading dislocations is too low to act as a substantial source of misfit dislocation for contemporary substrates. Therefore, the nucleation and expansion of dislocation half-loops becomes a dominant mechanism for the formation of misfit dislocations in high misfit systems (Maree *et al.* 1987; Fitzgerald *et al.* 1989).

It is well known that, in semiconductor materials, a perfect dislocation generally dissociates into two partials separated by a stacking fault. In the zinc-blende structure, slip occurs in {111} close-packed planes and the slip direction is <110>. The slip involves the sliding of close-packed planes of atoms over each other. Close-packed {111} planes simulated by a set of hard spheres are schematically shown in Fig.2.3. One {111} layer is represented by the full circles, A, and the second identical {111} layer above the A plane locates in the sites marked B. Consider the movement of the layers when they are sheared over each other to produce a displacement in the slip direction. It will be found that the B

layer of atoms, instead of moving from one B site to the next B site over the top of the A atoms, will move first to the nearby C site along the "valley" between the two A atoms and then to the new B site via a second valley. The unit lattice displacement $\mathbf{b}_1$ is achieved by two movements represented by vectors $\mathbf{b}_2$ and $\mathbf{b}_3$. The perfect dislocation with Burgers vector $\mathbf{b}_1$ therefore dissociates into two partial dislocations $\mathbf{b}_2$ and $\mathbf{b}_3$ with a stacking fault between them according to the reaction:

$$\mathbf{b}_1 \rightarrow \mathbf{b}_2 + \mathbf{b}_3$$

or $$\frac{a}{2}\langle 110\rangle \rightarrow \frac{a}{6}\langle 211\rangle + \text{Stacking Fault} + \frac{a}{6}\langle 12\bar{1}\rangle \qquad (2.2.1)$$

For a perfect 60° dislocation with $\mathbf{b}_1 = \frac{a}{2}[10\bar{1}]$ and line direction $\mathbf{u} = [0\bar{1}1]$ on (111) slip plane, equation (2.2.1) becomes

$$\frac{a}{2}[10\bar{1}] \rightarrow \frac{a}{6}[2\bar{1}\bar{1}] + \text{Stacking Fault} + \frac{a}{6}[11\bar{2}] \qquad (2.2.2)$$

where $\mathbf{b}_2 = \frac{a}{6}[2\bar{1}\bar{1}]$ is a 90° Shockley partial, and $\mathbf{b}_3 = \frac{a}{6}[11\bar{2}]$ is a 30° Shockley partial.

The nucleation of dislocation half-loops at the film surface thus has three possibilities: (i) nucleation of 60° perfect dislocation half-loops, (ii) nucleation of 90° partial dislocation half-loops, and (iii) nucleation of 30° partial dislocation half-loops. Several studies has considered the homogeneous nucleation of dislocation half-loop at a free surface. The change in energy on the introduction of a half-loop of radius r in strained layer is given by (Maree *et al.* 1987; Hull and Bean 1992; Zou and Cockayne 1996)

$$E_{hl} = E_l \pm E_s \pm E_\gamma - E_\tau \qquad (2.2.3)$$

Figure 2.3

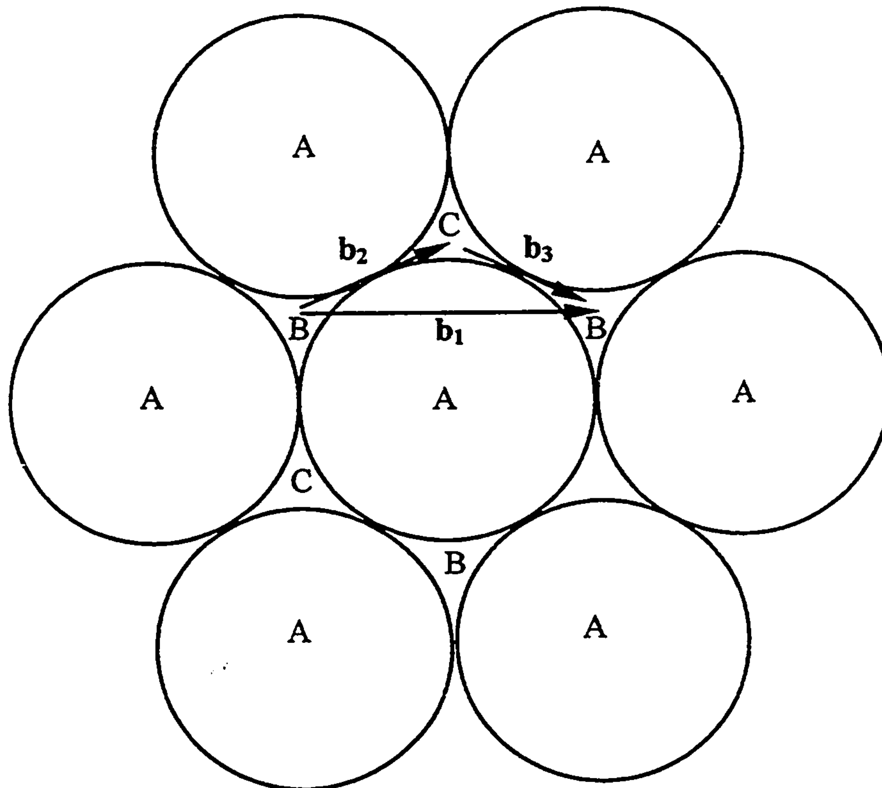

Slip on a {111} plane of a zinc-blende type crystal. A perfect (a/2)<110> dislocation can split into two partial (a/6)<112> dislocations. (after Maree *et al.* 1987; Petruzzelo and Leys 1988)

where E_l is the self-energy of a half-loop of length πr, and E_s is the energy associated with the removal or creation of a surface step. The contribution of the stacking fault energy E_γ is positive, negative, or zero, depending on whether the fault is created (leading partial), annihilated (trailing partial), or not formed at all (perfect dislocation). E_τ is the strain energy released by the loop. This change in energy may be written as

$$E_{hl} = \left[\frac{\mu b^2 r(1-\nu/2)}{4(1-\nu)}\right]\ln\left(\frac{\alpha r}{b}\right) \pm 2rb\gamma\sin\theta \pm \frac{1}{2}\pi r^2 \gamma_{S.F.} - \frac{1}{2}\pi r^2 \tau b \tag{2.2.4}$$

where μ is the shear modulus, b is the magnitude of the Burgers vector, ν is Poisson's ratio, α is the dislocation core parameter, γ is the surface energy, θ is the angle between the dislocation Burgers vector and the free surface, $\gamma_{S.F.}$ is the stacking fault energy, and τ is the shear stress resolved on the slip plane in the slip direction. Equation (2.2.3) has been used in Chapter 6 of this thesis to compute the heterogeneous nucleation of a dislocation half-loop at the 2% tensile strained $In_{0.25}Ga_{0.75}As$ film surface, including also the effect associated with a stress concentration in an "undulated" film surface.

The energy E_{hl} increases for small r, reaches a maximum $E_{hl,c}$ when dE/dr = 0 at the critical r_c, and then decreases while the loop expands further. Neglecting the step energy term, the critical radius and the maximum energy (or energy barrier) are given by:

$$r_c = \frac{1}{\tau b \pm \gamma_{S.F.}} \frac{\mu b^2 (1-\nu/2)}{4\pi(1-\nu)}\left[1 + \ln\left(\frac{\alpha r_c}{b}\right)\right] \tag{2.2.5}$$

and

$$E_{hl,c} = r_c\left\{\frac{\mu b^2(1-\nu/2)}{8(1-\nu)}\left[-1+\ln\left(\frac{\alpha r_c}{b}\right)\right]\right\} \qquad (2.2.6)$$

Since $E_{hl,c}$ varies as b^3, there is a strong tendency for the loop to decompose into two partials bounding a stacking fault. The computation on the nucleation of a dislocation half-loop at the surface of tensile strained $In_{0.25}Ga_{0.75}As$ films (presented in Chapter 6 of this thesis) also demonstrates that the nucleation of a partial dislocation half-loop is energetically more favorable than the nucleation of a perfect dislocation.

It has been shown experimentally that the 90° partial is the leading dislocation and the 30° partial is the trailing dislocation in tensile strained film, while the 30° partial is the leading dislocation and the 90° partial is the trailing dislocation in a compressively strained layer (Maree *et al.* 1987; Petruzzello and Leys 1988). Therefore, 90° partials nucleate first and expand to the interface position in a tensile strained layer. The strain in the layer is now relieved by 90° partial interfacial misfit dislocations. More importantly, twins will form by the repeated nucleation of 90° partial dislocations according to the following mechanism.

The {111} slip plane stacking sequence corresponding to a perfect zinc-blende structure is

$$\cdots A\,B\,C\,A\,B\,C\,A\,B\,C\cdots \qquad (2.2.7)$$

as shown in Fig.2.3. Assume that $\mathbf{b}_1 = \frac{a}{2}[10\bar{1}]$, $\mathbf{b}_2 = \frac{a}{6}[2\bar{1}\bar{1}]$, $\mathbf{b}_3 = \frac{a}{6}[11\bar{2}]$ and $\mathbf{u} = [0\bar{1}1]$ in Fig.2.3. If the B plane and all planes above it are displaced by the vector $\mathbf{b}_2 = \frac{a}{6}[2\bar{1}\bar{1}]$, the B plane moves into a C position, and the planes above it undergo the transition A $\rightarrow$ B, B $\rightarrow$ C,

and C → A, relative to positions fixed on the original A plane. This shear displacement is represented by the arrows in the reaction:

(2.2.8)

giving

(2.2.9)

The resultant fault is an intrinsic stacking fault because the sequence is the same as a layer of atoms (B) being removed from the normal sequence (2.2.7).

If the displacement $\frac{a}{6}[2\bar{1}\bar{1}]$ is continued plane by plane above,

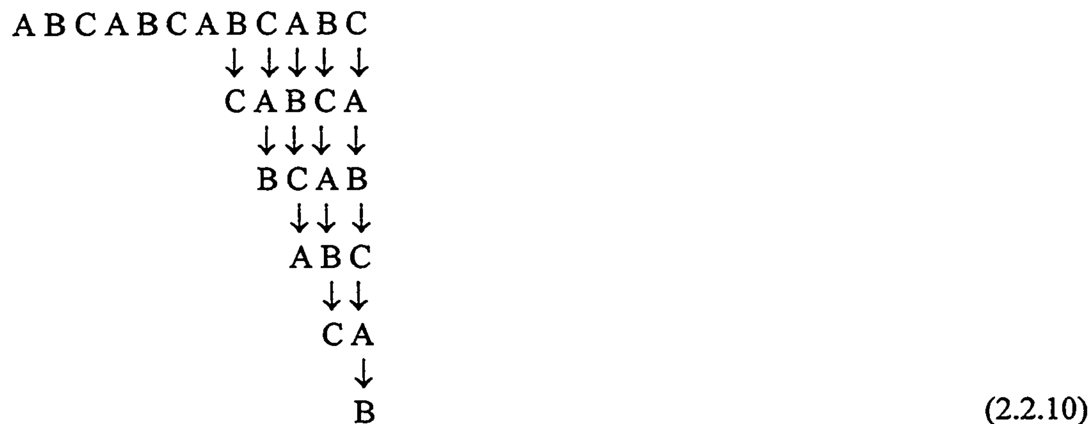

(2.2.10)

giving

(2.2.11)

Obviously, the new stacking sequence (2.2.11) is a twin with a A layer indicated by the line as a mirror plane.

The above mechanism for the formation of a twin has been observed in the tensile strained Si-Ge system (Wegscheider *et al.* 1990): a 90° Shockley partial dislocation half-loop

nucleates at the surface and glides on a {111} plane towards the thin film-substrate interface. As the dislocation is imperfect, an intrinsic stacking fault is produced. If another half loop of the 90° partial type is formed on an adjacent glide plane, this second 90° partial dislocation will glide down to the interface to relieve the misfit strain. The consequent continuation of this process leads finally to the formation of a twin as demonstrated by (2.2.10) and (2.2.11).

2.2.2 Elastic energy of the strained film with misfit dislocations and twins

A number of authors have considered the problem of finding the total elastic strain energy of a partially dislocated thin film (Willis *et al.* 1990; Jain *et al.* 1992; Dynna *et al.* 1994). Here we follow the approach of Dynna *et al.* (1994) who computed the total elastic energy of the strained film with misfit dislocations. For the array of mixed dislocations shown in Fig.2.4a, the total elastic energy per unit area of the system is given by:

$$E_{total} = E_0 + E_{disl} + E_{int,\,disl/film} + E_{int,\,disl/disl} \tag{2.2.12}$$

with

$$E_0 = 2\mu\frac{1+\nu}{1-\nu}f^2h \tag{2.2.13}$$

$$E_{disl} = \frac{1}{d}\left\{\frac{\mu b^2\left(1-\nu\cos^2\beta\right)}{4\pi(1-\nu)}\ln\left(\frac{2h}{r_0}\right)+\frac{\mu b^2\sin^2\beta}{8\pi(1-\nu)}\left[\cos^2\varphi-\sin^2\varphi-\frac{(1-2\nu)}{2(1-\nu)}\right]+U_{core}\right\} \tag{2.2.14}$$

$$E_{int,disl/film} = -\frac{2\mu(1+\nu)|f|hb\sin\beta\cos\varphi}{(1-\nu)d} \tag{2.2.15}$$

$$E_{int,disl/disl} = \frac{\mu b^2(1-\nu\cos^2\beta)}{4\pi(1-\nu)d}\left[\frac{d}{2\pi h}\sinh\left(\frac{2\pi h}{d}\right)\right]$$

$$+\frac{\mu b^2\sin^2\beta\cos^2\varphi}{4\pi(1-\nu)d}\left[\frac{2\pi h}{d}\coth\left(\frac{2\pi h}{d}\right)-\frac{2\pi^2h^2}{d^2}\operatorname{csch}^2\left(\frac{2\pi h}{d}\right)-\frac{1}{2}\right]$$

$$-\frac{\mu b^2\sin^2\beta\sin^2\varphi}{4\pi(1-\nu)d}\left[\frac{2\pi h}{d}\coth\left(\frac{2\pi h}{d}\right)+\frac{2\pi^2h^2}{d^2}\operatorname{csch}^2\left(\frac{2\pi h}{d}\right)-\frac{3}{2}\right]$$

(2.2.16)

In equation (2.2.12), E_0 is the energy per unit area of the film, E_{disl} is the energy per unit area of the dislocation array, neglecting interactions between dislocations, $E_{int,disl/film}$ is the interaction energy per unit area between the dislocation array and the film, and $E_{int,disl/disl}$ is the interaction energy per unit area between the dislocations which make up the array. In the expression for the four energy terms, μ is the shear modulus, ν is the Poisson's ratio, f is the misfit, h is the film thickness, β is the angle between the Burgers vector of the dislocation and the dislocation line, φ is the angle between the slip plane and the free surface, d is the dislocation spacing as shown in Fig.2.4, r_0 is the dislocation core radius, and U_{core} is the energy per unit length of the dislocation core.

For the array of 90° partial dislocations bounded by stacking faults shown in Fig.2.4b, the total elastic energy per unit area of the system should also include the stacking fault energy term

$$E_{S.F.} = \frac{\gamma_{S.F.}h}{d\sin\varphi} \qquad (2.2.17)$$

where $\gamma_{S.F.}$ is the stacking fault energy of the film.

At a given value of film thickness, there is an equilibrium dislocation spacing d_{eq} at which the energy reaches the minimum. d_{eq} can be obtained by solving $(\partial E_{total}/\partial d) = 0$.

As shown in section 2.2.1, twins can be formed by the successive glide of 90° partial dislocation on adjacent {111} planes (Fig. 2.4c). In this case, the total elastic energy per unit area of the system is given by (Dynna *et al.* 1997):

$$E_{total} = E_0 + E_{twin} + E_{int,\,twin/film} + E_{int,\,twin/twin} \qquad (2.2.18)$$

In this equation, E_0 is the energy per unit area of the film given by equation (2.2.13). E_{twin} is the self-energy per unit area of the twins, neglecting interactions between twins, $E_{int,twin/film}$ is the interaction energy per unit area between the twins and the film, and $E_{int,twin/twin}$ is the interaction energy per unit area between the twins.

E_{twin} can be calculated by first summing the interaction energies existing between the m partials that make up each twin using the method described in Dynna *et al.* (1994). This term is then added to twice the twin boundary energy and m times the self-energy of a 90° (a/6)<211> partial dislocation calculated by equation (2.2.14). Following this procedure, E_{twin} is given by

$$E_{twin} = \frac{1}{d}\left\{\frac{m\mu b^2(1-\nu\cos^2\beta)}{4\pi(1-\nu)}\ln\left(\frac{2h}{r_0}\right) + \frac{m\mu b^2\sin^2\beta}{8\pi(1-\nu)}\left[\cos^2\varphi - \sin^2\varphi - \frac{1-2\nu}{2(1-\nu)}\right] + mU_{core} + \frac{2\gamma_T h}{\sin\varphi}\right\}$$

$$\frac{1}{d}\left\{\frac{\mu b^2}{4\pi(1-\nu)}\sum_{k=1}^{m}(m-k)\left[(1-\nu\cos^2\beta)\ln\left(1+\frac{4h^2}{k^2 d_p^2}\right) + \sin^2\beta\sin^2\varphi\frac{12k^2 d_p^2 h^2 + 16h^4}{(k^2 d_p^2 + 4h^2)^2} - \sin^2\beta\sin^2\varphi\frac{4k^2 d_p^2 h^2 + 48h^4}{(k^2 d_p^2 + 4h^2)^2}\right]\right\}$$

(2.2.19)

where γ_T is the twin boundary energy, and $d_p = d_{111}/\sin\varphi$ is the spacing of partials making up the twin.

Figure 2.4

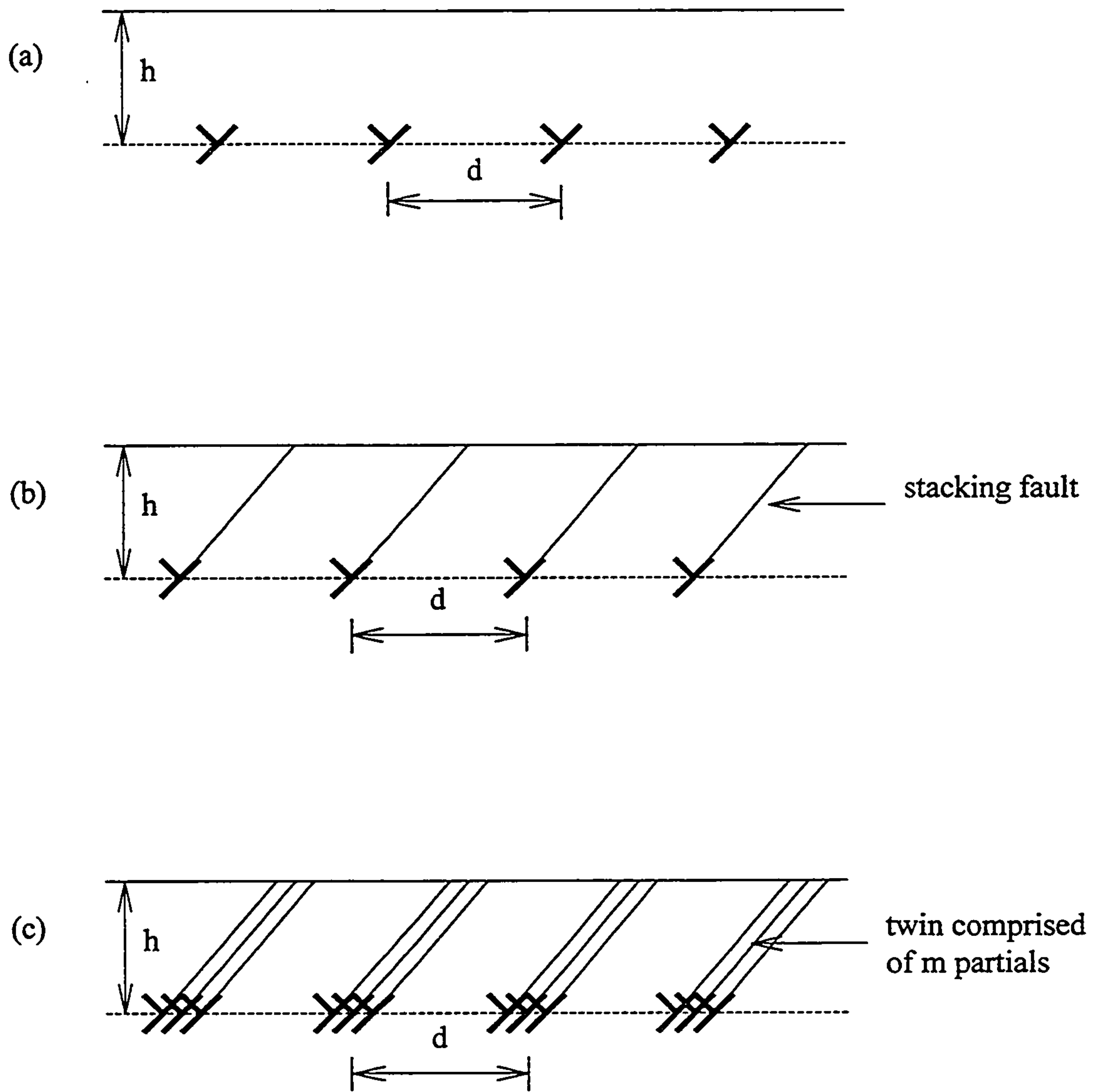

Schematic illustrations of the film with an array of perfect dislocations at the interface (a), an array of partial dislocations at the interface bounding stacking faults (b), and an array of twins comprised of m partials (c).

$E_{int,\ twin/film}$ and $E_{int,twin/twin}$ can be calculated using equations (2.2.15) and (2.2.16) by replacing b with mb, giving

$$E_{int,twin/film} = -\frac{2\mu(1+\nu)|f|hmb\sin\beta\cos\varphi}{(1-\nu)d} \tag{2.2.20}$$

and

$$E_{int,twin/twin} = \frac{\mu(mb)^2(1-\nu\cos^2\beta)}{4\pi(1-\nu)d}\left[\frac{d}{2\pi h}\sinh\left(\frac{2\pi h}{d}\right)\right]$$

$$+\frac{\mu(mb)^2\sin^2\beta\cos^2\varphi}{4\pi(1-\nu)d}\left[\frac{2\pi h}{d}\coth\left(\frac{2\pi h}{d}\right)-\frac{2\pi^2h^2}{d^2}\operatorname{csch}^2\left(\frac{2\pi h}{d}\right)-\frac{1}{2}\right]$$

$$-\frac{\mu(mb)^2\sin^2\beta\sin^2\varphi}{4\pi(1-\nu)d}\left[\frac{2\pi h}{d}\coth\left(\frac{2\pi h}{d}\right)+\frac{2\pi^2h^2}{d^2}\operatorname{csch}^2\left(\frac{2\pi h}{d}\right)-\frac{3}{2}\right]$$

(2.2.21)

By minimizing the total energy of the system with respect to d and m for a given value of h, the equilibrium twin thickness and spacing may be determined as a function of the film thickness. The application of this approach for both 60° perfect and 90° partial dislocations, as well as twins, is discussed in Chapter 6.

2.2.3 Equilibrium position of misfit dislocations

With the advent of high resolution transmission electron microscopy techniques, there have been a number of experimental observations of misfit dislocations that demonstrate that the core of the dislocation is often not precisely located at the interface, but is displaced some distance into the elastically softer phase (Mader 1987; Knauss and Mader 1991). Theoretical predictions of the magnitude of the displacement from the interface location have been given

by Mader and Knauss (1992) using a force balance argument, and by Gutkin *et al.* (1989) using an energy approach. The problem was treated using two elastically isotropic, semi-infinite solids with different elastic constants, having a uniaxial misfit in the interface plane. Both authors adopted the approach of Mura (1968) to solve the elasticity problem, although Mura's solution in turn implicitly used in the earlier work of Head (1953a, 1953b).

Consider a system as shown in Fig. 2.5. Two isotropic semi-infinite media I and II are perfectly bonded at a planar interface. The elastic properties may be described by the shear modulus μ and Poisson's ratio ν, with subscripts 1 and 2 referring to regions I and II respectively. In the analysis that follows it is assumed that $\mu_2 > \mu_1$, and $\nu_1 = \nu_2 = \nu$. For simplicity, the lattice planes have different spacings, a_1 and a_2 respectively, in the two crystalline regions I and II only normal to the x direction, with $a_1 < a_2$. For the plane strain case, the coherency stresses along x the direction in regions I and II are given by (Mader and Knauss 1992):

$$\sigma_{xx}^{I} = \frac{2\mu_1\mu_2 f}{(\mu_1+\mu_2)(1-\nu)}$$

$$\sigma_{xx}^{II} = -\frac{2\mu_1\mu_2 f}{(\mu_1+\mu_2)(1-\nu)} \qquad (2.2.22)$$

where $f = 2(a_2 - a_1)/(a_2 + a_1)$ is the misfit.

A single edge dislocation $\mathbf{b} = (b,0,0)$ is introduced into the softer phase, region I with smaller μ, lying at the point (0,d) from the interface (Fig.2.5). There are two forces acting on the dislocation in Fig.2.5: (a) the coherency force (f_y^c) and (b) the image force due to the interface (f_y^i). The coherency force (Peach-Koehler force) on the dislocation in region I

Figure 2.5

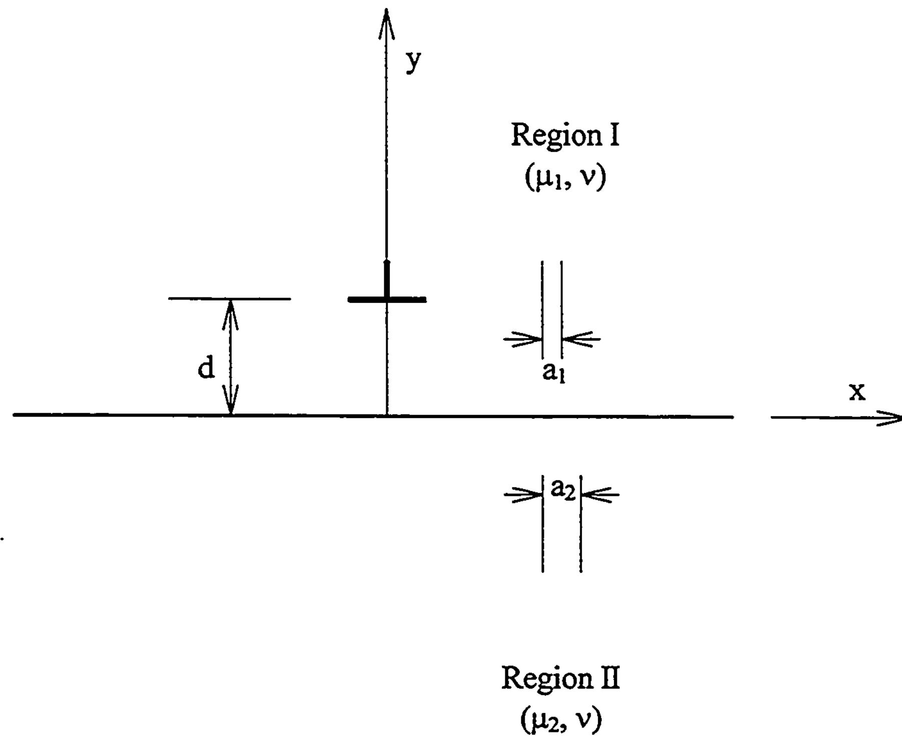

Schematic illustration of two semi-infinite media containing a misfit dislocation.

is given by:

$$F_y^c = -\sigma_{xx}^I b = -\frac{2\mu_1\mu_2 fb}{(\mu_1+\mu_2)(1-\nu)} \qquad (2.2.23)$$

The image force on the dislocation due to the interface can be calculated as (Dundurs and Sendeckyj 1965):

$$F_y^i = -\frac{\mu_1 b^2}{8\pi(1-\nu)d}(A+B) \qquad (2.2.24)$$

where $A = \frac{1-\Gamma}{1+\kappa\Gamma}$, $B = \frac{\kappa(1-\Gamma)}{\kappa+\Gamma}$, $\kappa = 3-4\nu$, and $\Gamma = \frac{\mu_2}{\mu_1}$.

Equation (2.2.24) is identical to equation (3) in the paper of Mader and Knauss (1992). At equilibrium the total force acting on the dislocation $F_y^c + F_y^i$ must vanish, i.e.

$$F_y^c + F_y^i = 0 \qquad (2.2.25)$$

Combining equations (2.2.23), (2.2.24) and (2.2.25), the equilibrium distance of the dislocation from the interface is obtained as

$$d = -\frac{b(\mu_1+\mu_2)(A+B)}{16\pi\mu_2 f} = -\frac{b(1+\Gamma)(A+B)}{16\pi\Gamma f} \qquad (2.2.26)$$

Gutkin *et al.* (1989) made a similar analysis for an edge dislocation based on the minimization of the energy as a function of the dislocation position. Both analyses were performed in a system with the interface separating two semi-infinite media. This approach cannot be applied to the case of epitaxially grown thin films on substrates where the misfit dislocations are near a free surface, and the thickness of the film is orders of magnitude smaller than the thickness of the substrate. Under these conditions, the presence of the free

surface is extremely important. Head (1953a) provided an exact solution for the equilibrium position of a screw dislocation in the thin film. Consider a semi-infinite isotropic elastic medium of shear modulus μ_1 for y>0 and shear modulus μ_2 for $-h<y<0$, with a free surface at $y = -h$. Then a screw dislocation with **b** = [0,0,b] at (0,d) will induce a stress field described by an infinite set of image dislocations at positions $(0,y_i)$ and strength (S_i), as follows (Head 1953a):

Position of image Value of y_i	Strength of image S_i
$-d$	$+p$
$-(d+2h)$	$-(1-p^2)$
$-(d+4h)$	$-(1-p^2)p$
$-(d+6h)$	$-(1-p^2)p^2$
$-(d+8h)$	$-(1-p^2)p^3$
etc	etc

where $p = \frac{\mu_2 - \mu_1}{\mu_2 + \mu_1} = \frac{\Gamma - 1}{\Gamma + 1}$, with $\Gamma = \frac{\mu_2}{\mu_1}$.

The force of each image acting on the screw dislocation at (0,d) is given by (Hirth and Lothe 1982):

$$f_y^i = \frac{\mu_1 b^2}{2\pi(d+|y_i|)} S_i \tag{2.2.27}$$

Thus, the total image force on the dislocation is

$$F_y^i = \Sigma f_y^i = \frac{\mu_1 b^2}{4\pi d}\left[p - (1-p^2)\sum_{i=1}^{\infty}\frac{d}{d+ih}p^{i-1}\right] \tag{2.2.28}$$

The equilibrium position of the dislocation can be determined by $F_y^i = 0$, i. e.

$$\frac{\mu_1 b^2}{4\pi d}\left[p - (1-p^2)\sum_{i=1}^{\infty}\frac{d}{d+ih}p^{i-1}\right] = 0 \tag{2.2.29}$$

In Chapter 7, a complete analysis of stress and equilibrium position of a mixed dislocation in a thin film is presented, following the approach of Head (1953a, 1953b).

2.3 Surface instability and composition modulation

2.3.1 Strain relaxation via surface morphological instability

It has long been known that misfit between the film and substrate can change the growth mode of a thin film from a layer-by-layer mechanism to a three dimensional island mechanism. The traditional explanation for this phenomenon is that misfit dislocations form at the film-substrate interface, which relieve the misfit strain and serve as nucleation sites for islands at the film surface (Matthews and Blakeslee 1975). Recently it has become clear that a planar heteroepitaxial layer can undergo transitions to rougher morphologies without the creation of misfit dislocation (Eaglesham and Cerollu 1990; Guha *et al.* 1990; Synder *et al.* 1991; Cullis *et al.* 1996). Furthermore recent experiments show that the development of surface undulations depends on the sign of the strain. In the Ge/Si system, films under compression roughen easily while those under tension remain relatively smooth (Xie *et al.* 1994). However, the surface roughness of $In_{1-x}Ga_xAs_yP_{1-y}$/InP system exhibits the reverse dependency on the sign of the strain: tensile strained films have a clear tendency to form undulating surfaces while compressive strained films do not (Ponchet *et al.* 1995; Okada *et al.* 1997). An anisotropy in the surface undulation between <011> directions has also been observed by Ponchet *et al.* (1995) and Okada *et al.* (1997). In the $In_{1-x}Ga_xAs_yP_{1-y}$/InP system, surface undulation occurs predominantly along the [011] direction, but not the $[0\bar{1}1]$ direction.

The surface morphological instability is defined by a competition between the elastic and surface free energy of the system. The elastic free energy is reduced for a rough surface because of partial relaxation while the surface free energy is increased because of the larger surface area. The following simple energetic analysis shows the nature of the expected instability in heteroepitaxial strained thin films. Considering an elastic half-plane subjected to stress σ as shown in Fig.2.6. The change in energy per unit length in going from the flat surface (Fig.2.6a) to the simple square wave surface morphology (Fig2.6b) is roughly (Srolovitz, 1989)

$$\Delta E = E_e + E_s = -\frac{\sigma^2}{2E}\lambda e + 2\gamma \cdot 2e \qquad (2.3.1)$$

where γ is the surface energy and E is Young's modulus. It has been crudely assumed in equation (2.3.1) that the stresses in the interior of the square protrusions are zero.

Equation (2.3.1) shows that the formation of this "rough" surface profile lowers the energy of the system provided that the wavelength, $\lambda > 8\gamma E/\sigma^2$. Although the above analysis is crude, it demonstrates why the surfaces of stressed bodies may be unstable.

Srolovitz (1989) also derived the stress field of a semi-infinite body with a sinusoidally undulated surface $y = e \cdot \sin(kx)$ with $k = 2\pi/\lambda$ and $e \ll \lambda$ (Fig.2.6c) using an Airy stress function method. The stresses were found to be:

$$\sigma_{xx} = \sigma\left[1 - ek(ky-2)e^{-ky}\sin(kx)\right]$$

$$\sigma_{yy} = \sigma e k^2 y e^{-ky}\sin(kx)$$

$$\sigma_{xy} = \sigma e k^2 (1-ky)e^{-ky}\cos(kx) \qquad (2.3.2)$$

Equations (2.3.2) are consistent with those derived by Gao (1991) who followed a different approach via a perturbation analysis. Equations (2.3.2) show that the undulated surface can magnify the bulk stress by a factor of 2 to 3. This stress concentration effect is significant, especially for already highly stressed heteroepitaxial semiconductor thin films, suggesting that the surface morphology of the film surfaces can play an important role in nucleating dislocations and cracks. In Chapter 6, equation (2.3.2) is used to calculate the dislocation nucleation at an undulated film surface.

For stability analysis, Srolovitz (1989) used Mullins' equation which describes the change in surface profile h(x,t) with time t. When the surface morphological evolution is controlled by surface diffusion, $\frac{\partial h}{\partial t} = \frac{D_s \Omega \delta}{kT} \frac{\partial^2 \mu}{\partial s^2}$ where D_s is the surface diffusivity, Ω is the atomic volume, δ is the number of atoms per unit area, kT is the thermal energy, s is the distance along the surface and $\mu(x)$ is the chemical potential including a strain energy density variation along the surface. Assuming that the magnitude of the undulation is much smaller than its wavelength, Srolovitz concluded that $\lambda_c = \pi E\gamma/\sigma^2$ is the critical wavelength for morphological instability. If the wavelength of an undulation is larger than λ_c, the undulation has a positive growth rate.

Grilhe (1993) estimated the elastic fields in an undulated body by representing them with the elastic fields of imaginary surface dislocations. He derived an appropriate surface dislocation distribution which satisfies the traction-free condition at the surface and found the critical wavelength $\lambda_c = 2\pi\mu\gamma/(1-\nu)\sigma^2$ where μ is the shear modulus, which is in good agreement with Srolovitz's result. Following Grilhe's approach, Okada *et al.* (1997) obtained

Figure 2.6

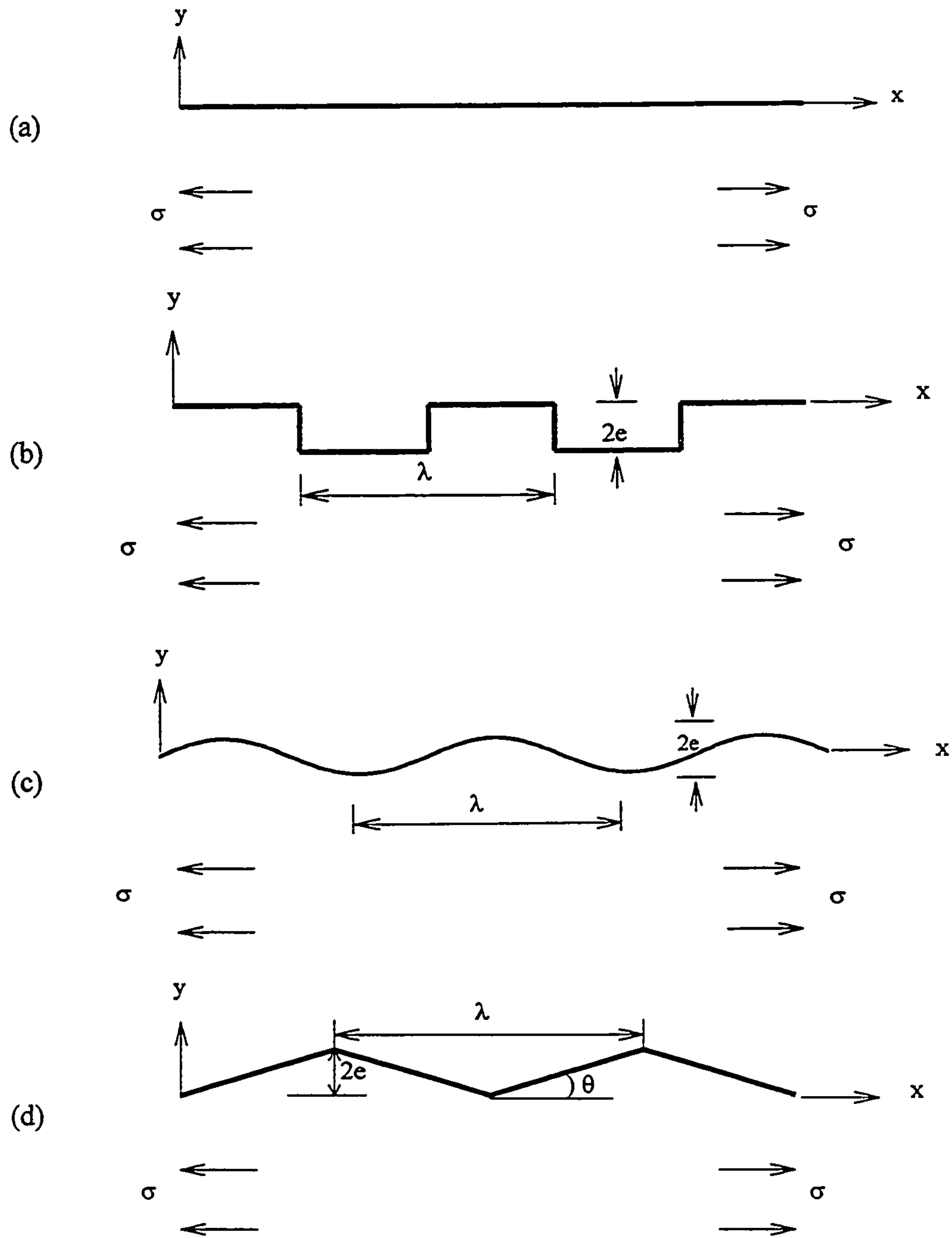

Strain relaxation by surface morphological instability. (a) An elastic half-plane subjected to tensile stress σ, (b) A square wave surface profile. The surface profile has wavelength λ and amplitude e, (c) A sinusoidal surface. $y = e \sin(kx)$ with $k = 2\pi/\lambda$, and (d) A faceted surface.

the critical wavelength for a faceted surface shown in Fig.2.6d. They found that the InGaAs films under tension (+0.5% to +0.6% strain) developed facets on $(113)_A$ or $(114)_A$ planes. The corresponding surfaces can be described as a series of (001) terraces, locally preserving the (2×4) reconstruction at the (001) surface, separated by double steps. To a first approximation the increase in surface energy in going from (001) surface to a (114) surface, for example, can be associated with the steps. If the step energy per unit length is Γ, and the step density measured in a [110] direction is ρ, the critical wavelength is given by (Okada *et al.* 1997)

$\lambda_c = \dfrac{32\mu\Gamma\rho}{\pi(1-\nu)\sigma^2\tan^2\theta}$, where θ is defined in Fig.2.6d.

2.3.2 Composition modulation in $In_{1-x}Ga_xAs_yP_{1-y}$ films

TEM contrast related to composition modulation has been observed by many authors in $In_{1-x}Ga_xAs_yP_{1-y}$ heteroepitaxial strained layers (Henoc *et al.* 1982; Chu *et al.* 1985; McDevitt *et al.* 1992; Ponchet *et al.* 1994; Okada *et al.* 1997). Composition modulation in strained layers has some unique characteristics, which are different from those found in bulk materials. There are many interesting experimental results on composition modulations in $In_{1-x}Ga_xAs_yP_{1-y}$ heteroepitaxial strained layers. Early studies suggested that the composition modulations always occurred in <001> directions (Henoc *et al.* 1982; Chu *et al.* 1985). However, further studies have shown that the composition modulation in thin films occurs along <011> directions not the <001> elastically soft directions, and is anisotropic between [011] and $[0\bar{1}1]$ directions (Ponchet *et al.* 1994; LaPierre *et al.* 1996; Okada *et al.* 1997). The presence of a composition modulation depends on the sign of strain built into the strained layer: the

composition modulation in the film under tension is much stronger than that in the film under same value of compression (Okada *et al.* 1997). The explanation for the origin of the composition modulation in $In_{1-x}Ga_xAs_yP_{1-y}$ alloys is believed to lie in the position of the chemical spinodal relative to the parameters x, y and growth temperature. Onabe (1982) and Stringfellow (1982) calculated the chemical spinodal of $In_{1-x}Ga_xAs_yP_{1-y}$ alloy, based on the regular solution approximation for a solid solution. The free energy G for an $In_{1-x}Ga_xAs_yP_{1-y}$ alloy can be expressed as (Onabe 1982)

$$\begin{aligned} G = &\omega_{InP}(1-x)(1-y) + \omega_{InAs}(1-x)y + \omega_{GaP}x(1-y) + \omega_{GaAs}xy \\ &+ \alpha_{InP-GaP}(1-x)x(1-y) + \alpha_{InAs-GaAs}(1-x)xy \\ &+ \alpha_{InP-InAs}(1-x)(1-y)y + \alpha_{GaP-GaAs}x(1-y)y \\ &+ RT[(1-x)\ln(1-x) + x\ln(x) + (1-y)\ln(1-y) + y\ln(y)] \end{aligned} \qquad (2.3.3)$$

where the ω values are the sum of the first and second nearest-neighbour interaction energies of a binary compound, the α values are the ternary interaction parameters, R is the gas constant and T is the absolute temperature. The spinodal of an alloy with two independent parameters x and y is defined by (Prigogine and Defay, 1954)

$$\frac{\partial^2 G}{\partial x^2}\frac{\partial^2 G}{\partial y^2} - \left(\frac{\partial^2 G}{\partial x \partial y}\right)^2 = 0 \qquad (2.3.4)$$

Substituting equation (2.3.3) into (2.3.4), we have

$$\begin{aligned} &\{RT - 2(1-x)x[(1-y)\alpha_{InP-GaP} + y\alpha_{InAs-GaAs}]\} \\ &\times \{RT - 2(1-y)y[(1-x)\alpha_{InP-InAs} + x\alpha_{GaP-GaAs}]\} \\ &-(1-x)x(1-y)y(\omega_Q + \alpha_Q)^2 = 0 \end{aligned} \qquad (2.3.5)$$

where $\omega_Q = \omega_{InP} - \omega_{InAs} - \omega_{GaP} + \omega_{GaAs}$ and

$\alpha_Q = (1-2x)(\alpha_{InAs-GaAs} - \alpha_{InP-GaP}) + (1-2y)(\alpha_{GaP-GaAs} - \alpha_{InP-InAs})$. The value of ω_Q is 3688 + 0.92T (cal/mol) and values of $\alpha_{InP-GaP}$, $\alpha_{InAs-GaAs}$, $\alpha_{InP-InAs}$, and $\alpha_{GaP-GaAs}$ are 3500 (cal/mol), 3000 (cal/mol), 400 (cal/mol) and 400 (cal/mol) respectively (Onabe 1982). The chemical spinodal for the $In_{1-x}Ga_xAs_yP_{1-y}$ alloy at 480°C calculated using equation (2.3.5) is shown in Fig.1.1. In Chapter 8, this chemical spinodal is used to discuss the composition modulations observed in a series of $In_{1-x}Ga_xAs_yP_{1-y}$ alloy films with different compositions.

Chapter 3

Experimental techniques

3.1 Molecular beam epitaxy

All lattice-mismatched epitaxial $In_{1-x}Ga_xAs_yP_{1-y}$ films used in this study were grown on (100) InP substrates using gas source molecular beam epitaxy (GS-MBE) in which the evaporation sources are used for the group III elements (In and Ga), while the group V constituents are supplied primarily in the form of AsH_3 and PH_3. The hydrides are decomposed in a single, low pressure cell heated to 1000°C following $2MH_3 \rightarrow M_2 + 3H_2$ where M represents P or As. All films were grown at a rate of 1μm/h and 480°C. Fig.3.1 is a schematic diagram of the McMaster MBE system used for $In_{1-x}Ga_xAs_yP_{1-y}$ film growth in this study. An InP wafer mounted on a sample holder is first evacuated in the load-lock then transferred to the Auger electron spectroscopy (AES) chamber where the wafer is degassed at 350-400°C. After the degassing step, the sample is transferred to the main growth chamber where the temperature is raised to the growth temperature, under a P_2 overpressure which prevents the preferential evaporation of P from InP wafer. The oxide layer formed on the InP wafer is removed with the help of an electron cyclotron resonance plasma of hydrogen for about 2 minutes. Usually an InP buffer layer about 1000Å thick is deposited first on a substrate to ensure a clean and flat surface for subsequent heteroepitaxial growth. All epitaxial growth is commenced after achieving a clean group V stabilized surface showing a (2×4) streaky reflection high energy electron diffraction (RHEED) pattern.

3.2 Transmission electron microscopy

3.2.1 Sample preparation

Figure 3.1

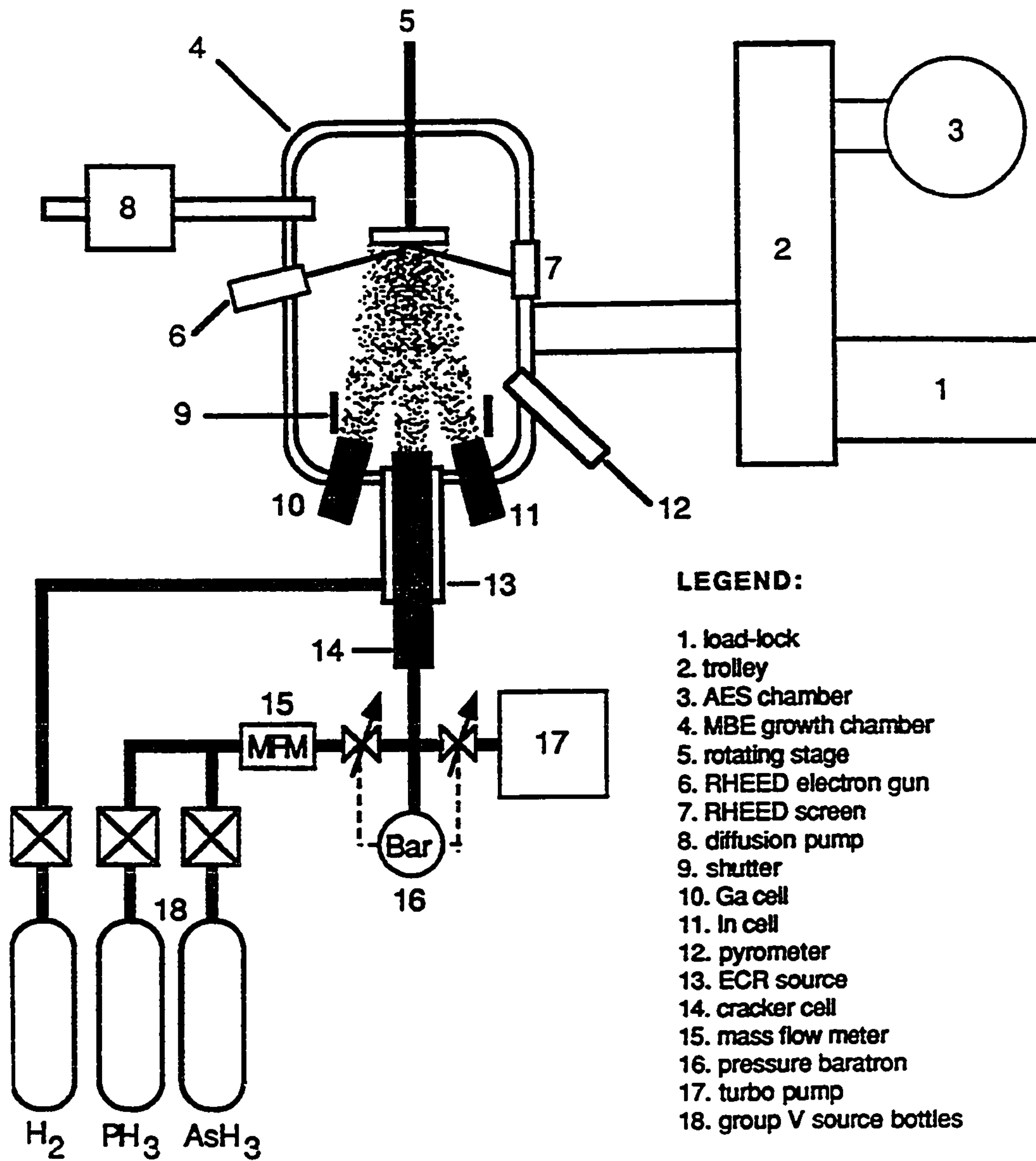

Schematic diagram of McMaster GS-MBE system. (after Lapierre, 1994)

High quality TEM samples with a wide observable area are needed for successful TEM observations. $[0\bar{1}1]$ cross-section, [011] cross-section and (100) plan-view TEM samples were prepared in this study.

(A) <011> cross-section TEM sample

After the MBE growth of $In_{1-x}Ga_xAs_yP_{1-y}$ epitaxial films on a (100) InP substrate, two bars of about 7×1×0.4 mm^3 are cut out of a wafer by cleaving along {011} planes (Fig.3.2a). These two bars are glued together with the epitaxial sides face-to-face to make the central part of the cross-section sample. Then 8 supporting Si bars of about 7×1×0.4 mm^3 are glued to both sides (4 for each side) of the central part to make a sample sandwich" of about 7×3.6×1 mm^3 (Fig.3.2b). After mechanical thinning of the sample sandwich to ~ 300 μm thick, two 3 mm diameter discs are cut from the sandwich using an ultrasonic disc cutter (Fig.3.3c). To prevent it from being broken, the disc is then glued onto a molybdenum ring, 3 mm in outside diameter, 2mm in inside diameter and 30μm in thickness. Then the disc is mechanically thinned from the no-ring side to ~ 100 μm thickness (Fig.3.2d). The thinned disc is dimpled from the no-ring side with 3 μm diamond paste until the center of the disc is ~ 20 μm thick (Fig.3.2e), and then polished from both sides with 1 μm diamond paste to get a very smooth surface. The final thinning until perforation is conducted using Ar ion-milling with a liquid N_2 cold stage from both sides using an ion beam angle of 10°, a gun voltage of 4 kV and a gun current of 0.5 mA (Fig.3.2f).

(B) (100) plan-view TEM sample

A 3 mm diameter disc about 0.4 mm thick is first cut from the wafer using an ultrasonic disc cutter. The disc is then glued onto the molybdenum ring with the epitaxial side

Figure 3.2

(a)

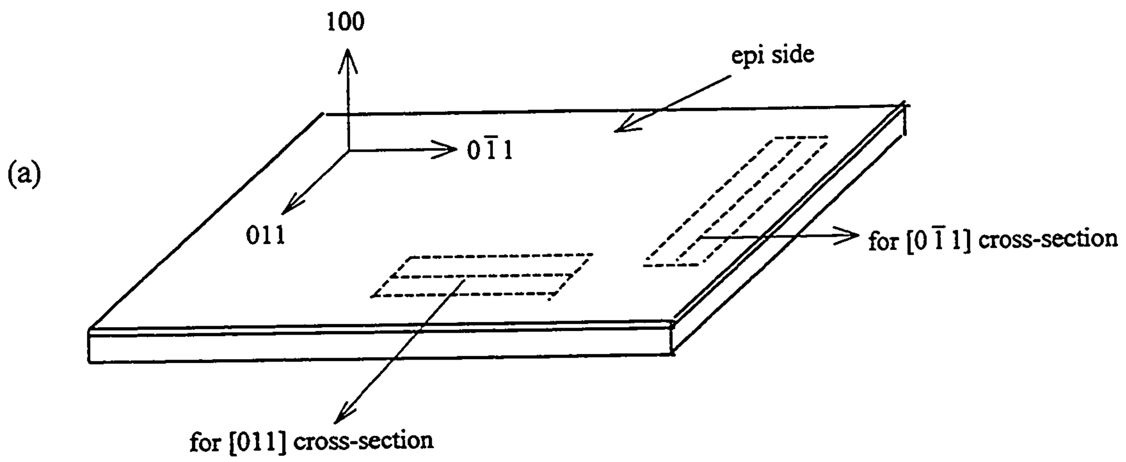

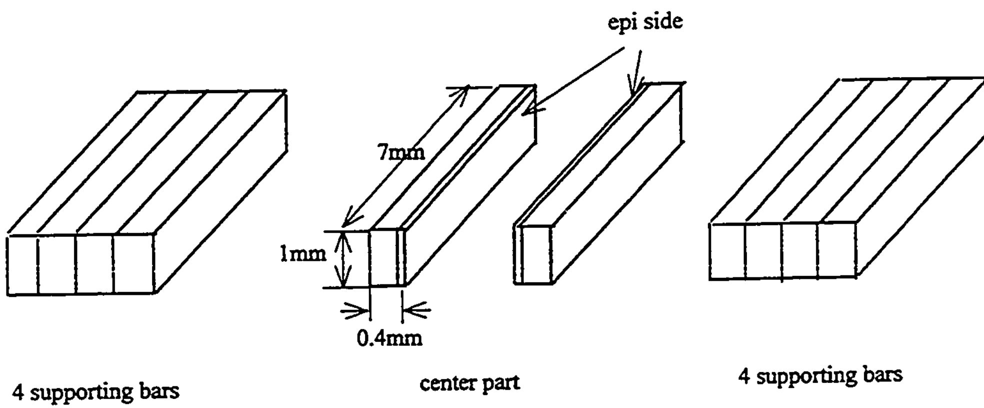

(b)

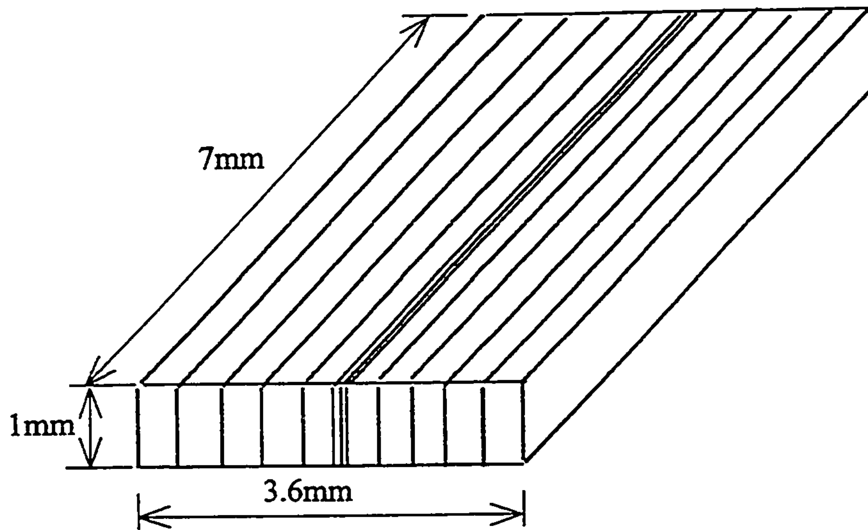

Figure 3.2 (continued)

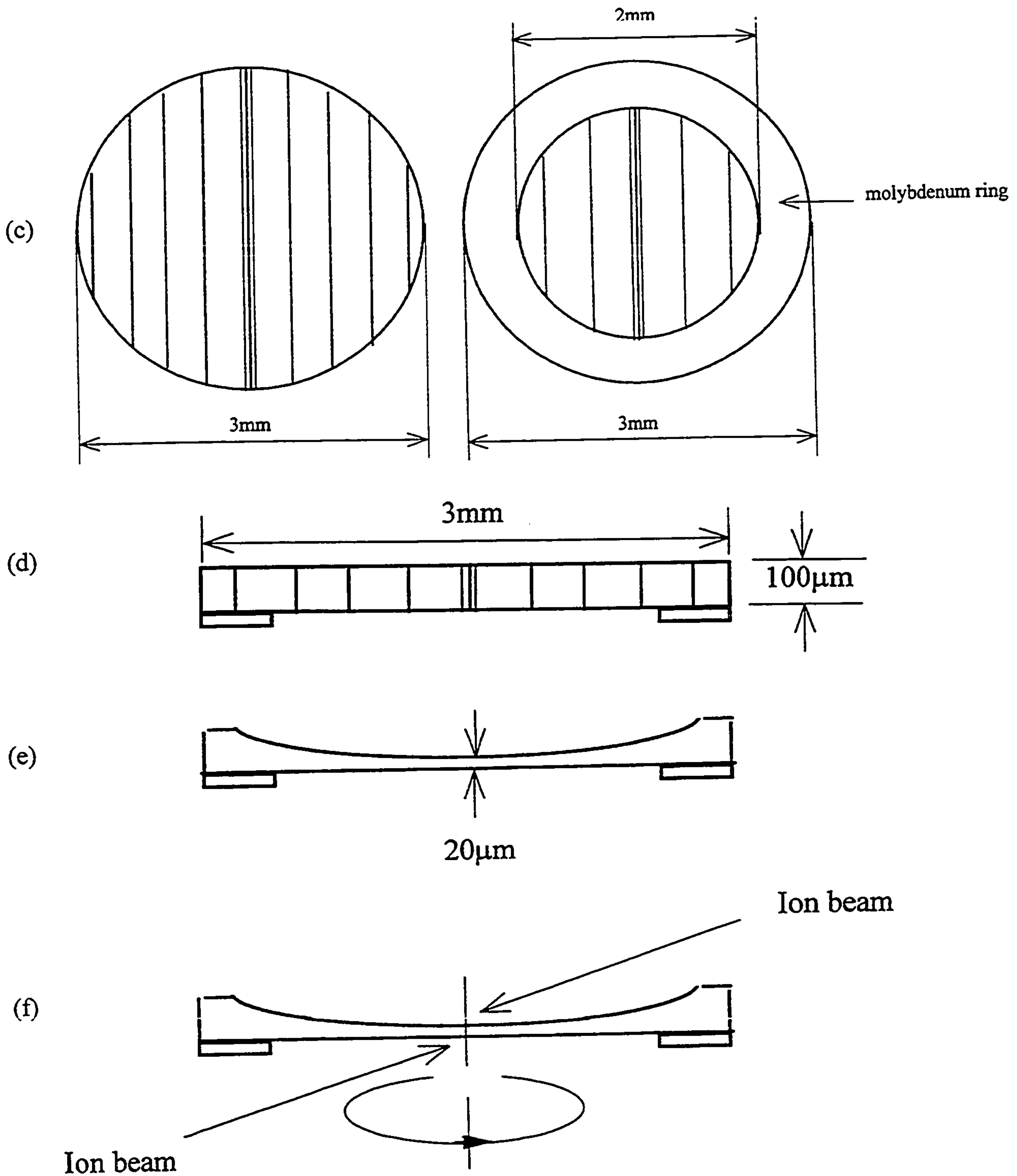

<011> cross-section TEM sample preparation.

contacting the ring. The disc is then mechanically thinned from the substrate side to ~ 100 μm thickness, followed by dimpling and polishing the disc until the centre of disc is ~ 20 μm thick. The final thinning until perforation is again conducted using Ar ion-milling with liquid N_2 cold stage but from one side – the substrate side at ion beam angle of 10°, a gun voltage of 4 kV and a gun current of 0.5 mA.

The TEM samples were examined in a Philips CM12 operating at 120 kV and a JEOL 2010F field emission source TEM operating at 200kV.

3.2.2 TEM diffraction contrast

To get good strong diffraction contrast in both bright field (BF) and dark field (DF) images, the specimen is tilted to two-beam conditions, in which only one diffracted beam is strongly excited. In practice, we always use this two-beam condition to form a conventional TEM image. From the two-beam theory with the column approximation, the amplitudes of the diffracted beam ϕ_g and the transmitted beam ϕ_0 for a perfect crystal are given by the Howie-Whelan equations as follows (Hirsch *et al.* 1977)

$$\frac{d\phi_g}{dz} = \frac{\pi i}{\xi_g}\phi_0 \exp(-2\pi isz) + \frac{\pi i}{\xi_0}\phi_g$$

$$\frac{d\phi_0}{dz} = \frac{\pi i}{\xi_0}\phi_0 + \frac{\pi i}{\xi_g}\phi_g \exp(2\pi isz) \qquad (3.2.1)$$

where z is the coordinate taken down into the column, s is the deviation parameter, ξ_g is the extinction distance for the diffracted beam, and ξ_0 is the extinction distance for the transmitted beam.

Solving equation (3.2.1), the intensities in the Bragg-diffracted beam and transmitted beam

are given by (Hirsch *et al.* 1977)

$$I_g = |\phi_g|^2 = \left(\frac{\pi t}{\xi_g}\right)^2 \left[\frac{\sin^2(\pi t s_{eff})}{(\pi t s_{eff})^2}\right]$$

$$I_0 = 1 - I_g \qquad (3.2.2)$$

The extinction distance is

$$\xi_g = \frac{\pi V_c \cos\theta_B}{\lambda F_g} \qquad (3.2.3)$$

and the effective deviation parameter

$$s_{eff} = \sqrt{s^2 + \frac{1}{\xi_g{}^2}} \qquad (3.2.4)$$

where t is the specimen thickness, V_c is the volume of the unit cell, θ_B is the Bragg angle, λ is the wavelength, and F_g is the structure factor.

Combining equations (3.2.2) and (3.2.3) leads to the diffracted intensity

$$I_g \propto F_g{}^2 \qquad (3.2.5)$$

Thus, a difference in the structure factors of two regions can be used to form a dark-field image with different contrast between the two regions. The application of this approach for imaging composition modulation contrast is discussed in Chapter 8.

Additional diffraction contrast arises from the strain field of crystal defects such as dislocations, stacking faults and so on. For the imperfect crystal, the Howie-Whelan equations become:

$$\frac{d\phi_g}{dz} = \frac{\pi i}{\xi_g}\phi_0 \exp[-2\pi i(sz + \mathbf{g}\cdot\mathbf{R})] + \frac{\pi i}{\xi_0}\phi_g$$

$$\frac{d\phi_0}{dz} = \frac{\pi i}{\xi_0}\phi_0 + \frac{\pi i}{\xi_g}\phi_g \exp[2\pi i(sz + \mathbf{g}\cdot\mathbf{R})] \tag{3.2.6}$$

where **g** is the diffraction vector and **R** is the displacement field associated with the defects at depth z.

Thus, strain contrast associated with the defects will appear if $2\pi \mathbf{g}\cdot\mathbf{R}\neq 0$. This allows one to image crystal defects such as dislocations and stacking faults under TEM.

Perovic *et al.* (1991) studied the electron diffraction contrast of coherently strained films viewed in cross-section. The relaxation of built-in elastic strains near thin foil free surfaces was treated using a line-force model and a Fourier series model. The displacements as a function of foil depth is calculated and used in equation (3.2.6). The two-beam dynamic simulations are shown to accurately predict the observed diffraction contrast features in both single and multilayer structures (Perovic *et al.* 1991).

3.2.3 Setting up a two-beam image

Two-beam diffraction conditions are established by tilting the sample on the double tilt stage until one desired diffracted beam (hkl) is strong (Fig.3.3a). Three types of TEM imaging techniques, namely bright field (BF), centred dark field (CDF) and weak beam dark field (WBDF) are used in this study. To form a two-beam bright field image, the objective aperture is centred on the optic axis (Fig.3.3a). To set up a strong two-beam CDF image, the incident beam is tilted so that the weak $\overline{hkl}$ refection becomes strong as it moves onto the optic axis, then the objective aperture is centred on the axis (Fig.3.3b). To obtain WBDF image, the incident beam is tilted so that the strong hkl reflection moves onto the optic axis. The hkl reflection becomes weak as it moves onto the axis and the 3h3k3l reflection becomes

strong. The objective aperture is then inserted on the axis to form WBDF image (Fig.3.3c).

3.2.4 High-resolution TEM

(A) Phase contrast

Contrast in TEM images can arise due to the differences in the phase of the electron waves scattered through a thin specimen. This contrast can be exploited to form lattice images of a thin specimen – high-resolution TEM images. The high-resolution TEM image is formed in two stages: first, the specimen scatters the incident-electron beam into the scattered beams, which become completely separated at the back focal plane of the objective lens, and then the lenses of the microscope bring the beams back into coincidence at the level of the image. The high-resolution image is therefore always simply an interference pattern. This image contrast is very sensitive to many factors: the appearance of the image varies with small changes in the thickness, orientation, or scattering factor of specimen, and variations in the focus or astigmatism of the objective lens.

Consider first two beam lattice images. The total wave function can be written as

$$\psi = \phi_0 \exp\left[2\pi i\left(\mathbf{k}_I \cdot \mathbf{r}\right)\right] + \phi_g \exp\left[2\pi i\left(\mathbf{k}_D \cdot \mathbf{r}\right)\right] \qquad (3.2.7)$$

where $\mathbf{k}_I$ is the **k**-vector of the incident wave, $\mathbf{k}_D$ is the **k**-vector of the diffracted wave, and $\mathbf{k}_D = \mathbf{k}_I + \mathbf{g} + \mathbf{s}$.

Setting $\phi_0 = 1$ and $\phi_g = R\exp(i\delta)$ with $R = \frac{\pi}{\xi_g}\frac{\sin(\pi ts)}{\pi s}$ and $\delta = \frac{\pi}{2} - \pi ts$, then the intensity is given by

$$I = \psi\psi^* = 1 + R^2 + 2R\cos[2\pi(\mathbf{g}+\mathbf{s})\cdot\mathbf{r}]$$

$$= 1 + R^2 - 2R\sin(2\pi x/d_{hkl} - \pi st) \qquad (3.2.8)$$

Figure 3.3

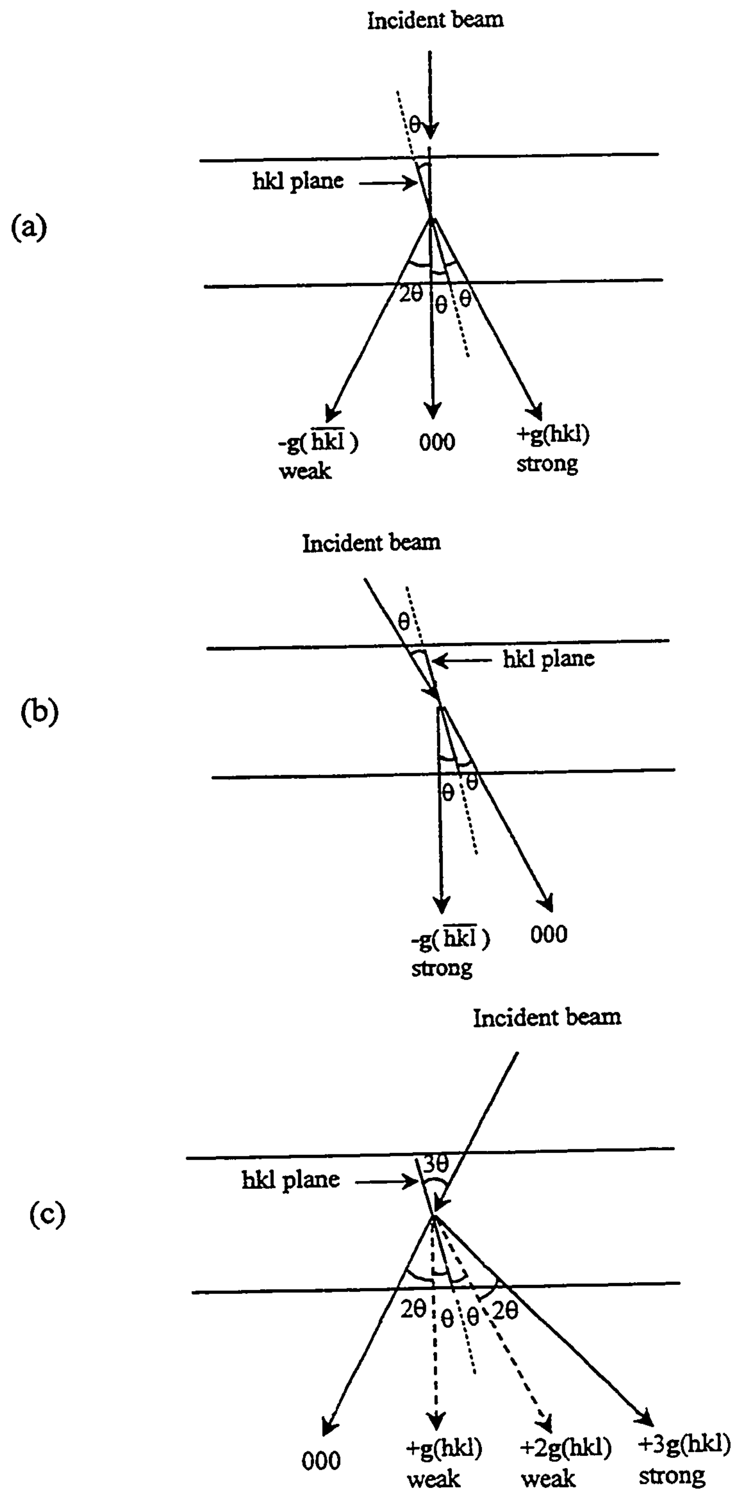

Two-beam conditions of (a) bright field, (b) centered dark field and (c) weak beam dark field images when the objective aperture is on axis.

where x is parallel to the diffracting vector g, and $d_{hkl} = 1/|g|$ is the spacing of the lattice planes.

Therefore, the image appears as a series of sine fringes normal to g (Fig.3.4a), with a periodicity that depends on s and t. Extending this approach to the many-beam case, a lattice image appears (Fig.3.4b).

(B) The fast Fourier transform (FFT)

The Fourier transform method lies at the heart of most calculations for electron diffraction and HRTEM imaging. The fast Fourier transform (FFT) is the method used to reduce the number of operations in the calculation of the Fourier transform, i.e. to reduce the computation time required to interchange electron diffraction patterns and HRTEM images. The mathematical form of the forward Fourier transform is

$$F(j) = \sum_{k=0}^{N-1} f(k) \exp\left(2\pi i \frac{jk}{N}\right) \text{ for } j = 0, 1, \ldots, N-1 \qquad (3.2.9)$$

while the corresponding reverse Fourier transform is

$$f(k) = \frac{1}{N} \sum_{j=0}^{N-1} F(j) \exp\left(-2\pi i \frac{jk}{N}\right) \text{ for } k = 0, 1, 2, \ldots, N-1 \qquad (3.2.10)$$

In Chapter 6, fast Fourier transform (FFT) and inverse fast Fourier transform (IFFT) methods were used to generate HRTEM diffraction patterns and filtered images.

3.3 Other characterization techniques

TEM sample preparation is a destructive technique. Sometimes, it can introduce artefacts during sample preparation. Two other non-destructive techniques, scanning electron microscopy (SEM) and atomic force microscopy (AFM) were also used in this study. SEM

Figure 3.4

(a)

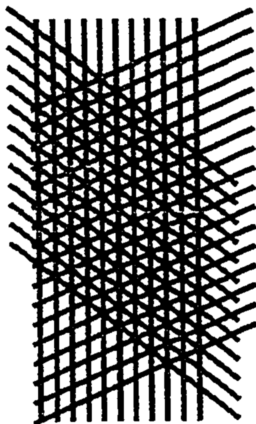

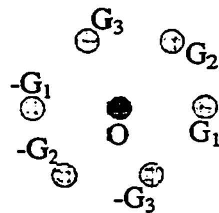

(b)

Lattice images of two-beam (a), and many-beam (b).

was used to study the crack spacing at the surface of cracked films in Chapter 4. SEM observations were conducted with a Philips 515 operating at 20 kV. Secondary electrons were used to form SEM images because this signal is sensitive to the surface topography. High-resolution (1 nm to 5 nm) AFM was used to study the crack opening displacement, the normal surface displacement associated with cracks, and the surface morphology of the films. AFM studies were performed in air using Digital Instruments Nanoscope II and IIIa systems.

Chapter 4

Cracking phenomena in $In_{0.25}Ga_{0.75}As$ films on InP substrates

4.1 Observations

In this chapter, a study of the cracking mechanisms in III-V heteroepitaxial strained layers is presented. Two percent tensile strained $In_{0.25}Ga_{0.75}As$ films with thicknesses of 10 nm, 20 nm, 100 nm, 200 nm and 500 nm grown on (100) InP substrates were chosen for this study. Figure 4.1(a) is a [011] cross-section TEM image of a 20 nm thick sample taken with g = $0\bar{2}2$. V-shaped cracks are visible. These cracks apparently nucleated at the surface of the strained layer and penetrated into the substrate along the [100] growth direction. A TEM image of the same area taken with g = 200 clearly shows that the strain relaxation by cracking is not homogeneous (Fig.4.1(b)). In this image the band of dark contrast in the substrate is a measure of the residual strains in the epilayer. The origin of this contrast, which arises because of surface relaxation of the stresses in the epilayer during TEM sample preparation, is discussed by Perovic *et al.* (1991) (see section 3.2.2). Only the strain at the crack tips has been relaxed while the areas between the crack tips are still strained. Fig.4.1(c) is a HRTEM image of a V- shaped crack, lying on the vertical $(0\bar{1}1)$ plane in the strained layer. This crack has propagated about 10 nm into the substrate, before deviating onto an inclined $\{111\}$ plane and finally terminating at a sharp tip. A close inspection of the lattice image of Fig.4.1(c) shows terminating lattice-fringes near the crack tip, suggesting that there has been dislocation activity accompanying the final stage of crack propagation. This was confirmed by plan-view images. A (100) plan-view TEM image of the 20 nm thick layer sample (Fig.4.2) revealed dislocations emanating from the crack tips.

Figure 4.1

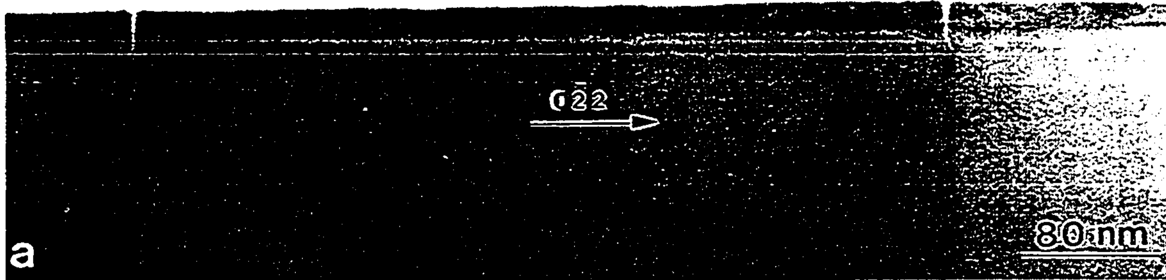

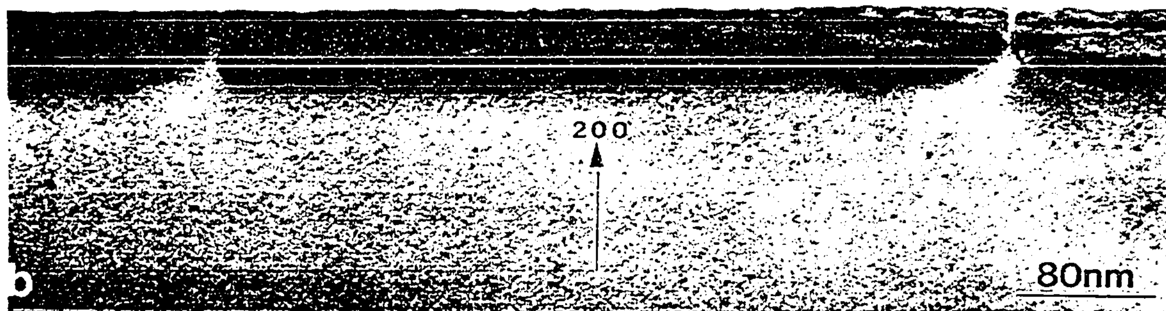

Figure 4.1 (continued)

Cracks in [011] cross-section of 20 nm layer sample. (a) **g** = $0\bar{2}2$ image showing V-shaped cracks. (b) **g** = 200 image showing that the strain was relaxed at the tips of cracks but the areas between the crack tips are still strained. (c) HRTEM image of a crack showing that the crack deviates from the {011} plane onto the {111} plane after penetrating a distance of 10 – 15 nm into the substrate.

The TEM image of the $[0\bar{1}1]$ cross-section for the same layer (Fig.4.3) shows a totally different structure from that observed in the [011] cross-section. Instead of cracks, an array of planar defects (microtwins or stacking faults) was observed in this cross-section.

The density of cracking as growth proceeded was followed by both SEM and XTEM. In the SEM images (Fig.4.4), the lines running along the [011] direction are the contrast from cracks, while the contrast along the $[0\bar{1}1]$ direction comes from surface roughness. (The crack opening displacement of the cracks (in the 20nm thick film) lies below the resolution of the SEM (~5 nm). The cracks must be seen by topographic contrast, as the surface is slightly relaxed next to the cracks. This is discussed in Chapter 5). The SEM observations revealed that the crack spacing increases with an increase in layer thickness. No cracks were observed in the 10nm and 500nm thick samples (Note that the 10nm thick sample is not shown in Fig.4.4). The TEM observations (Fig.4.5) confirmed the SEM results: the crack spacing increases with an increase in layer thickness and no cracks were observed in either 10 nm or 500 nm thick layer samples. Table 4.1 summarizes the SEM and TEM observations of the crack dimensions with film thickness.

Table 4.1 Summary of measurement of crack spacing with different layer thickness

Layer thickness h (nm)	20	100	200
Crack spacing d (nm) (SEM)	600±190	2040±580	4980±1320
Crack spacing d (nm) (TEM)	630±230	2190±470	4900±1660
Crack length c (nm) (TEM)	44±1.2	300±60	560±80
Crack opening displacement δ_0 (nm) (TEM)	5.8±0.4	10±0.7	15±2.3

The total crack length (c) and crack opening displacement (δ_0) are defined in Fig.4.6, a

Figure 4.2

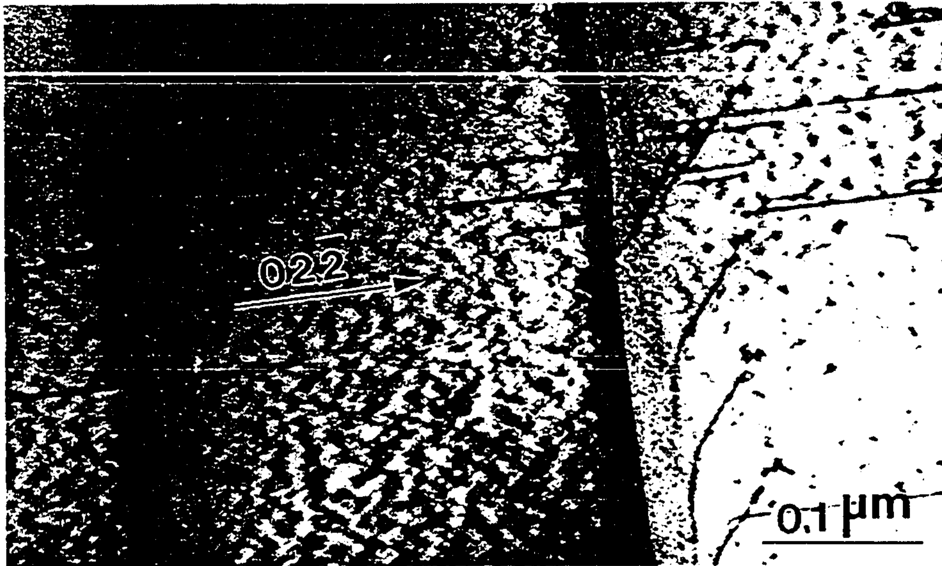

(100) plan-view image with $\mathbf{g} = 0\bar{2}2$ of 20 nm layer sample showing dislocations emanating from the crack tips. The dark-light contrast associated with the cracks is caused by surface strain relaxation effects.

Figure 4.3

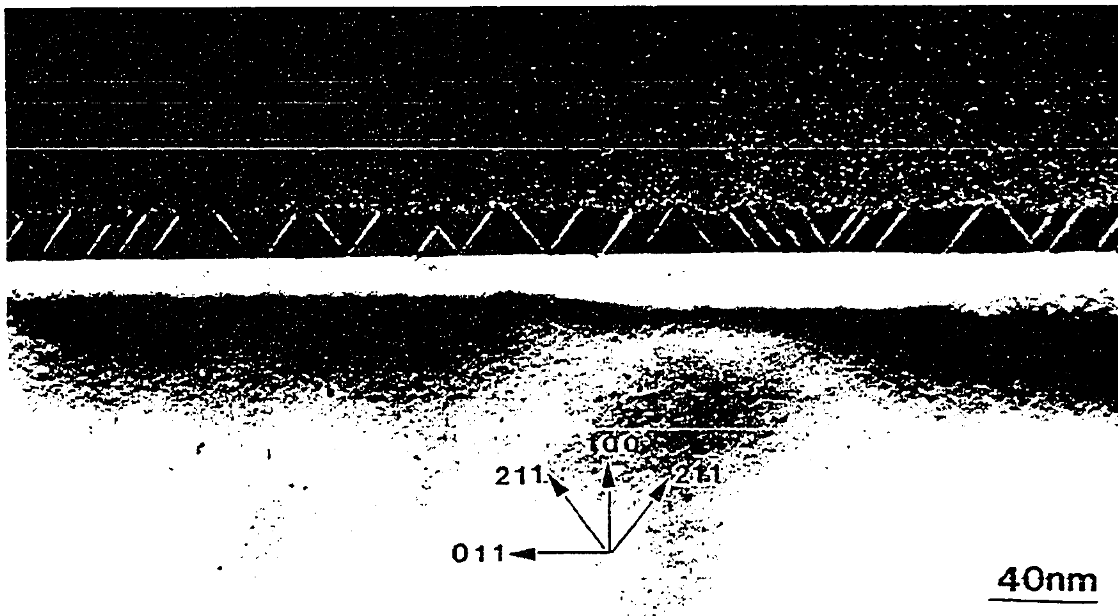

$\mathbf{g} = 200$ dark field image showing planar defects (twins and stacking faults) in $[0\bar{1}1]$ cross-section of 20 nm layer sample.

Figure 4.4

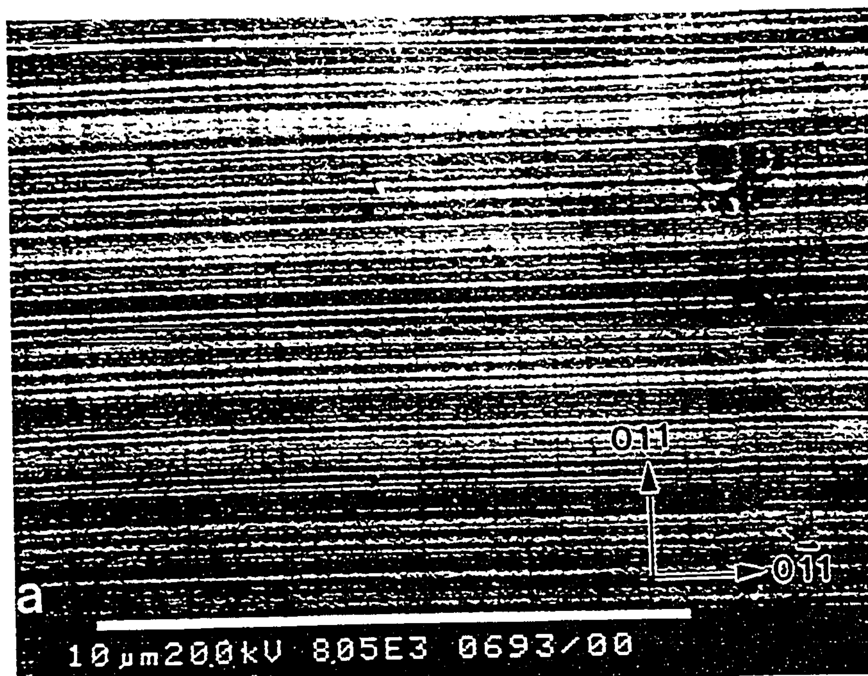

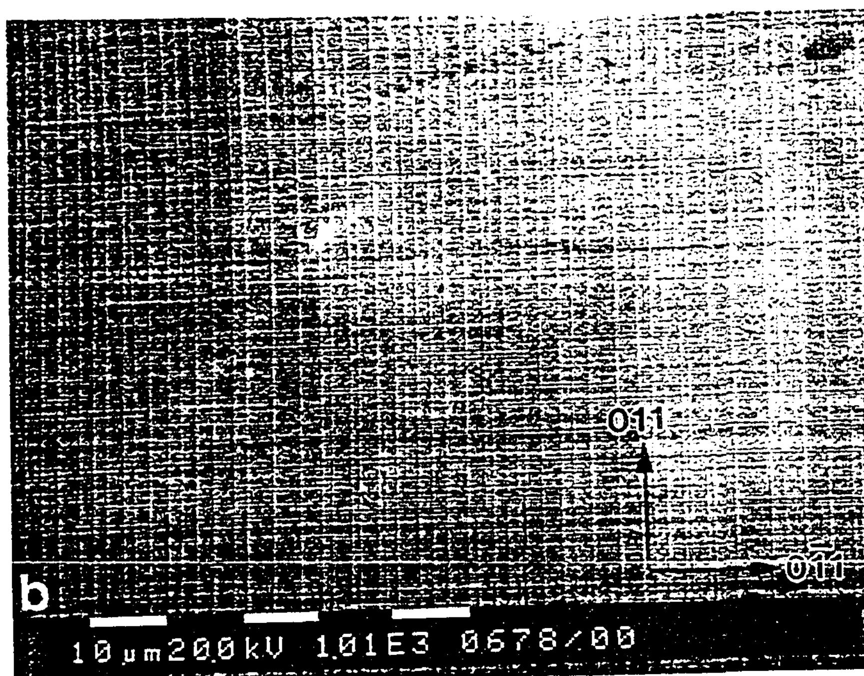

Figure 4.4 (continued)

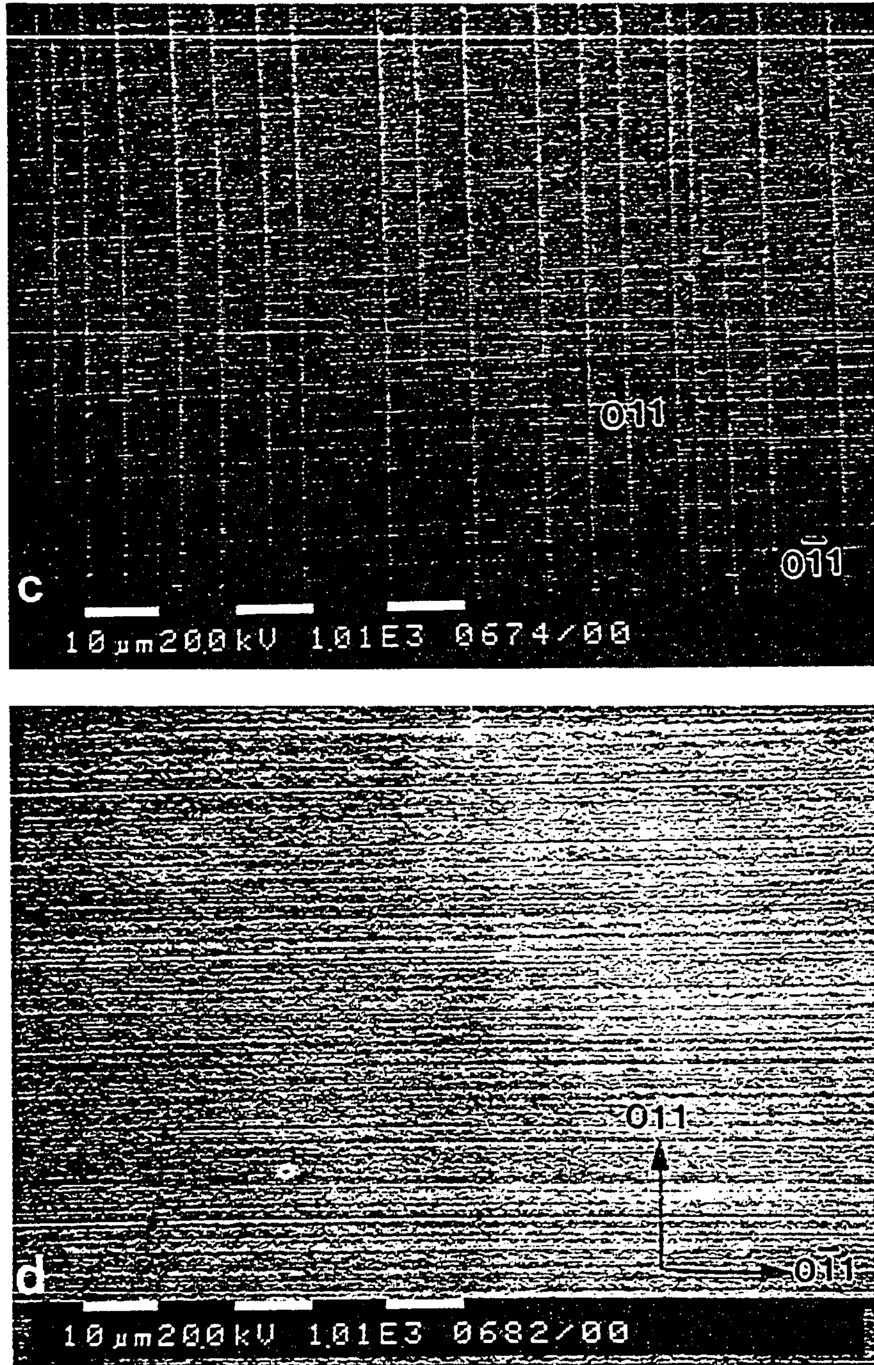

SEM images of epilayer surface showing cracks and roughness contrast. The density of cracks decreases with an increase in layer thickness. No cracks were observed in the 500 nm thick layer: (a) h = 20 nm; (b) h = 100 nm; (c) h = 200 nm; and (d) h=500 nm.

Figure 4.5

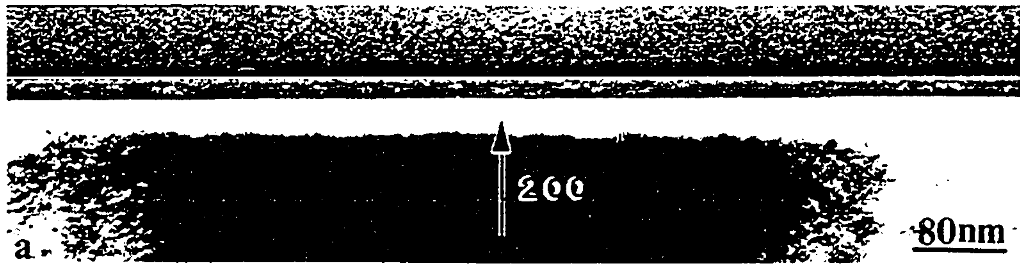

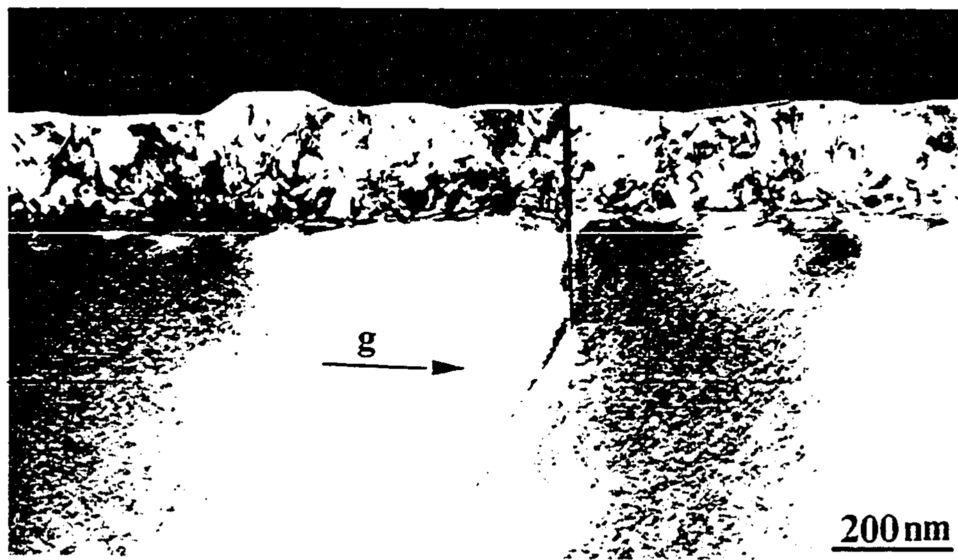

Figure 4.5 (continued)

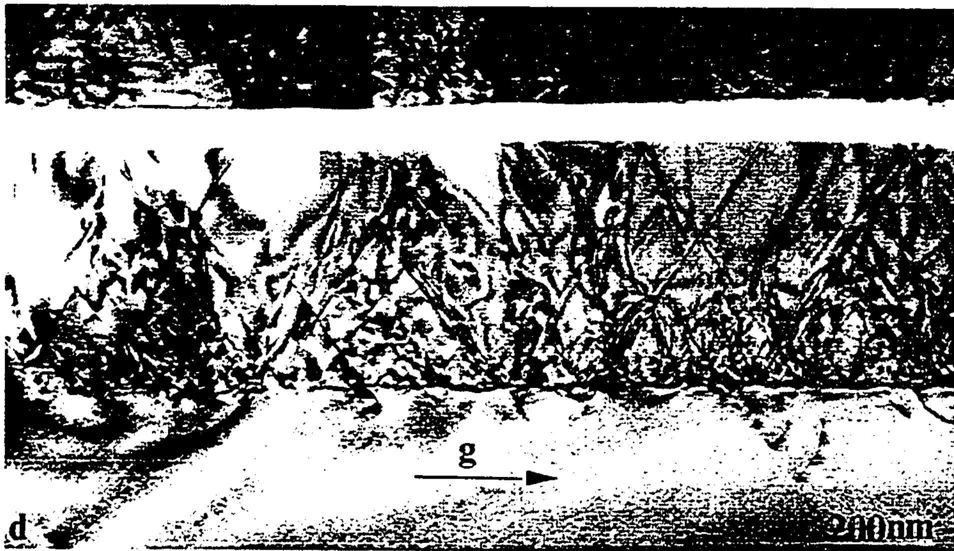

The change of the structure with the change in layer thickness: (a) h = 20 nm, g = 200; (b) h = 100 nm, g = $0\bar{2}2$; (c) h = 200 nm, g = $0\bar{2}2$; (d) h = 500 nm, g = $0\bar{2}2$. Note the increased dislocation activity seen in [011] cross-sections as the film thickness increases.

STEM image from the 100nm thick sample. This figure also displays a part of an energy dispersive x-ray (EDX) analysis of the crack region (marked by an arrow in the figure). This is discussed in Section 4.4.

4.2 Discussion

There are several interesting experimental observations which warrant further scrutiny: the critical thickness at which cracks nucleate (~20 nm in this study); a crack density that decreases as films growth proceeds beyond the critical thickness; the disappearance of cracks in the thickest film (500 nm); the anisotropy of cracking, and the penetration of cracks into the substrate, accompanied by the deviation of the crack plane from $\{011\}$ to $\{111\}$.

Table 4.2 summarizes some of the relevant properties of the III-V compounds, which are used in the Discussion that follows. The properties of $In_{0.25}Ga_{0.75}As$ have been estimated from data for InAs and GaAs, assuming Vegard's Law behaviour as noted in Chapter 1. The elastic properties of the film and substrate are similar. The elastic mismatch is characterized by two Dundurs parameters (Dundurs 1969; Ye *et al*, 1992), α and β, which are given as

$$\alpha = \frac{(1-\nu_s)/\mu_s - (1-\nu_f)/\mu_f}{(1-\nu_s)/\mu_s + (1-\nu_f)/\mu_f}$$

$$\beta = \frac{1}{2}\frac{(1-2\nu_s)/\mu_s - (1-2\nu_f)/\mu_f}{(1-\nu_s)/\mu_s + (1-\nu_f)/\mu_f} \qquad (4.2.1)$$

where μ is the shear modulus and ν the Poisson's ratio; the subscripts f and s indicate film and substrate.

Substituting the values of μ_f, ν_f, μ_s and ν_s from Table 4.2 into equation (4.2.1), we have α =

Figure 4.6

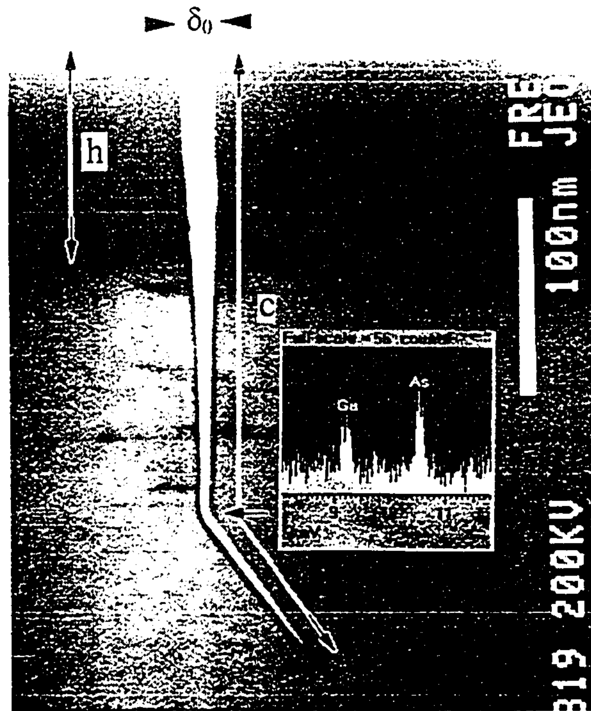

STEM image of crack in 100 nm thick sample, showing the total crack length (c) and crack opening displacement (δ_0). The EDX spectrum from the crack region in the substrate of 100 nm thick sample, showing Ga and As signals.

0.103 and β = 0.003 respectively. Since both α and $\beta \approx 0$, the effect of elastic mismatch can be ignored. The thermal mismatch strain (ε_t) on cooling from the growth temperature (T_g= 480°C) to room temperature (T_r= 25°C) is given by

$$\varepsilon_t = (b_f - b_s)\Delta T = (b_f - b_s)(T_g - T_r) \qquad (4.2.2)$$

where b is the thermal expansion coefficient.

Substituting values of b_f and b_s from Table 4.2 into equation (4.2.2), we have $\varepsilon_t = 6\times10^{-4}$, which is very much smaller than the growth strains, $f = 2\times10^{-2}$, so this effect too can be safely ignored. Finally the estimated room temperature values of the surface energy of InP and $In_{0.25}Ga_{0.75}As$ are very similar (Table 4.2), so the fracture resistance of the film and substrate are probably of the same order of magnitude. (Note that the value of γ has only been measured for GaAs and the values for the other compounds were estimated from the trends calculated by Cahn and Hanneman for all the group III-V compounds.)

Table 4.2 Properties of III-V compounds

	InP	GaAs	InAs	$In_{0.25}Ga_{0.75}As$
Shear modulus μ (GPa)	22.3(a)	32.5(a)	19.0(a)	29.1
Poisson's ratio ν	0.360(a)	0.312(a)	0.352(a)	0.322
Thermal expansion Coefficient b (10^{-6}/K)	4.5(b)	6.0(b)	5.2(b)	5.8
Surface Energy γ (J/m^2)				
{011}	0.75(c)	0.86(d)	0.57(c)	0.77
{111}	0.65(c)	0.75(c)	0.48(c)	0.68

(a) S. Adachi, *J. Appl. Phy.* **53** (1982) 8775
(b) M. Neuberger, *Handbook of electronic materials*, Vol.2 (1972) IFI/Plenum, New York
(c) Estimated values from J.W.Cahn and Hanneman, *Surface Science*, **1**, (1964) 387 (see text)
(d) C. Messmer and J.C.Bilello, *J. Appl. Phy.* **52**, (1982) 4623

4.2.1 Single crack behaviour

Prior to the introduction of any dislocations (twins), cracks or surface roughening, the epitaxial film is in a state of balanced biaxial tension, while the substrate is under compression. The stresses in the film and substrate are given by

$$\sigma^f_{yy} = \sigma^f_{zz} = 2\mu\frac{1+\nu}{1-\nu}f\cdot\frac{h_s}{h+h_s} \qquad \text{(film)}$$

$$\sigma^s_{yy} = \sigma^s_{zz} = -2\mu\frac{1+\nu}{1-\nu}f\cdot\frac{h}{h+h_s} \qquad \text{(substrate)} \qquad (4.2.3)$$

where the x, y and z axes are parallel to $[\bar{1}00]$, $[0\bar{1}1]$ and [011] respectively.

If the substrate thickness (h_s) » film thickness (h), equation (4.2.3) can be simplified as

$$\sigma^f_{yy} = \sigma^f_{zz} = 2\mu\frac{1+\nu}{1-\nu}f$$

$$\sigma^s_{yy} = \sigma^s_{zz} = 0 \qquad (4.2.4)$$

This is the equation (2.1.1)

In these expressions, f is the misfit Δa/a between the lattice parameters of $In_{0.25}Ga_{0.75}As$ and InP (f = 0.02 in this study), and identical elastic constants are assumed for the film and substrate. Two conditions have to be satisfied for crack nucleation. A necessary condition is that the stress at the surface of the film is at least equal to the (011) cleavage stress (σ_c). If h_s » h, and the surface remains planar, this condition can be written as $2\mu\frac{1+\nu}{1-\nu}f \geq \sigma_c$. In a surface roughened film this expression will underestimate the value of σ_c as the maximum stress will be highest at the valleys of the roughened surface. If this effect is ignored, a value of $\sigma_c \leq$ E/34 is obtained by substituting E (Young's Modulus) for $2\mu(1+\nu)$, 0.02 for f and 0.32 for ν.

A second, and sufficient condition for crack formation, leading to the critical thickness concept, is that the energy of the system should be lowered by the introduction of a crack. As discussed in Chapter 2, the elastic energy relieved by the crack (E_e) can be calculated using (2.1.9). For a single crack terminating at the interface,

$$E_e = \int_0^h G dx = \int_0^h \frac{K^2}{E} dx = \int_0^h \frac{\left(1.122\sigma\sqrt{\pi x}\right)}{E} dx = \frac{1.98\sigma^2 h^2}{E} \qquad (4.2.5)$$

Substituting $E = 2\mu(1+\nu)$ and equation (4.2.4) for σ into equation (4.2.5), we have

$$E_e = \frac{3.96\mu(1+\nu)f^2 h^2}{(1-\nu)^2} \qquad (4.2.6)$$

Comparing this equation with equation (2.1.4), it is found that the elastic energy calculated by equation (4.2.6) is 1.98/(1-ν) (≈ 2.8, if ν = 0.3) times that given by equation (2.1.4). Equation (2.1.4) underestimates the elastic energy relieved by the crack. The energy associated the fracture resistance Γ_f is

$$E_s = \Gamma_f h \qquad (4.2.6)$$

The critical thickness h_c is obtained by solving $E_e = E_s$, giving

$$h_c = \frac{\Gamma_f (1-\nu)^2}{3.96(1+\nu)\mu f^2} \qquad (4.2.7)$$

Substituting in values for ν and μ from Table 4.2, 0.02 for f, and knowing that h_c lies between 10 and 20 nm, we find that Γ_f lies between

$$1.32 \text{ J/m}^2 < \Gamma_f < 2.64 \text{ J/m}^2$$

For a purely elastic fracture $\Gamma_f = 2\gamma$: at room temperature 2γ is estimated to be 1.54 J/m^2 for $In_{025}Ga_{0.75}As$ (Table 4.2). At the growth temperature (480°C), the surface energy will be

lower than this. Assuming a temperature dependence $\partial\gamma/\partial T = -0.1 mJ/m^2 (°C)^{-1}$ (Tu *et al.* 1992), $2\gamma = 1.45 J/m^2$ at the growth temperature. This value lies within the range for Γ_f found experimentally, suggesting that the initial fracture process is essentially elastic in nature. Neither of equation (2.1.3) nor equation (2.1.6) for h_c in Chapter 2, gives as good agreement with the experimental data as does equation (4.2.7).

4.2.2 Multiple cracking and substrate cracking

The classical analyses of film cracking assume that arrays of parallel cracks spread across the film with little or no penetration of the crack into substrate (Thouless 1990; Thouless *et al.* 1992; Beuth 1992; Hutchinson and Suo 1991; Ye *et al.* 1992). Cracks start to interact when the ratio of the crack spacing (d) to film thickness (h) is less than about 8 (Thouless 1990; Thouless *et al.* 1992), and an equilibrium spacing (< 8h) can be achieved by minimizing the total energy of the system, including the crack-crack interaction energy term (Thouless *et al.* 1992) In our experiments, d/h lies between about 20 and 30, so crack interactions can be neglected. Nevertheless, a further reduction in energy can be achieved by allowing the crack to penetrate into the substrate. Although Ye *et al.* (1992) state that crack penetration into the substrate is negligible when $\Gamma_s/\Gamma_f \approx 1$ (Γ_s is the fracture resistance of the substrate), our results suggest otherwise. The total strain energy (E_c) released by substrate cracking can be estimated from the stress-intensity factors given by Tada *et al.* (1985) as discussed in Chapter 2. For a crack of total length c (see Fig.2.2b), E_c is obtained using equations (2.1.9), (2.1.11) and (2.1.16) as follows

$$E_e = \frac{1.98\sigma^2 c^2}{E} \qquad c \le h$$

$$E_e = \frac{1.98\sigma^2 h^2}{E} + \frac{4\sigma^2}{\pi E}\int_h^c x\left[\sin^{-1}\left(\frac{h}{x}\right)F\left(\frac{h}{x}\right)\right]^2 dx \qquad c \ge h \qquad (4.2.8)$$

The total change in energy of the system is

$$\Delta E = -E_e + \Gamma_f c \qquad c \le h$$

$$= -E_e + \Gamma_f h + \Gamma_s (c-h) = -E_e + \Gamma c, \text{ if } \Gamma_f = \Gamma_s \qquad c \ge h \qquad (4.2.9)$$

and the crack arrests when $(\partial \Delta E)/(\partial c) = 0$.

In order to compare the experimental observation with the prediction of equation (4.2.8) and (4.2.9), we should note that the stress in the film progressively relaxed as growth proceeds by four competing processes: cracking, twinning, 60° dislocation formation and surface roughening. Since it is difficult to calculate the stress we have chosen to estimate σ from the experimental observations of c and δ_0 (the crack opening displacement) as a function of h (see Table 4.1). The method of calculation is indicated in Fig.4.7a, which shows ΔE plotted as a function of c/h for a film of thickness h = 20nm at three stress values (1.8, 2 and 2.2 GPa). ΔE is initially positive but becomes negative at the critical thickness given by equation (4.2.7) with $\Gamma_f = 1.45 J/m^2$. The energy released passes through a minimum position before slowly rising to become zero again. It seems reasonable to assume that the stable crack position in the substrate corresponds to this minimum. For the 20 nm thick film, c/h $\approx$ 2 and a stress level of 2.2 GPa provides a good fit to the data. The stress in the uncracked film (E/34) is 2.26 GPa, so this estimate appears plausible. The predicted value of δ_0 from equation (2.1.18) in Chapter 2, 5.4 nm, also compares favourably with the experimental of 5.8 nm (see Table 4.1).

The same procedures were followed for the 100nm and 200nm thick films (c/h = 3 and 2.8 respectively). Stress levels of 1.2 GPa (Fig.4.7b) and 0.85 GPa (Fig.4.7c) were estimated for the effective stress acting in these films. Again these numbers appear reasonable, and point to the progressive relaxation of the film stress by plastic flow and surface roughening. The predicted crack opening displacements, 16 and 22 nm respectively, are slightly greatly than the average measured values, 10 and 15 nm. However, given the various assumptions made (isotropic elasticity, isotropic surface energies in the film and substrate and a uniform far field stress acting on each crack), the agreement is still satisfactory.

Two factors probably contribute to the deviation of the crack path from {110} to {111} in the substrate. The {111} surface energy of III-V compounds is about 13% lower than the {110}values (see Table 2). Secondly the "T-stress", that is the stress acting parallel to the crack when it penetrates into the substrate, can influence the crack path (Hutchinson and Suo 1991; Ye *et al.* 1992)

4.2.3 Anisotropy of cracking

The InGaAs/InP system studied in this work represents an extreme case where stress relief in one of the two orthogonal <011> directions first occurs by twinning (Fig.4.3), while in the other direction it occurs by cracking (Fig.4.1). Similar observations have been reported by Olsen *et al.* (1974) and Murray *et al.* (1996). The critical thickness for the nucleation of stacking faults or twins (Chapter 6) in this system is very similar to the critical thickness for crack formation calculated above, equation (4.2.7). Given the approximate nature of these calculations, it is impossible to decide whether one mechanism would be favoured over

Figure 4.7

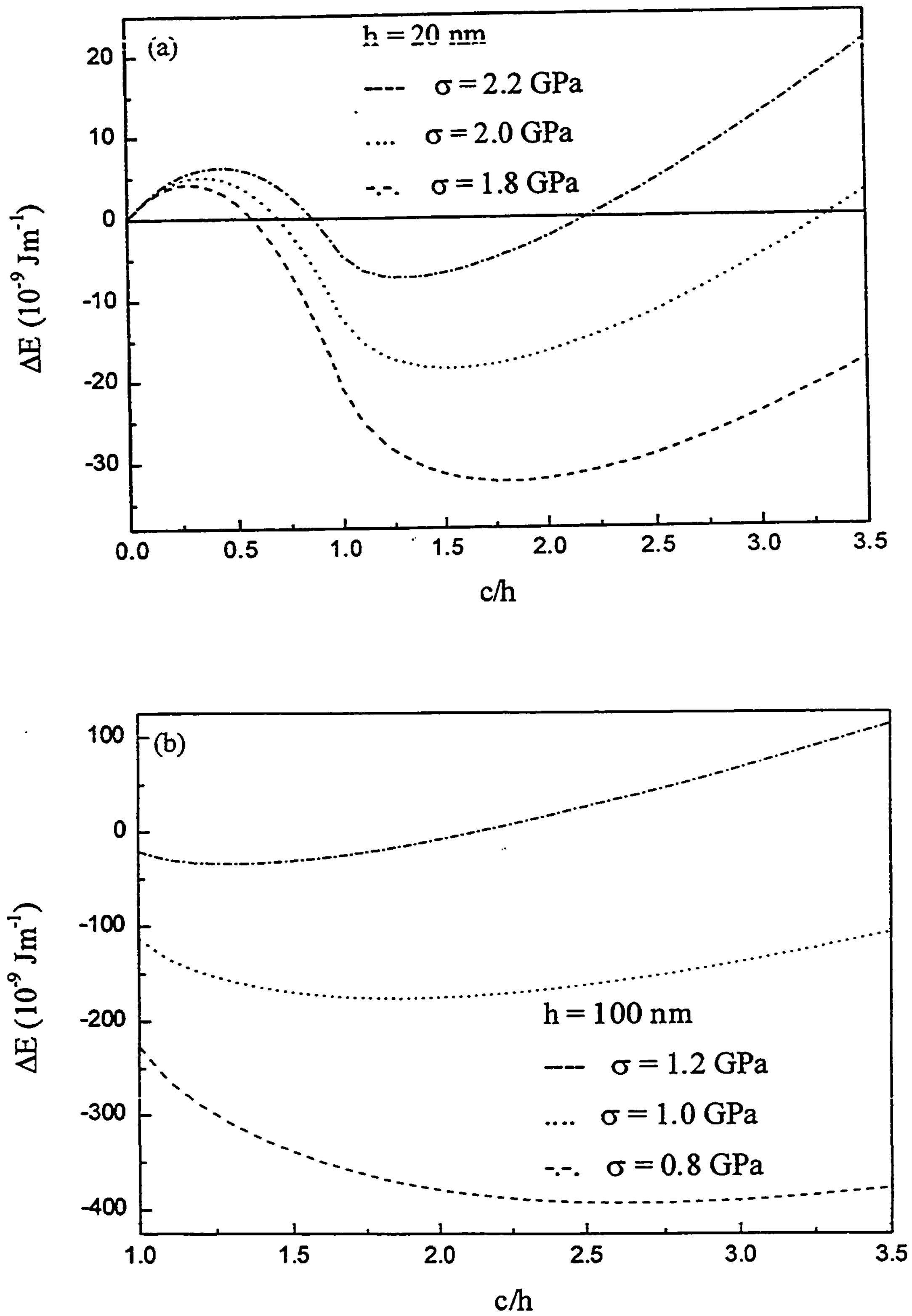

Figure 4.7 (continued)

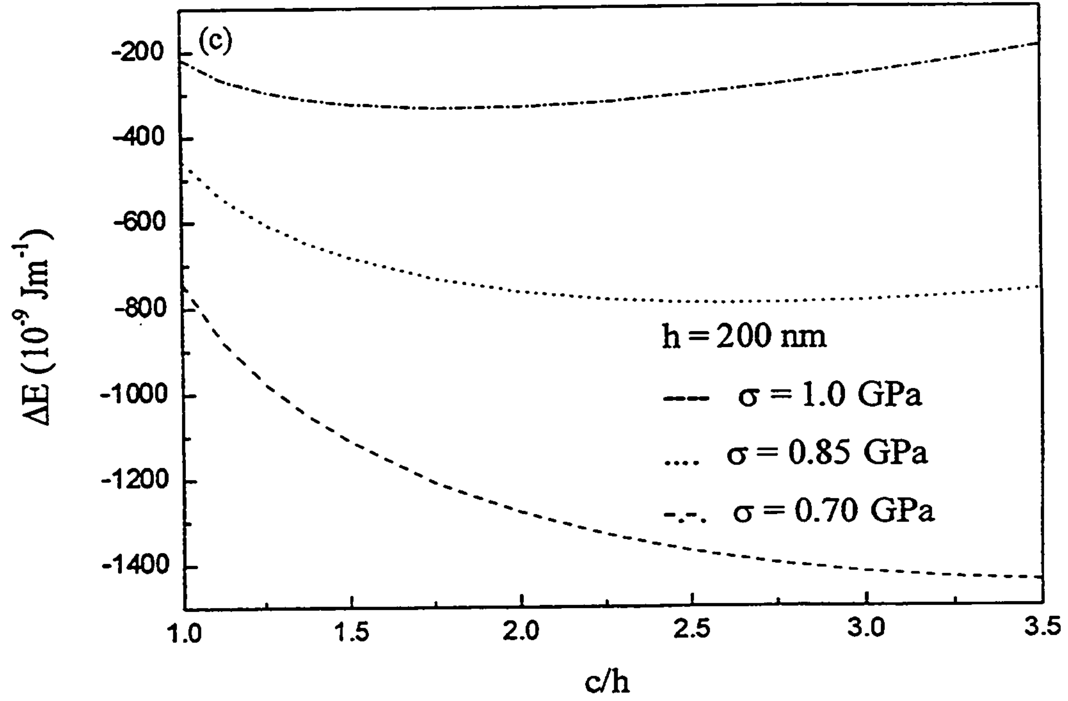

Plots of ΔE [equation (4.2.9)] vs c/h at different stress levels for film thickness: (a) h = 20 nm; (b) h = 100 nm; (c) h = 200 nm

another. The probable explanation for the observed asymmetry lies in the different nucleation characteristics of α and β dislocations (DeCooman and Carter 1989; Kavanagh *et al.* 1988), and the role played by surface roughening in both stacking fault (twin) nucleation and cracking.

4.2.4 Crack healing

The single most intriguing observation of this study was the progressive drop in the density of cracks as film growth proceeds in the range from 20 nm to 200 nm, followed by the total elimination of cracks in the 500 nm thick film. These were such unexpected observations that a number of repeat growths and cross-checks were carried out to ensure that the results were reproducible and representative. The data presented in Table 4.1 demonstrate that a destructive sample preparation technique, cross-sectional transmission electron microscopy, and a non-destructive technique, scanning electron microscopy, give essentially identical crack densities at each thickness. Similar results (not presented here) were observed with atomic force microscopy. The cross-sectional work also showed that the cracks were not being "buried" during growth, as reported by Murray *et al.* (1996).

The initial stage of stress relief in 20 nm thick film occurred by cracking along $(0\bar{1}1)$ planes, and by twinning on (111) and $(\bar{1}11)$ planes. As growth of the film continued, both perfect (a/2)<011> dislocations and stacking faults bounded by (a/6)<112> partial dislocations were observed in the [011] cross-sections (see Fig.4.8). Strain relief by plastic flow becomes a competitive mechanism to crack formation in this direction. The details of this process are unclear, but it might be associated with the formation of the dislocations at the

Figure 4.8

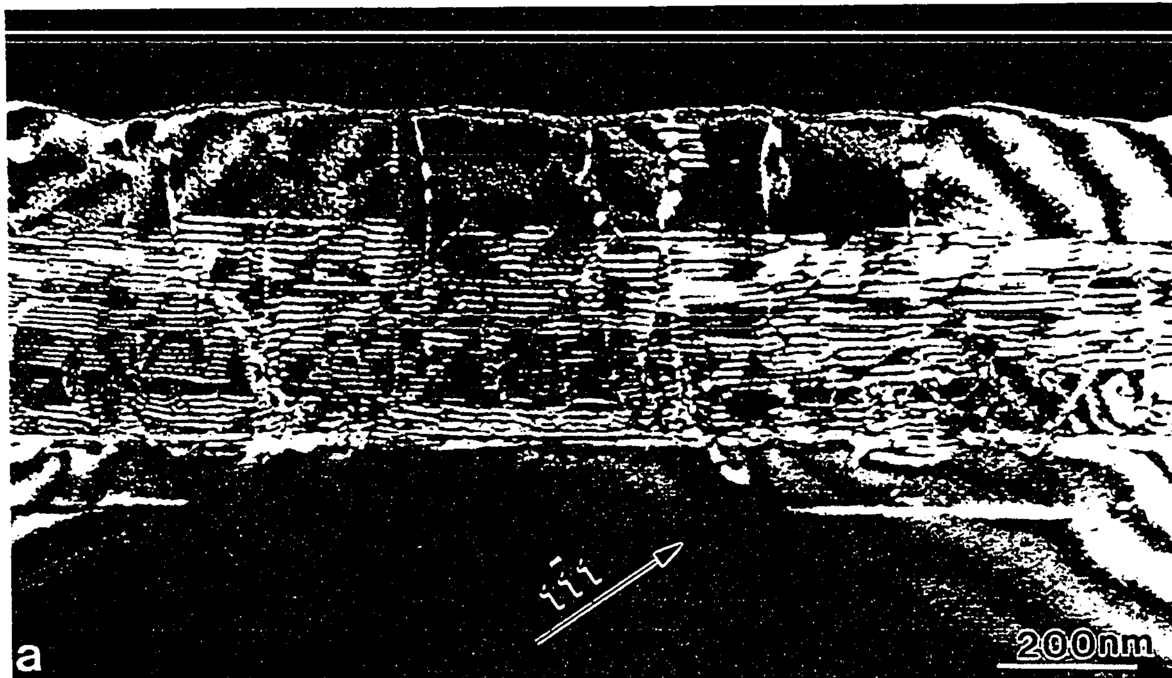

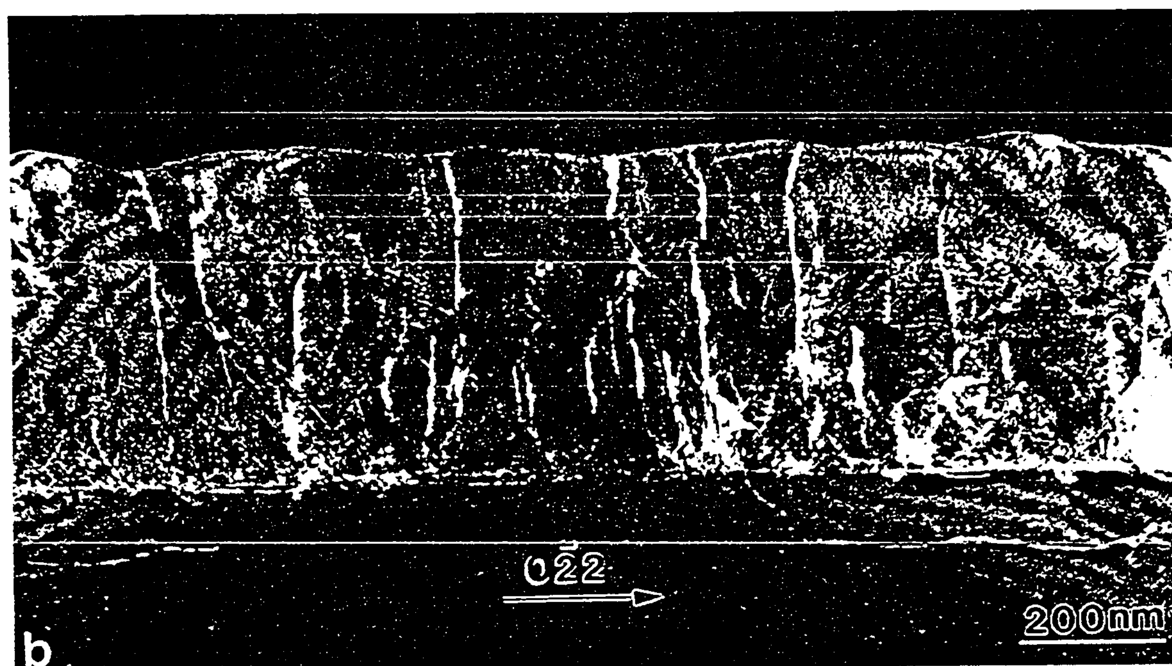

Weak beam dark field images showing a high density of stacking faults and perfect dislocations in 500 nm thick layer: (a) $g = 1\bar{1}1$; (b) $g = 0\bar{2}2$.

crack tips (Fig.4.2), interacting and multiplying as growth proceeds. Whatever the origin of the dislocations seen in Fig.4.8, they must reduce the residual elastic strain (and stress) acting on the cracks in the epilayer.

The crack healing process itself is a discontinuous one, i.e. there is not a spontaneous healing at the crack front that simply reverse the interatomic bond breaking that must accompany crack formation. Instead the cracks appear to heal from the ends of the sample (or at discrete locations along the crack front). This is most obvious on comparing the crack morphology in the 20 nm thick film, where long continuous cracks are observed, with the 200 nm thick film where short crack segments or crack terminations are frequently observed (Fig.4.9). Crack healing is driven by the difference in chemical potential of atoms at the free surface and crack tip. As plastic flow starts to relieve the stresses acting on the cracks, the capillary stress at the crack tip ($\sim\gamma\kappa$, where γ is the surface energy and $\kappa=1/\rho_1 + 1/\rho_2$ with ρ_i the principal radii of curvature) could become greater than the residual elastic stress. There would then be a driving force for surface diffusion of atoms to the crack tip and crack healing. The extreme purity of the atmosphere of the growth chamber in the molecular beam epitaxy process, and the constant supply of atoms from the surrounding atmosphere during growth would both aid crack healing.

Support for this hypothesis comes from energy dispersive x-ray analysis of the crack tips in TEM cross-sections. Figure 4.6 shows the x-ray spectrum from the crack tip region in the substrate at some distance from the epilayer. Both Ga and As were detected at this location in the 100 and 200 nm thick samples, but not in the 20 nm thick sample. These atoms could only come from the MBE growth atmosphere and diffuse to the crack tip along the crack surfaces.

Figure 4.9

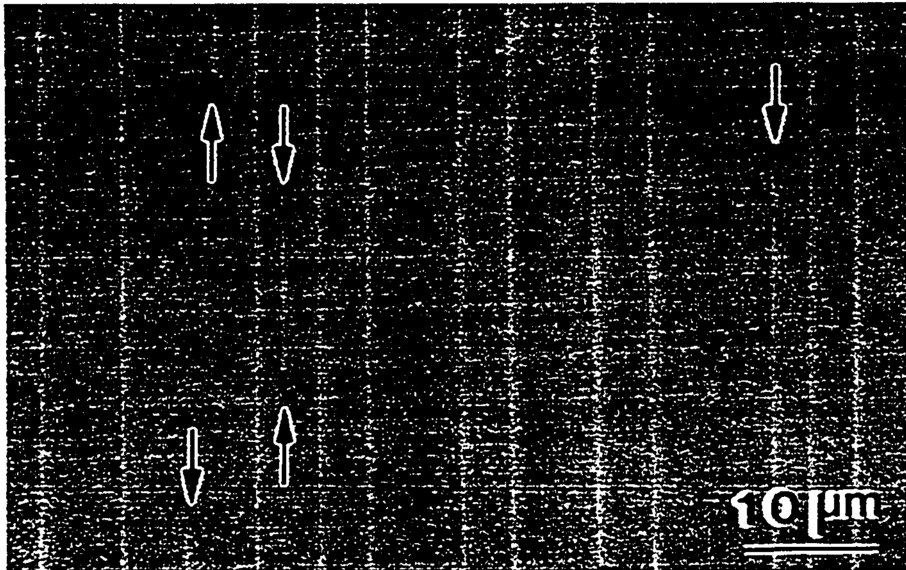

SEM image of the surface of 200 nm thick layer showing short cracks and crack terminations.

If crack healing turns out to be commonly found in the growth of III-V compounds, it highlights the pitfalls in relying solely on an energy criterion to derive the critical film thickness for cracking. One might conclude from the observation of films whose thickness >> h_c that cracking had not occurred, whereas (as shown here) the films have first cracked and then the cracks have healed on further film growth.

* This Chapter is based on the publication "Cracking phenomena in $In_{0.25}Ga_{0.75}As$ films on InP substrates" by X. Wu and G.C. Weatherly, *Acta Mater.*, Vol.47, No.12, pp. 3383-3394, 1999

Chapter 5

The surface topography of cracks in strained InGaP films

5.1 Observations

In the previous Chapter, it was shown that the cracks are seen via topographic contrast in the optical and scanning electron microscopes. In this Chapter, a more detailed study of the surface topography of cracks in strained films is presented. A two percent tensile strained 100nm thick $In_{0.72}Ga_{0.28}P$ film grown on an InP substrate was chosen for this study. A variety of crack morphologies were found in the film, as shown by the [011] XTEM observations of Fig.5.1. The majority of the cracks penetrated some distance into the substrate along the $(0\bar{1}1)$ plane, before deviating and arresting on the $(1\bar{1}1)$ or $(\bar{1}\bar{1}1)$ planes (Fig.5.1a). However, on occasion, cracks were observed to arrest after penetrating into the substrate only along the $(0\bar{1}1)$ plane (Fig.5.1b). The stress relaxation mechanisms observed in the orthogonal $[0\bar{1}1]$ section were a combination of surface roughening and twinning (Fig.5.1c). Overall the strain relaxation behaviour in this film is the same as the films studied in Chapter 4.

The atomic force microscopy (AFM) observations from the same set of cracks are summarized in Figs.5.2 and 5.3. If a relatively large area (10μm×10μm) was scanned, the normal surface displacement associated with the cracks was readily detected, but the cracks themselves (and the crack opening displacement) were not seen. This cracking process associated with a normal displacement of the free surface of the tensile strained film in the vicinity of the crack is also reported by Murray *et al.* (1996). They used this observation to estimate the amount of stress (strain) relaxation associated with film cracking. The positions

Figure 5.1

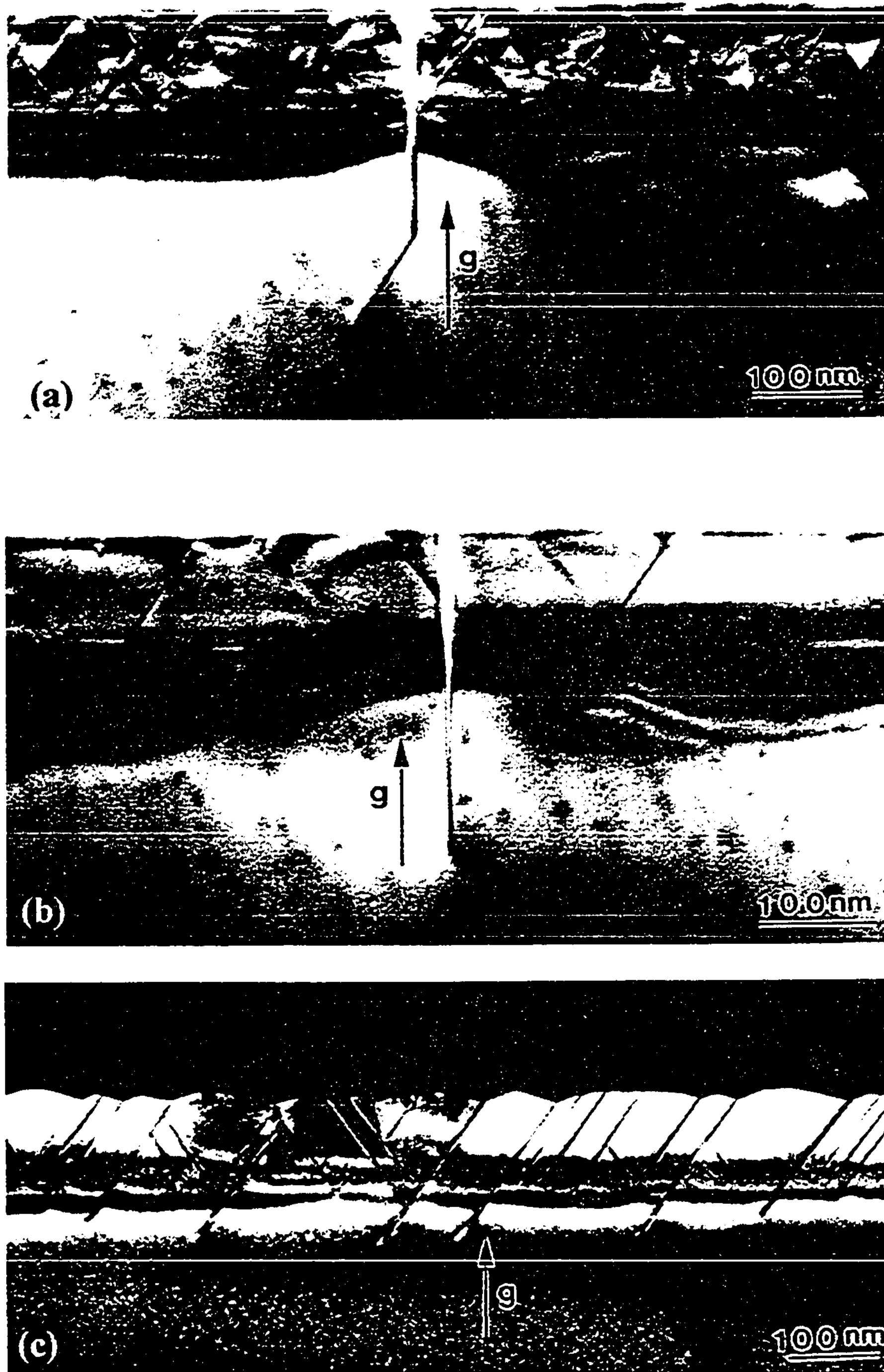

g = 400 cross-section TEM images. (a) The crack arrests on $(1\bar{1}1)$ plane after penetrating into substrate along $(0\bar{1}1)$ in [011] cross-section. (b) The crack arrests on $(0\bar{1}1)$ plane after penetrating into the substrate along $(0\bar{1}1)$ in [011] cross-section. (c) Planar defects and surface undulation in $[0\bar{1}1]$ cross-section.

of the cracks are marked by arrows in Fig.5.2a, and the corresponding surface topography, as measured in a direction normal to the plane of the crack is shown in Fig.5.2b. The assessment of the overall surface morphology in these films is complicated by the roughening associated with surface faceting on (411) and $(4\bar{1}\bar{1})$ planes (Okada *et al.* 1997). This phenomenon is clearly seen in the image of Fig.5.3a. However, measurements of the surface displacement associated with cracking were obtained from line traces where there was no interference from the surface roughening. AFM images taken at higher magnification showed both the crack opening displacement and the normal displacement (Figs.5.3a and b).

Table 5.1 summarizes measurements of the cracking opening displacement (δ_0) (see Chapter 4 for the definition of δ_0) and maximum normal surface displacement (L) obtained from a number of AFM images of cracks in the 100nm thick $In_{0.72}Ga_{0.28}P$ film. The average value of δ_0/L is approximately 3.

Table 5.1 Summary of AFM observations on 100nm thick $In_{0.72}Ga_{0.28}P$ film

δ_0 (nm)	L (nm)
18.5	5.2
19.5	5.2
20.5	6.0
20.5	6.3
19.5	7.1
19.7	7.5
	6.0
	7.1
	5.2
	6.0
19.7±0.7	6.2±0.8

Figure 5.2

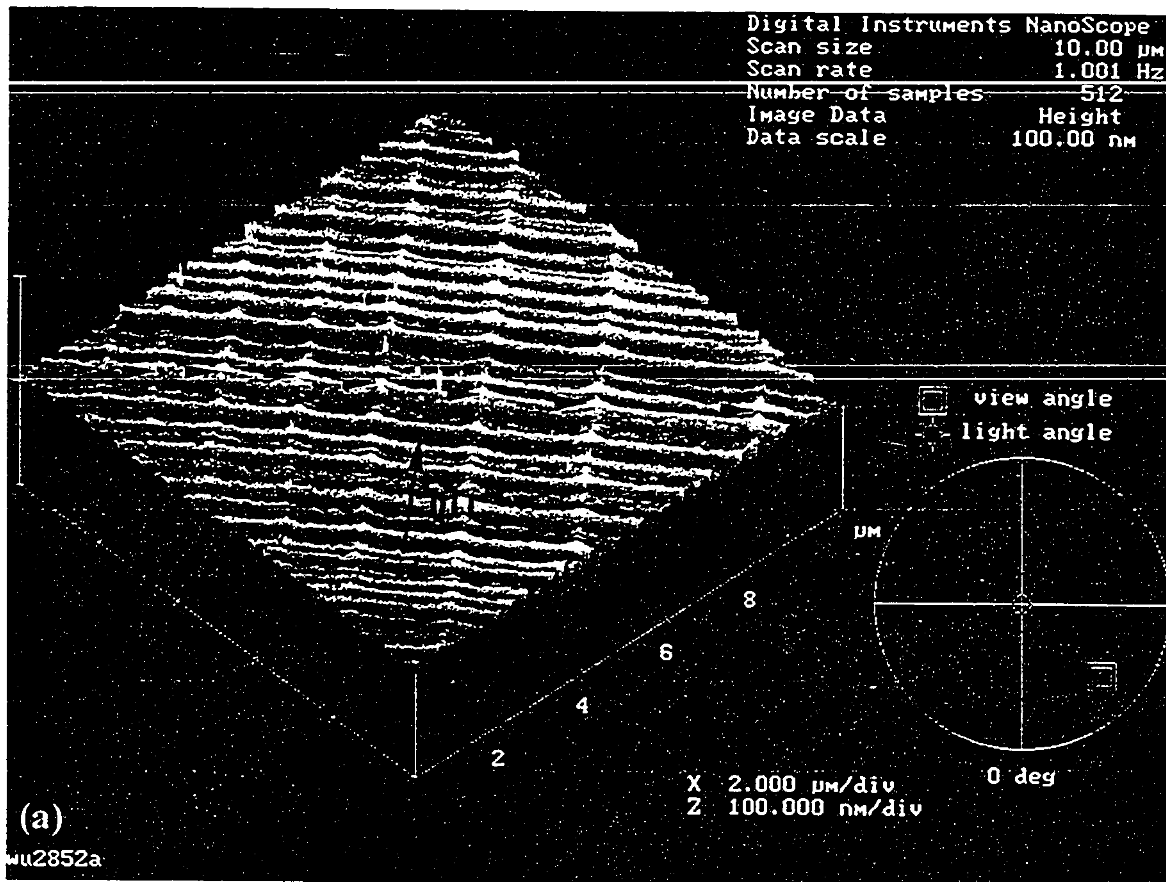

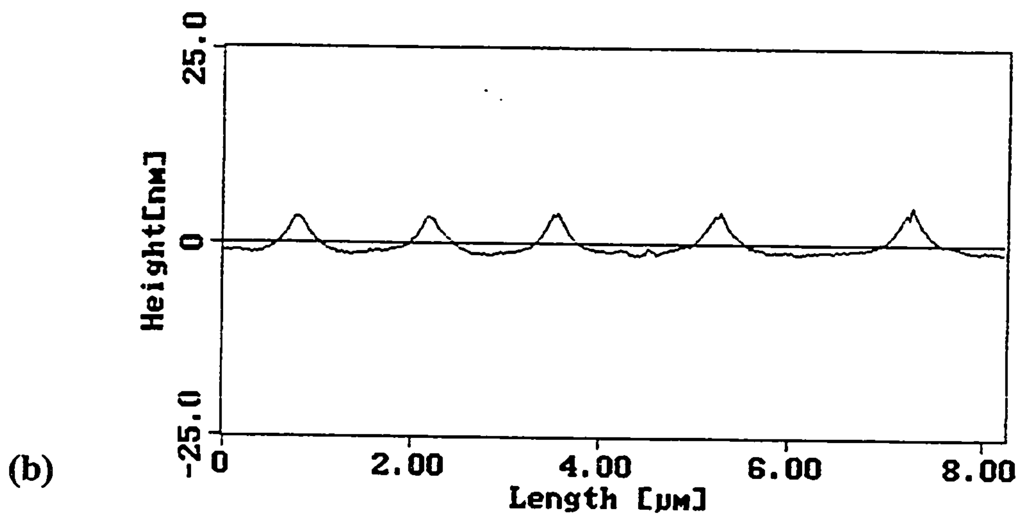

AFM image and surface profile. (a) 8 cracks (indicated by arrows) running along [011] direction. The normal surface displacement associated with the cracks is visible. (b) Surface profile along the direction perpendicular to the [011] direction.

Figure 5.3

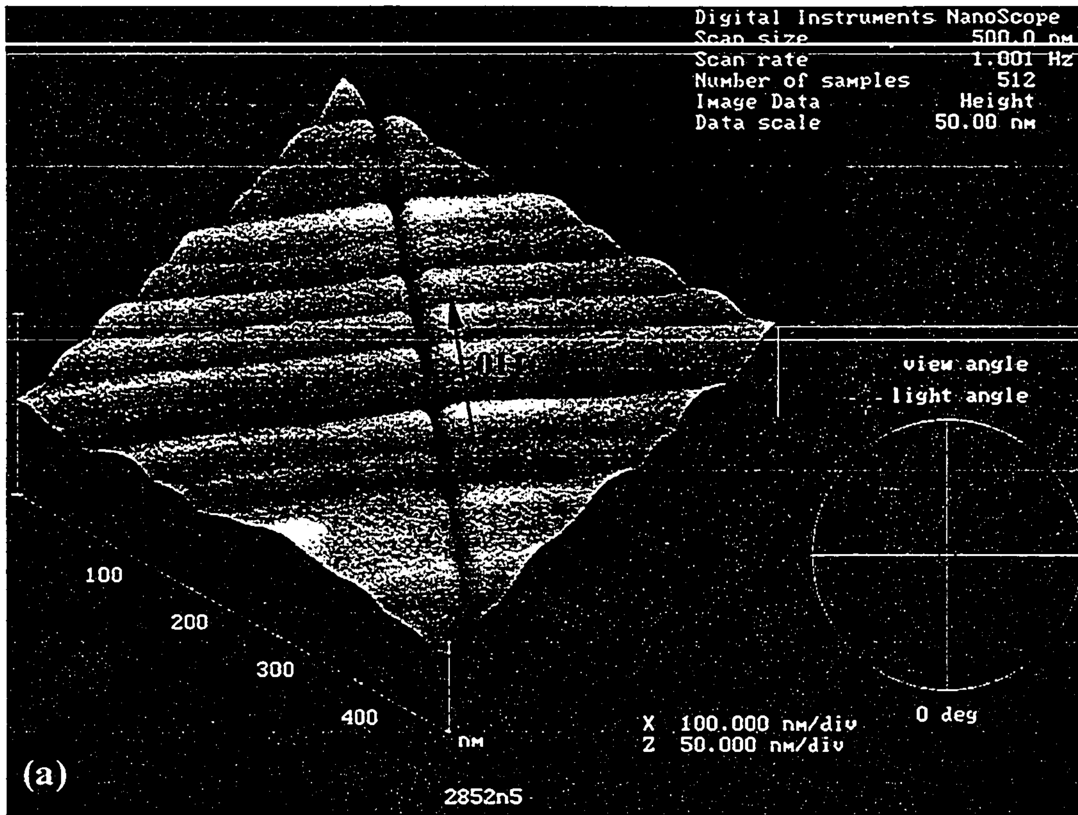

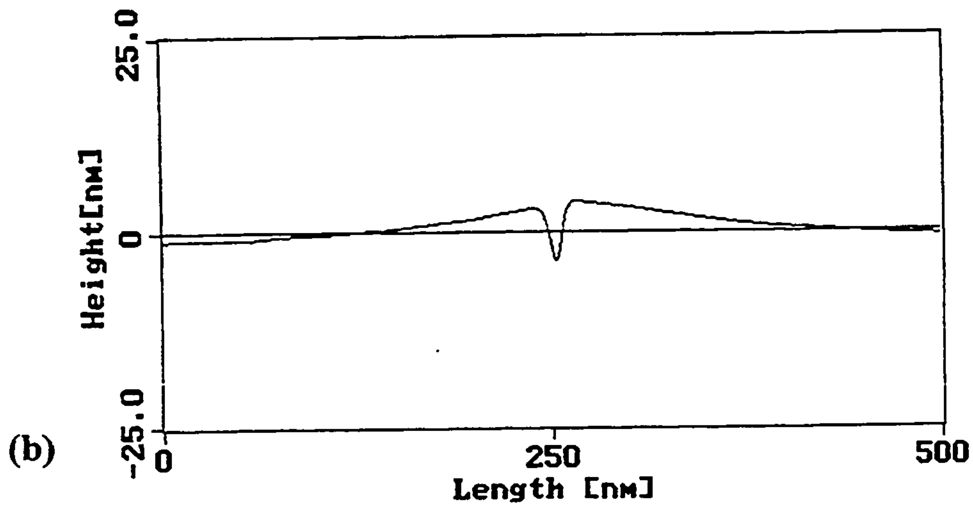

AFM image and surface profile. (a) A crack running along [011] direction. The crack opening displacement is visible. (b) Surface profile along the direction perpendicular to the [011] direction.

5.2 Discussion

In this section, a dislocation analogue for a surface crack in a thin epitaxial film, within the framework of isotropic elasticity, is used to account for the ratio of the crack opening displacement (δ_0) to the normal surface displacement (L) associated with the crack.

5.2.1 Single crack in an infinite medium

For completeness, consider first a crack with total length 2c subjected to mode I loading (normal stress σ) in an infinite isotropic medium (Fig.5.4a). The dislocation analogue for this crack is shown in Fig.5.4b. In this analogue, the crack is replaced by a double dislocation pileup. If the Burgers vector of the individual dislocation in the pileup is b, and the dislocation distribution function in the pileup is f(x'), the expression bf(x')dx' represents the Burgers vector of the dislocation array within the length dx' at x = x'. In an infinite medium, an edge dislocation with Burgers vector **b** = (0,b,0) located at (h,0) has the following stress fields (Head 1953b):

$$\sigma_{xx} = \frac{\mu b}{2\pi(1-\nu)}\left\{\frac{(x-h)\left[(x-h)^2 - y^2\right]}{\left[(x-h)^2 + y^2\right]^2}\right\} \quad (5.2.1a)$$

$$\sigma_{yy} = \frac{\mu b}{2\pi(1-\nu)}\left\{\frac{(x-h)\left[(x-h)^2 + 3y^2\right]}{\left[(x-h)^2 + y^2\right]^2}\right\} \quad (5.2.1b)$$

$$\sigma_{xy} = \frac{\mu b}{2\pi(1-\nu)}\left\{\frac{y\left[(x-h)^2 - y^2\right]}{\left[(x-h)^2 + y^2\right]^2}\right\} \quad (5.2.1c)$$

where μ and ν are the shear modulus and Poisson's ratio respectively.

When y = 0, these three expressions reduce to

Figure 5.4

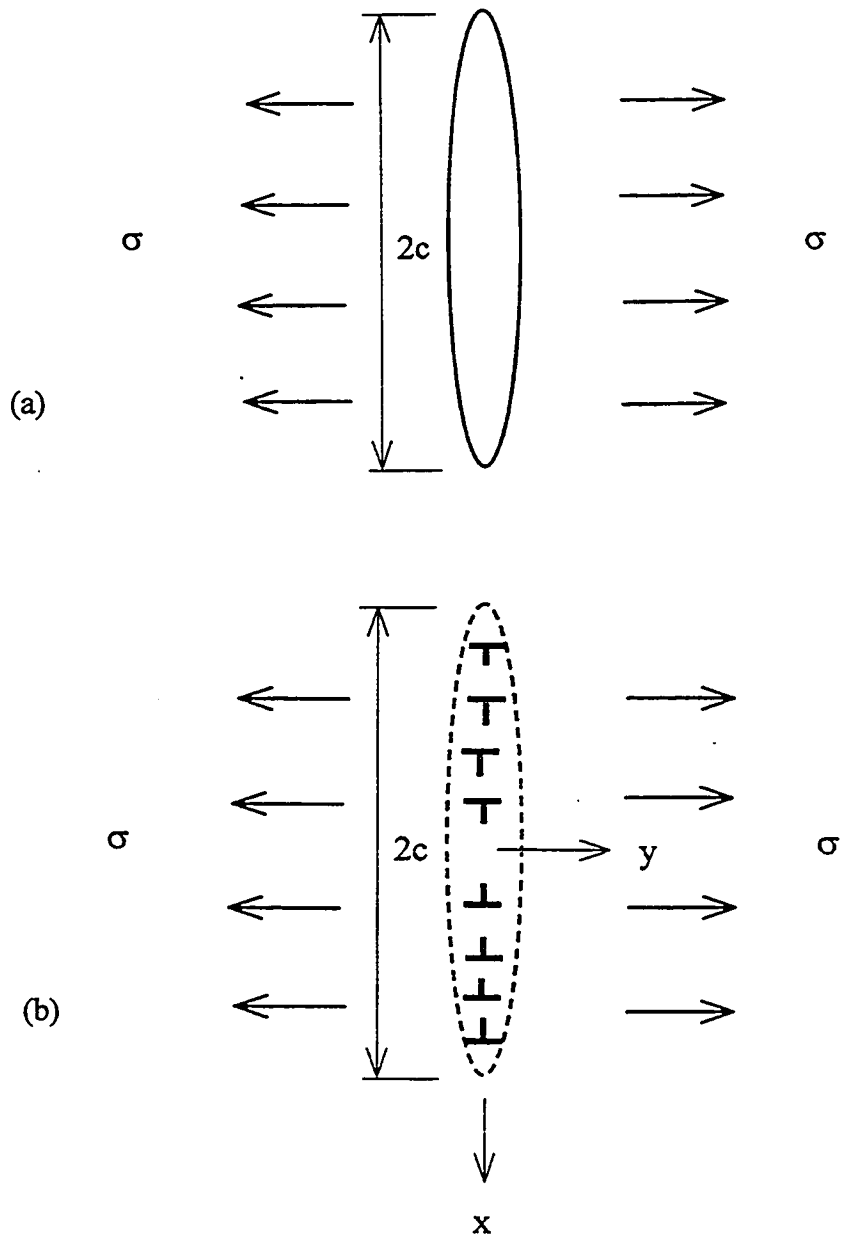

The geometry of the crack in an infinite medium (a) and the dislocation analogue (b)

$$\sigma_{xx} = \frac{\mu b}{2\pi(1-\nu)}\left(\frac{1}{x-h}\right) \tag{5.2.2a}$$

$$\sigma_{yy} = \frac{\mu b}{2\pi(1-\nu)}\left(\frac{1}{x-h}\right) \tag{5.2.2b}$$

$$\sigma_{xy} = 0 \tag{5.2.2c}$$

For the individual dislocations in the pileup to be in equilibrium, the climb force produced by the stress σ and that caused by interaction with the other dislocations must balance (Hirth and Lothe 1982), i.e.

$$\sigma b = \frac{\mu b}{2\pi(1-\nu)}\int_{-c}^{c}\frac{bf(x')dx'}{x-x'} \tag{5.2.3}$$

Solving the above equation, we have

$$f(x') = \frac{2(1-\nu)\sigma}{\mu b}\frac{x'}{\sqrt{c^2-x'^2}} \tag{5.2.4}$$

For the crack in Fig.5.4a, classical fracture mechanics gives the crack opening profile 2u(x) and the stress intensity factor K as (Tada *et al.* 1985)

$$2u(x) = \frac{4\sigma}{\overline{E}}\sqrt{c^2-x^2} \tag{5.2.5}$$

and

$$K = \sigma\sqrt{\pi c} \tag{5.2.6}$$

The crack opening profile can also be computed using the dislocation analogue as follows:

$$\int_{x}^{c} bf(x')dx' = \frac{2(1-\nu)\sigma}{\mu}\int_{x}^{c}\frac{x'}{\sqrt{c^2-x'^2}}dx' = \frac{2(1-\nu)\sigma}{\mu}\sqrt{c^2-x^2} \tag{5.2.7}$$

Substituting $\mu = E/2(1+\nu)$ and $E = \overline{E}(1-\nu)^2$ into equation (5.2.7), we get exactly the same equation as equation (5.2.5) for the crack opening profile. Moreover by solving equation

$u(x)=\frac{4}{E}K\sqrt{\frac{c-x}{2\pi}}$ (Gao *et al.* 1999), we get an identical value for K as equation (5.2.6). The crack opening displacement at the crack center x = 0 (δ_0) is given by:

$$\delta_0 = 2u(0)=\frac{4\sigma c}{E}=\int_0^c bf(x')dx' \quad (5.2.8)$$

5.2.2 Single crack at the film surface

The geometry of a surface crack in a thin epitaxial film is shown in Fig.5.5a, with the dislocation analogue in Fig.5.5b. The approach used in the previous sub-section can be used to solve the dislocation analogue for the surface crack. The stress field of an edge dislocation near a free surface should be used for this propose. In a semi-infinite medium with a free surface at x = 0, an edge dislocation with Burgers vector **b** = (0,b,0) located at (h,0), i.e. a distance h from the free surface has the following stress fields (Head 1953b):

$$\sigma_{xx}=\frac{\mu b}{2\pi(1-\nu)}\left\{\frac{(x-h)\left[(x-h)^2-y^2\right]}{\left[(x-h)^2+y^2\right]^2}-\frac{(x+h)\left[(x+h)^2-y^2\right]}{\left[(x+h)^2+y^2\right]^2}+2h\frac{(3x+h)(x+h)^3-6x(x+h)y^2-y^4}{\left[(x+h)^2+y^2\right]^3}\right\}$$

(5.2.9a)

$$\sigma_{yy}=\frac{\mu b}{2\pi(1-\nu)}\left\{\frac{(x-h)\left[(x-h)^2+3y^2\right]}{\left[(x-h)^2+y^2\right]^2}-\frac{(x+h)\left[(x+h)^2+3y^2\right]}{\left[(x+h)^2+y^2\right]^2}-2h\frac{(x-h)(x+h)^3-6x(x+h)y^2+y^4}{\left[(x+h)^2+y^2\right]^3}\right\}$$

(5.2.9b)

$$\sigma_{xy}=\frac{\mu b}{2\pi(1-\nu)}\left\{\frac{y\left[(x-h)^2-y^2\right]}{\left[(x-h)^2+y^2\right]^2}-\frac{y\left[(x+h)^2-y^2\right]}{\left[(x+h)^2+y^2\right]^2}+4hxy\frac{3(x+h)^2-y^2}{\left[(x+h)^2+y^2\right]^3}\right\}$$

(5.2.9c)

Figure 5.5

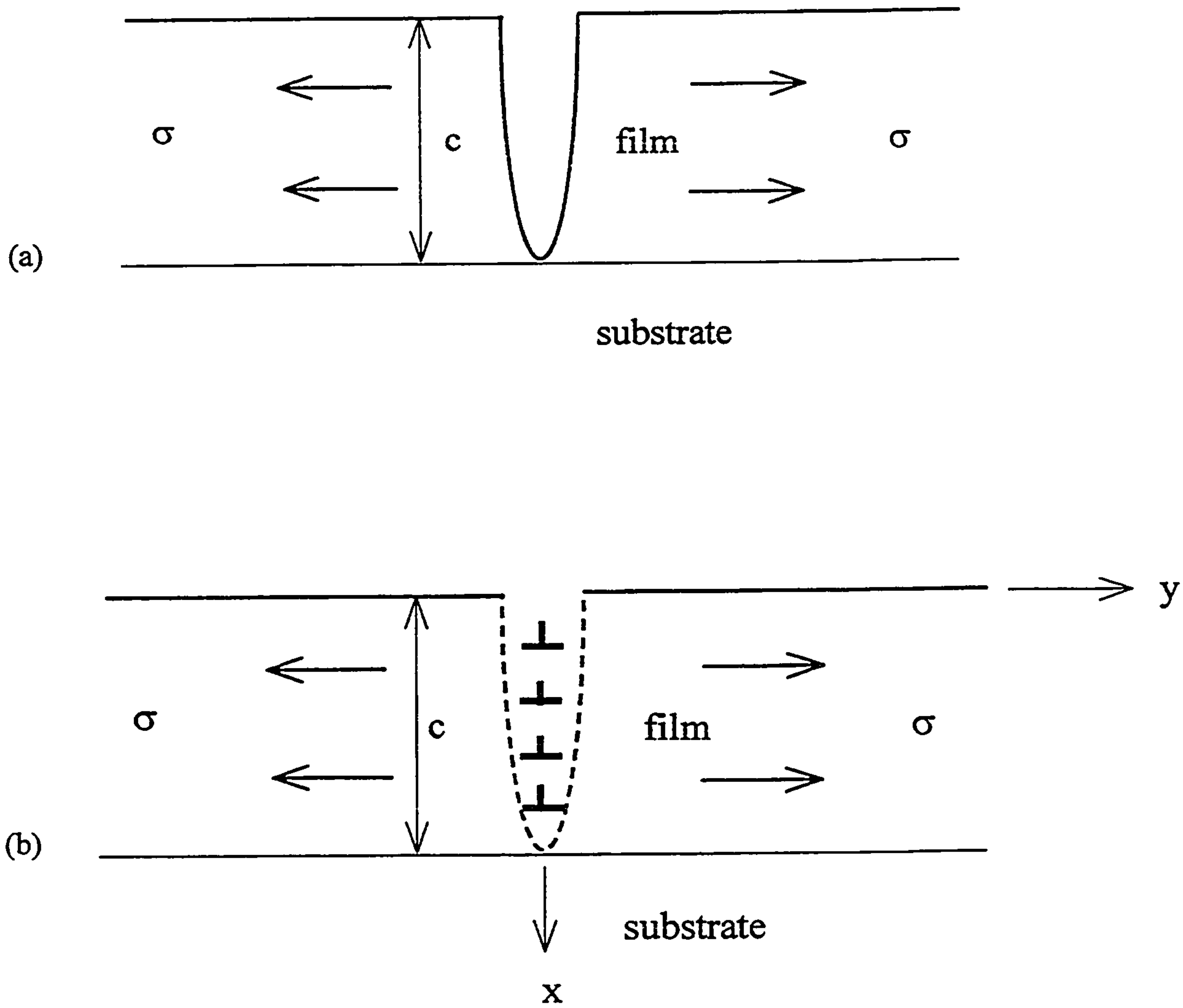

The geometry of the surface crack in the film (a) and the dislocation analogue (b).

where μ and ν are the shear modulus and Poisson's ratio respectively.

When $y = 0$, these three expressions reduce to

$$\sigma_{xx} = \frac{\mu b}{2\pi(1-\nu)}\left\{\frac{1}{x-h} - \frac{1}{x+h} + 2h\frac{3x+h}{(x+h)^3}\right\} \tag{5.2.10a}$$

$$\sigma_{yy} = \frac{\mu b}{2\pi(1-\nu)}\left\{\frac{1}{x-h} - \frac{1}{x+h} - 2h\frac{x-h}{(x+h)^3}\right\} \tag{5.2.10b}$$

$$\sigma_{xy} = 0 \tag{5.2.10c}$$

For the individual dislocations in the pileup to be at equilibrium, the climb force produced by the stress σ and that caused by interaction with the other dislocations must balance, i.e.

$$\sigma b = \frac{\mu b}{2\pi(1-\nu)}\int_0^c bg(x')\left[\frac{1}{x-x'} - \frac{1}{x+x'} - 2x'\frac{x-x'}{(x+x')^3}\right]dx' \tag{5.2.11}$$

where g(x') is the dislocation distribution function in the pileup shown in Fig.5.5b, and the term inside the square beackets comes from equation (5.2.10b).

Gao *et al.* (1999) have given the numerical solutions to equation (5.2.11). They used this analogy in a recent theoretical study of grain boundary "diffusion wedges", although they concentrated on time-dependent stress relaxation phenomena rather than cracking per se. It has been shown by Gao *et al.* (1999) that the crack opening displacement at the free surface,

$$\delta_0 = \int_0^c bg(x')dx' \approx \frac{5.8\sigma c}{E} \tag{5.2.12}$$

where E is Young's modulus. This result, as expected, is identical to the classical fracture mechanics result for δ_0 for a surface crack given by equation (2.1.15). Gao *et al.* have also given the numerical solutions to the dislocation analogue for the surface crack array in the thin film as shown in Fig.2.2c.

The dislocation analogy can also be used to estimate the surface displacements, u_x and u_y. For an edge dislocation with Burgers vector **b** = (0,b,0) located at a distance h from the free surface x = 0, u_x and u_y are found from Head's expressions (5.2.9a) and (5.2.9b) as:

$$u_x = \int \varepsilon_{xx} dx$$
$$= \frac{b}{4\pi(1-\nu)} \left\{ \frac{y^2}{\left[(x-h)^2 + y^2\right]} + \left(\frac{1}{2} - \nu\right) \ln\left[\frac{(x-h)^2 + y^2}{(x+h)^2 + y^2}\right] + \frac{4\nu h(x+h) - y^2 - 6hx - 4h^2}{(x+h)^2 + y^2} + \frac{4hy^2 x}{\left[(x-h)^2 + y^2\right]^2} \right\}$$

(5.2.13a)

$$u_y = \int \varepsilon_{yy} dy = \frac{b}{4\pi(1-\nu)} \left\{ -\frac{y(x-h)}{\left[(x-h)^2 + y^2\right]} - 2(1-\nu)\left[\arctan\left(\frac{y}{x+h}\right) - \arctan\left(\frac{y}{x-h}\right)\right] - \frac{4hxy(x+h)}{\left[(x-h)^2 + y^2\right]^2} \right\}$$
$$+ \frac{b}{4\pi(1-\nu)} \left\{ \frac{y\left(3h^2 + 13xh^2 + x^3 + 11x^2 h\right)}{\left[(x-h)^2 + y^2\right](x+h)^2} - \frac{4\nu hy}{\left[(x-h)^2 + y^2\right]} - \frac{6xhy}{\left[(x-h)^2 + y^2\right](x+h)} \right\}$$

(5.2.13b)

where $\varepsilon_{xx} = \frac{1}{2\mu}\left[(1-\nu)\sigma_{xx} - \nu\sigma_{yy}\right]$ and $\varepsilon_{yy} = \frac{1}{2\mu}\left[(1-\nu)\sigma_{yy} - \nu\sigma_{xx}\right]$.

At the free surface x = 0, the normal displacement (u_x) is given by

$$u_x = -\frac{b}{\pi} \frac{h^2}{h^2 + y^2} \qquad (5.2.14)$$

(The negative sign indicates that the surface relaxation corresponds to a local bulging of the surface, as observed).

The total normal displacement of the dislocation array as shown in Fig.5.5b is then given by

$$u = -\frac{h^2}{\pi\left(h^2 + y^2\right)} \int_0^c b g(x') dx' \qquad (5.2.15)$$

At y = 0,

$$u = -\frac{1}{\pi}\int_0^c bg(x')dx' \qquad (5.2.16)$$

Re-arranging the above equation, we have

$$\frac{\int_0^c bg(x')dx'}{u} = -\pi \qquad (5.2.17)$$

In equation (5.2.17), $|u|$ is identically equal to the experimental measurement L, while $\int_0^c bg(x')dx'$ is the crack opening displacement at the free surface (δ_0). So the dislocation analogy suggests that $|\delta_0/L| = \pi$. This is in excellent agreement with the average ratio of $\delta_0/L = 3.2$ found experimentally (see table 5.1).

The analysis leading to the conclusion $\delta_0/L = \pi$ will still hold for cracks that penetrate into the substrate without deviating (Fig.5.1b), but an asymmetry in the surface profile would be expected for cracks that deviate onto {111} planes before arresting. Indeed we have often observed a small asymmetry in the surface profiles (see e.g. Fig5.3b), but as most of the contribution to L comes from the bg(x')dx' components nearest to the surface, this will have little overall effect on the magnitude of L or on the ratio (δ_0/L).

Finally, it should be noted that the surface relaxation associated with the cracks is entirely consistent with the state of strain in the film prior to cracking. The film is in a state of biaxial tension prior to stress relief, so that the through-thickness strain (in the x-direction) is given by $-\frac{\nu}{1-\nu}\left(\varepsilon_{zz} + \varepsilon_{yy}\right)$, where ν is Poisson's ratio. It is the local relaxation of this strain in the neighborhood of the crack that leads to the surface profiles found by AFM. The same

effect is responsible for the visibility of the cracks I the SEM, although the crack-opening displacement itself is below the resolution of the SEM. The elastic strain energy released by cracking must be evaluated by the integral $-\frac{1}{2}\int_{\delta_b}^{\delta_0}\sigma\delta(x)dx$, as discussed in Chapter 4, where δ_b and δ_0 are the crack opening displacements at the film-substrate interface and free surface respectively (Hutchinson and Suo 1991, Ye *et al.* 1992).

* This Chapter is based on the publication "The surface topography of cracks in strained InGaP films" by X. Wu and G.C. Weatherly, *Phil. Mag. Lett.*, In press, 2000.

Chapter 6

Strain relaxation by 60° perfect dislocations, 90° partial dislocations/twinning and cracking

6.1 Observations

It has been shown in Chapters 4 and 5 that the misfit strain in 2% tensile strained $In_{1-x}Ga_xAs_yP_{1-y}$ films can be relieved by cracking or plastic flow. In this chapter, comparison of strain relaxation via 60° perfect dislocations, 90° partial dislocations (stacking fault/twinning) and cracking is presented. Again two percent tensile strained $In_{0.25}Ga_{0.75}As$ films with thicknesses of 10nm, 20nm, 100nm, 200nm and 500nm grown on (100) InP substrates were chosen for this study. Figure 6.1 shows $[0\bar{1}1]$ cross-section images of 10nm, 100nm, 200nm and 500nm thick films. A $[0\bar{1}1]$ cross-section image of the 20nm thick film is shown in Fig.4.3 in Chapter 4. A low-density of planar defects (stacking faults and twins) was observed in the 10nm thick film (Fig6.1a). As the film thickness increases to 20nm and 100nm, the density of the planar defects increases (Fig4.3 and Fig.6.1b). Both planar defects and 60° perfect dislocations were observed in 200nm and 500nm thick films (Fig.6.1c and d). The nature of the planar defects was further studied by HRTEM. Figure 6.2a shows a HRTEM image of the planar defects in a 20nm thick film. Inset is the fast Fourier transform (FFT) image of the area indicated by the box. The inverse fast Fourier transform (IFFT) image formed using {111} and {200} reflections from the FFT is shown in Fig.6.2b. The IFFT image of Fig.6.2c is an enlargement of the area of the tip from the planar defect. According to the right-hand/start-finish convention, a Burgers circuit constructed around the tip of the

Figure 6.1

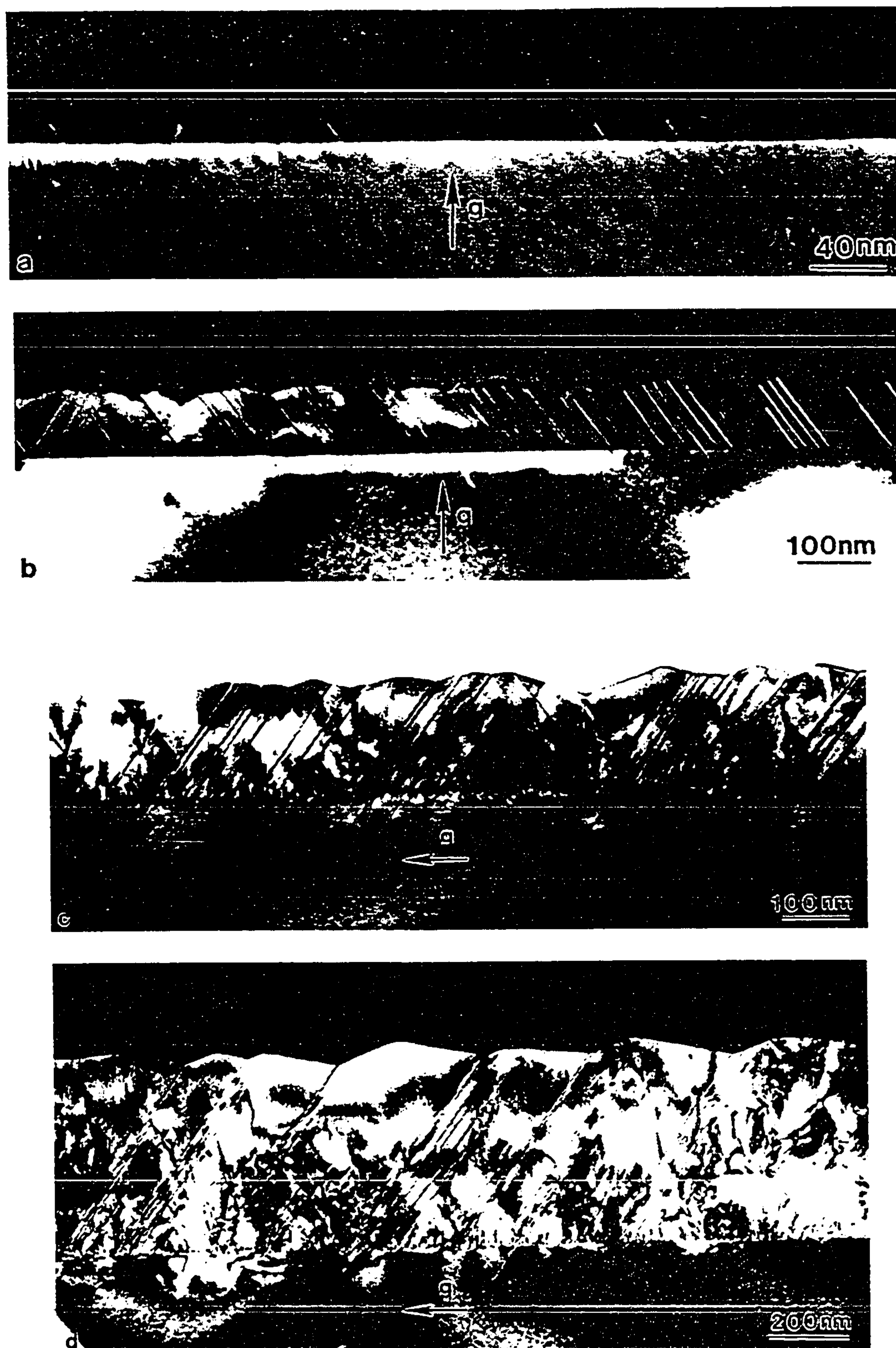

The change of the structure with the change in film thickness in $[0\bar{1}1]$ cross-section: (a) h = 10nm, g = 200; (b) h = 100nm, g = 200; (c) h = 200nm, g = 022; (d) h = 500nm, g = 022.

planar defect is also shown in Fig.6.2c. The Burgers vector is determined to be (a/6)$[2\bar{1}\bar{1}]$. Since (a/6)$[2\bar{1}\bar{1}]$ is perpendicular to the dislocation line direction $[0\bar{1}1]$, the (a/6)$[2\bar{1}\bar{1}]$ dislocation is a 90° Shockley partial dislocation, bounded by a stacking fault lying on the (111) plane. This observation also confirms that the 90° Shockley partial dislocation is the leading partial dislocation in a tensile strained film, as noted in Chapter 2. The extended dislocation is formed according to the following reaction in (111) plane:

$$\frac{a}{2}[10\bar{1}] \rightarrow \frac{a}{6}[2\bar{1}\bar{1}] + \text{S.F.} + \frac{a}{6}[11\bar{2}] \qquad (6.1.1)$$

where (a/2)$[10\bar{1}]$ is a 60° perfect dislocation, (a/6)$[2\bar{1}\bar{1}]$ is a 90° leading partial dislocation, (a/6)$[11\bar{2}]$ is a 30° trailing partial dislocation, (note that the line direction of both perfect and partial dislocations is $[0\bar{1}1]$), and S.F. is an intrinsic stacking fault.

Most planar defects in this sample were identified as stacking faults. A few of the planar defects are ultra-thin microtwins having a thickness of 2 to 3 {111} planes. The planar defect labeled 1 in Fig.6.2a has different characteristics between part A and part B. Part A is a ultra-thin microtwin with a thickness of two (111) planes, while part B is a single stacking fault. The planar defect labeled 2 in Fig.6.2a is a microtwin having a thickness of three (111) planes. Figure 6.2d illustrates the geometry of the planar defects 1 and 2 in Fig.6.2a.

The average 90° partial dislocation spacing in $[0\bar{1}1]$ cross-section for film thicknesses h = 10nm, 20nm, and 100nm was obtained from TEM images such as Fig.6.1a,b and Fig.4.3; at least 30 measurements were made on each film. The data is summarized in Table 6.1.

Figure 6.2

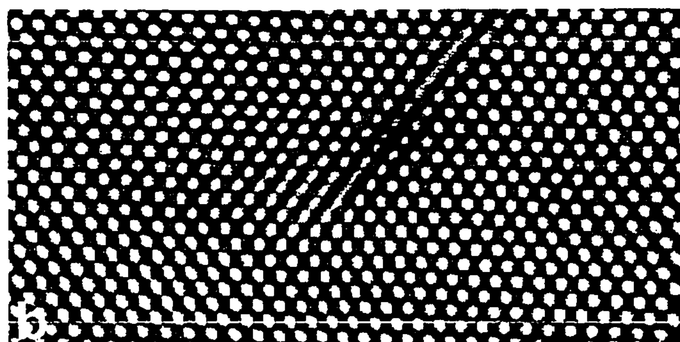

Figure 6.2 (continued)

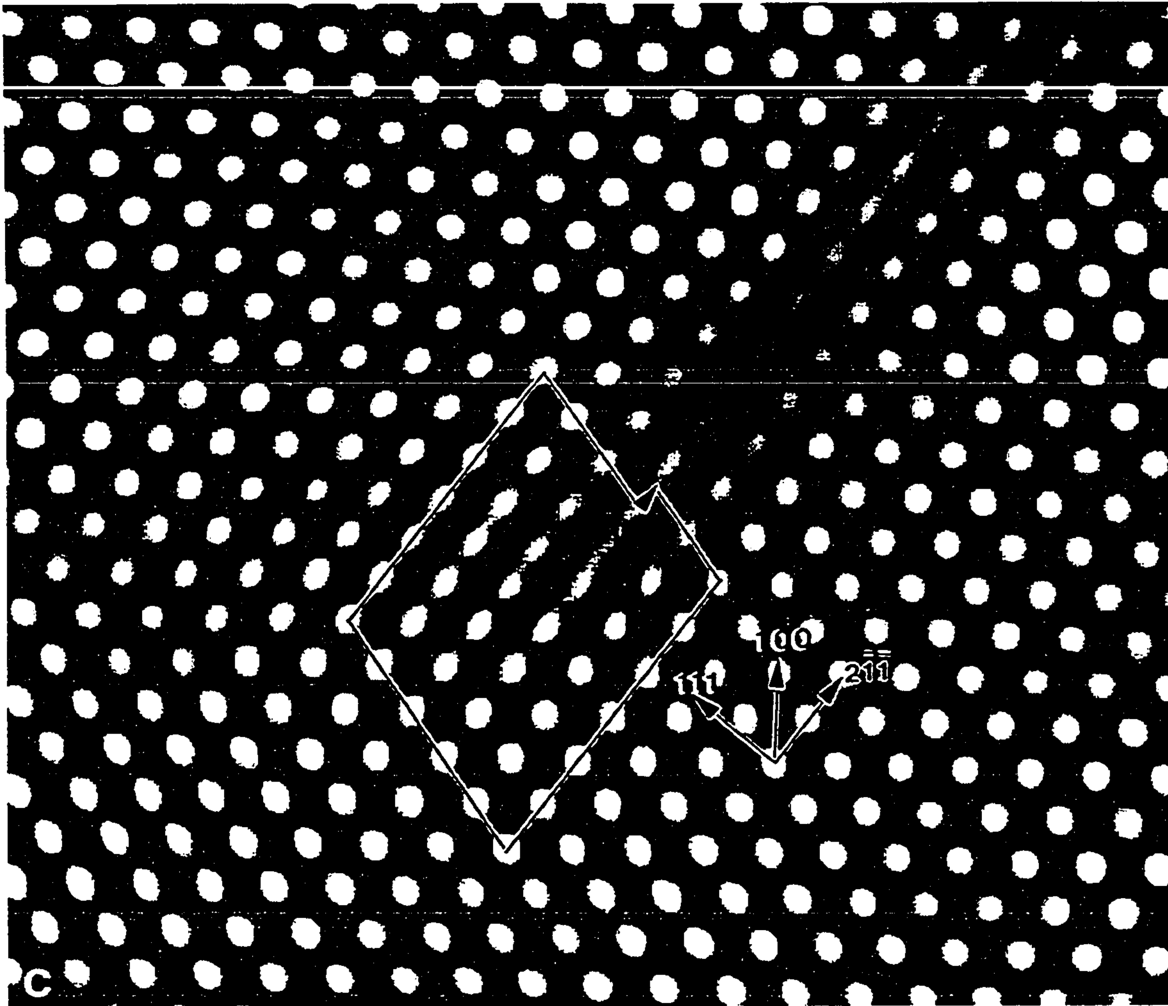

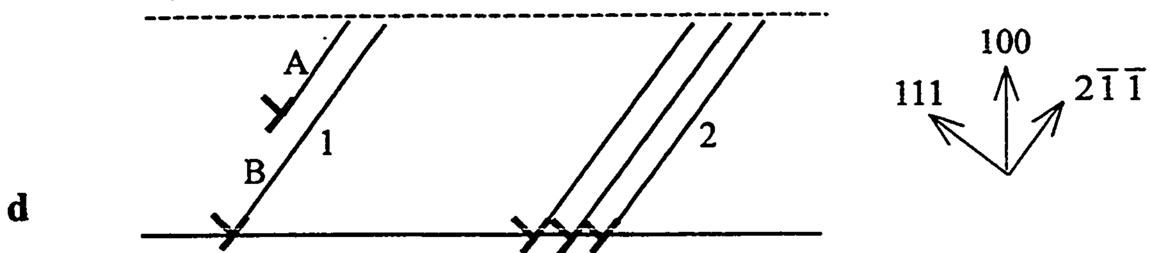

HRTEM image of planar defects in $[0\bar{1}1]$ cross-section. (a) HRTEM image, together with the inset FFT image of the area indicated by the box; (b) IFFT image formed using {111} and {200} reflections in FFT image in (a); (c) Enlargement of the area of the tip of planar defect 1. A (a/6)$[2\bar{1}\bar{1}]$ partial dislocation is identified by the Burgers circuit. (d) Geometry of the planar defects 1 and 2 in (a).

Figure 6.3

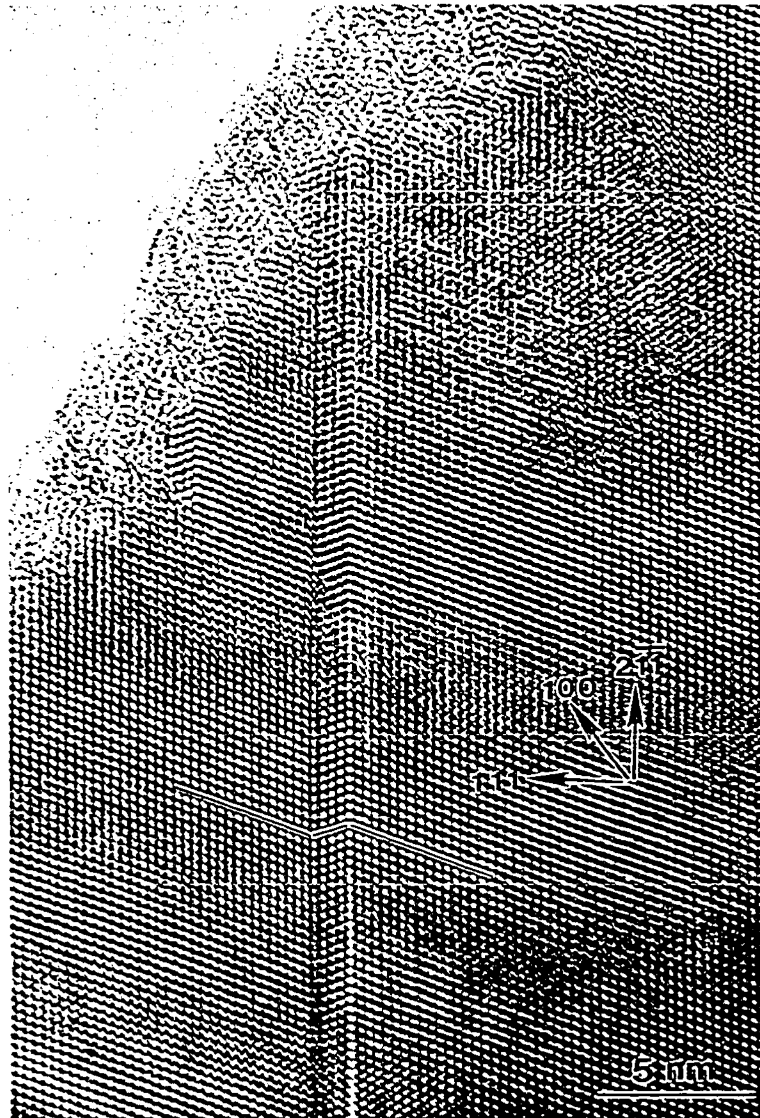

HRTEM image of a twin in 200nm thick film. The twin thickness is five (111) planes.

Table 6.1 Summary of measurement of 90° partial dislocation spacing with different film thickness

Film thickness (nm)	Average spacing (nm)
10	100
20	25
100	20

The thickness of the twins was found to increase with an increase in film thickness. Figure 6.3 is a HRTEM image of a planar defect in the 200nm thick film. This microtwin has a thickness of five (111) planes. Another feature to be noted in the $[0\bar{1}1]$ cross-section samples is the surface morphological instability. The surface of the 20nm film is undulated, as clearly seen in the HRTEM image (Fig.6.2a). Faceted surfaces are observed in 100nm, 200nm and 500nm thick films (Fig.6.1b,c,d). The average facet size increases with an increase in film thickness.

TEM images of [011] cross-sections (see Fig.4.1 and Fig.4.5 in Chapter 4) show very different structures from that seen in $[0\bar{1}1]$ cross-sections. There are no planar defects in the 10nm film (Fig.4.5a), while cracks were observed in the 20 nm film (Fig.4.1). The origin of the cracking phenomena has been discussed in Chapter 4. In the reminder of this chapter, these observations are analyzed in terms of different energy related criteria for defect formation.

6.2 Critical thickness for the formation of 60° perfect dislocation, 90° partial dislocation and crack

When a defect (dislocation or crack) is formed in a strained film, the change in elastic energy of the system is given by

$$\Delta E = E_e + E_{def} \quad (6.2.1)$$

where E_e is the elastic energy relieved by the defect, and E_{def} is the energy associated with the defect.

If $\Delta E < 0$, then the formation of the defect is energetically favored. The critical thickness for the formation of the defect can thus be obtained by solving

$$\Delta E = 0 \quad (6.2.2)$$

For the formation of a crack, E_{def} is the energy associated with the newly formed crack surfaces. The critical thickness for the formation of a crack was obtained in Chapter 4 as

$$h_c = \frac{2\gamma(1-\nu)^2}{3.96(1+\nu)\mu f^2} \quad (6.2.3)$$

As discussed in Chapter 2, for the introduction of either a 60° perfect dislocation or a 90° partial dislocation, the elastic energy per unit length relieved by the dislocation is given by

$$E_e = E_{int,disl/film} = -\frac{2\mu(1+\nu)|f|hb\sin\beta\cos\varphi}{(1-\nu)} \quad (6.2.4)$$

while the elastic energy per unit length associated with the dislocation is given by

$$E_{def} = E_{disl} =$$

$$\frac{\mu b^2(1-\nu\cos^2\beta)}{4\pi(1-\nu)}\ln\left(\frac{2h}{r_0}\right) + \frac{\mu b^2\sin^2\beta}{8\pi(1-\nu)}\left[\cos^2\varphi - \sin^2\varphi - \frac{(1-2\nu)}{2(1-\nu)}\right] + U_{core}$$

(6.2.5)

for a 60° perfect dislocation, and

$$E_{def} = E_{disl} + E_{S.F} =$$

$$\frac{\mu b^2(1-\nu\cos^2\beta)}{4\pi(1-\nu)}\ln\left(\frac{2h}{r_0}\right)+\frac{\mu b^2\sin^2\beta}{8\pi(1-\nu)}\left[\cos^2\varphi-\sin^2\varphi-\frac{(1-2\nu)}{2(1-\nu)}\right]+U_{core}+\frac{\gamma_{S.F}h}{\sin\varphi} \qquad (6.2.6)$$

for a 90° partial dislocation. All parameters in equations (6.2.3), (6.2.4), (6.2.5) and (6.2.6) are defined in Chapters 2 and 4. β = 60° and 90° for perfect and partial dislocations respectively, and $\varphi = \cos^{-1}(1/\sqrt{3})$ for both dislocations.

Combining (6.2.1), (6.2.2), (6.2.4), (6.2.5) and (6.2.6) leads to two equations defining the critical thickness for the formation of dislocations as follows

$$\frac{b}{16\pi}\left[(4-\nu)\ln\left(\frac{2h_c}{r_0}\right)-\frac{1}{2}+\frac{29+6\nu}{4(1-\nu)}\right]=(1+\nu)fh_c \qquad (6.2.7)$$

for a 60° perfect dislocation, and

$$\frac{\mu b^2}{4\pi(1-\nu)}\left[\ln\left(\frac{2h_c}{r_0}\right)-\frac{1}{6}+\frac{7\div 2\nu}{4(1-\nu)}\right]+\frac{\sqrt{3}\gamma_{S.F.}h_c}{\sqrt{2}}=\frac{2\mu(1+\nu)fh_c b}{\sqrt{3}(1-\nu)} \qquad (6.2.8)$$

for a 90° partial dislocation. Cottrell's approximation, $U_{core} = \frac{\mu b^2}{2\pi(1-\nu)^2}$ was used for the dislocation core energy (Cottrell 1953) in all computations using equations (6.2.7) or (6.2.8). The absolute value of U_{core} does not have a serious effect on the calculation.

A plot of critical thickness h_c vs. misfit f for the 60° perfect dislocation, 90° partial dislocation, and crack (equation 6.2.3) in the $In_{0.25}Ga_{0.75}As$ film is shown in Fig.6.4. The data used for this plot are indicated in the figure caption. The value of the stacking fault energy comes from Gottschalk *et al.* (1978). The following conclusions can be drawn from Fig.6.4: cracking is unlikely in lower strained films (misfit f < 2%) because the critical thickness for

the formation of dislocations is much less than that for the formation of crack. As the strain increases, the difference between the critical thicknesses decreases. For a film with misfit $f < 1\%$, a 60° dislocation should be formed first, while a 90° dislocation should be formed first in a film with misfit $f > 1\%$. The prediction of Fig.6.4 agrees with the experimental observations in the 2% tensile strained InGaAs films: 90° partial dislocations bounded by stacking faults are formed prior to the formation of 60° perfect dislocations and cracks. It has been assumed in the above discussion that nucleation of defects is not an issue, i.e. that as soon as the critical thickness is exceeded, the defects will form. This assumption was often made in the study of the critical thickness for the formation of defects. It should also be noted that 90° partial dislocations were first formed in $[0\bar{1}1]$ cross-section of 10 nm thick film, while cracks were first formed in [011] cross-section of 20 nm thick film. The calculations only explain the observations for one of the two orthogonal <011> cross-sections.

6.3 Nucleation of 60° perfect dislocation and 90° partial dislocation

As discussed in Chapter 2, the change in energy on the introduction of a dislocation half-loop of radius r in a strained layer is given by

$$E_{hl} = E_l \pm E_s \pm E_\gamma - E_\tau = \left[\frac{\mu b^2 r(1-\nu/2)}{4(1-\nu)}\right]\ln\left(\frac{\alpha r}{b}\right) \pm 2rb\gamma\sin\theta \pm \frac{1}{2}\pi r^2 \gamma_{S.F.} - \frac{1}{2}\pi r^2 \tau b$$

(6.3.1)

Equation (6.3.1) assumes that τ is constant over the area of the loop. A more general expression for the elastic energy released by the half-loop is given by

Figure 6.4

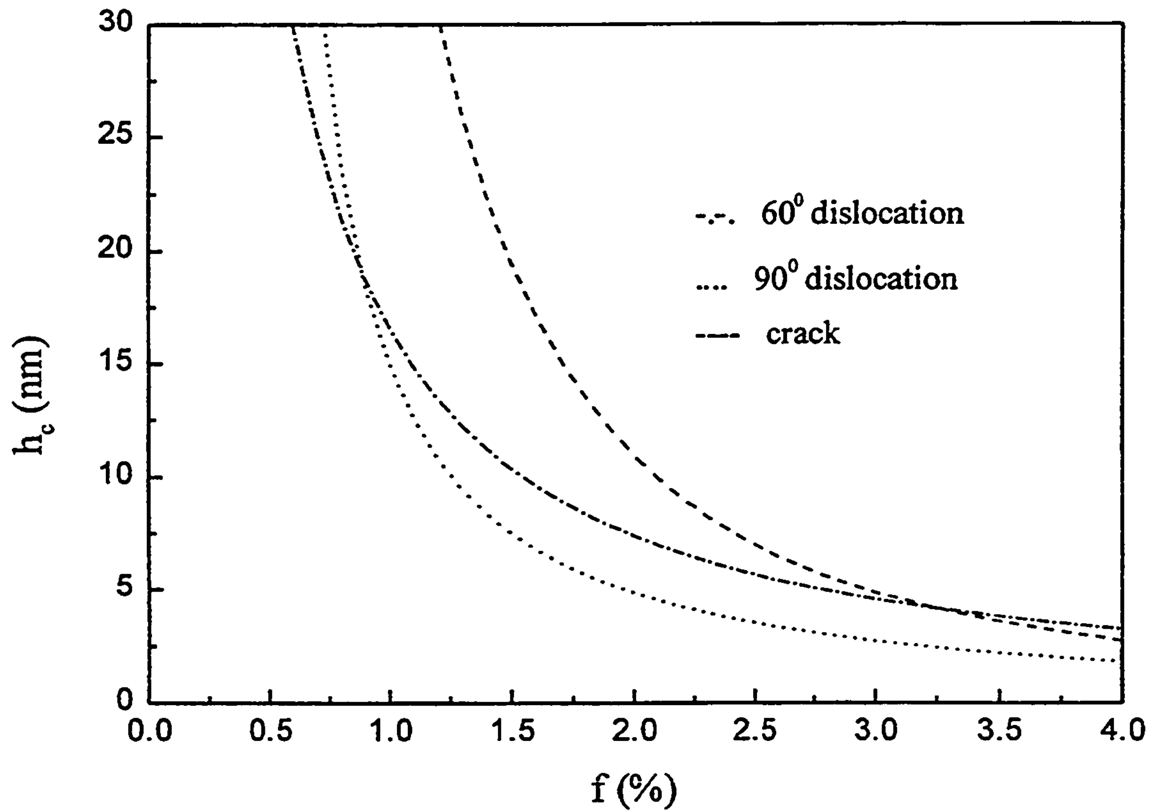

Critical thickness h_c vs. misfit f for a 60° perfect dislocation, a 90° partial dislocation and a crack (equations 6.2.3, 6.2.7 and 6.2.8). Data used for plots: μ = 29.1GPa, ν = 0.322, $\gamma_{S.F.}$ = 48.75 mJ/m^2, 2γ = 1.45J/m^2, b = 4.0691Å for 60° dislocation, b = 2.3493Å for 90° and 30° dislocations and r_0 = b.

$$E_\tau = \int_0^r \tau b \cdot \pi y dy \qquad (6.3.2)$$

where y is the coordinate taken along the film growth direction. The resolved shear stress on the slip plane along the slip direction is related to σ_{xx} by the Schmid factor ($\cos\varphi\cos\lambda$) as $\tau = \sigma_{xx}\cos\varphi\cos\lambda$. φ is the angle between σ_{xx} and the slip plane normal (i.e. the angle between the slip plane and the free surface) and λ is the angle between σ_{xx} and the slip direction.

For a flat surface, the homogeneous biaxial stress $\sigma_{xx} = 2\mu\frac{1+\nu}{1-\nu}f$. Therefore,

$$E_\tau = \int \tau b \cdot \pi y dy = \mu\frac{1+\nu}{1-\nu} fb\pi r^2 \cos\varphi\cos\lambda \qquad (6.3.3)$$

Figure 6.5a and b are plots of E_{hl} vs. r in a 2% tensile strained $In_{0.25}Ga_{0.75}As$ film (assuming the top surface of the film is flat) for two cases: (a) 60° perfect dislocation, 90° leading partial dislocation and 30° trailing partial dislocation, which corresponds to a tensile strained film; (b) 60° perfect dislocation, 30° leading partial dislocation and 90° trailing partial dislocation, which corresponds to a compressively strained film. All data used for the plots are indicated in the figure caption. The values of the Schmid factor for 60° perfect, 90° partial and 30° partial dislocations are calculated in Table 6.2. In these calculations, E_γ is positive for a leading partial since a stacking fault is created while E_γ is negative for the trailing partial since the stacking fault is annihilated; $E_\gamma = 0$ for a perfect dislocation. It is also assumed that E_s is negative when 60° perfect or leading partial dislocations are nucleated since surface steps always exist in the free surface of heterostructures. Dislocation loops will nucleate preferentially at these steps (Zou and Cockayne 1996).

Figure 6.5 shows that E_{hl} initially increases with increasing r, reaches a maximum value of E_{hlc} (the activation energy for nucleation) at a critical radius r_c, and then decreases as r increases beyond r_c. For a tensile strained film, E_{hlc} for the 90° leading partial (15.8eV) < E_{hlc} for the 30° trailing partial (36.3eV) < E_{hlc} for the 60° perfect dislocation (79.0eV) (Fig.6.5a). Therefore, the 90° leading partial dislocation half-loops should nucleate first at the growing surface and expand to the interface. The 90° leading partial moves ahead of the 30° trailing partial and creates a stacking fault, which may be removed by the trailing partial. The interface misfit dislocation is a 90° partial dislocation and contributes only $\sqrt{2}a/6$ to the release of strain in the film. Moreover, the 90° leading partial dislocation creates a stacking fault on the {111} glide plane. After the first 90° leading partial dislocation bounded by a stacking fault is formed, a second 90° leading partial dislocation half-loop may be nucleated on neighboring {111} planes and expand to the interface to relax the misfit strain. In this way, as shown in Chapter 2, stacking faults form sequentially on parallel {111} planes and produce a microtwin band. The formation of a microtwin of thickness $m \times d_{111}$ (where m is an integer and d_{111} is the {111} interplanar spacing) requires that m such stacking faults lie next to each other, i.e. m 90° partial dislocation half-loops nucleate on neighboring {111} planes and expand to the interface. The nucleation of 90° partial dislocations on neighboring planes will stop when the resolved shear stress falls bellow the critical value needed for nucleation. The energy analysis of the equilibrium microtwin thickness is presented in section 6.5. HRTEM observations (Figs.6.2 and 6.3) clearly demonstrate this mechanism. This mechanism of formation of stacking faults and microtwins has also been reported in the strained Si-Ge

(Wegscheider *et al.* 1990) and Au-Ni systems (Dynna *et al.* 1997).

For a compressively strained film, the 30° leading partial has to start the nucleation process first. However, the activation energy (E_{hlc}) of the 30° leading partial (65.9eV) is much higher than that of the 90° trailing partial (13.9eV). Therefore, if the 30° leading partial is nucleated, it will be instantly followed by the 90° trailing partial, which means the formation of stacking faults and microtwins is highly unlikely in a compressively strained film. Instead, a 60° perfect dislocation network is expected to relieve the misfit strain in a compressively strained film.

Table 6.2 The values of the Schmid factor

	60° perfect dislocation	90° partial dislocation	30° partial dislocation
Stress (σ_{xx}) direction	011	011	011
Slip plane	111	111	111
Slip direction (**b**)	$10\bar{1}$	$2\bar{1}\bar{1}$	$11\bar{2}$
cosφ	0.816	0.816	0.816
cosλ	0.500	0.577	0.289
Schmid factor (cosφcosλ)	0.408	0.471	0.236

Although we have shown that stacking faults and microtwins will be favored to form through the nucleation of 90° leading partial dislocations in the tensile strained film, the activation energy (E_{hlc} = 15.8eV) shown in Fig.6.5a is too high for a homogeneous nucleation process to occur because the available energy for surface nucleation is 50 kT (3.24 eV at the growth temperature 480°C) (Frank 1950; Matthews *et al.* 1976). As noted in this study and other studies (Eaglesham and Cerollu 1990; Guha *et al.* 1990; Synder *et al.* 1991; Cullis *et al.* 1996), the surface of the film roughens before dislocations form. In other words, dislocations nucleate at an undulated surface, not a perfect flat surface. For an undulated surface, a stress

Figure 6.5

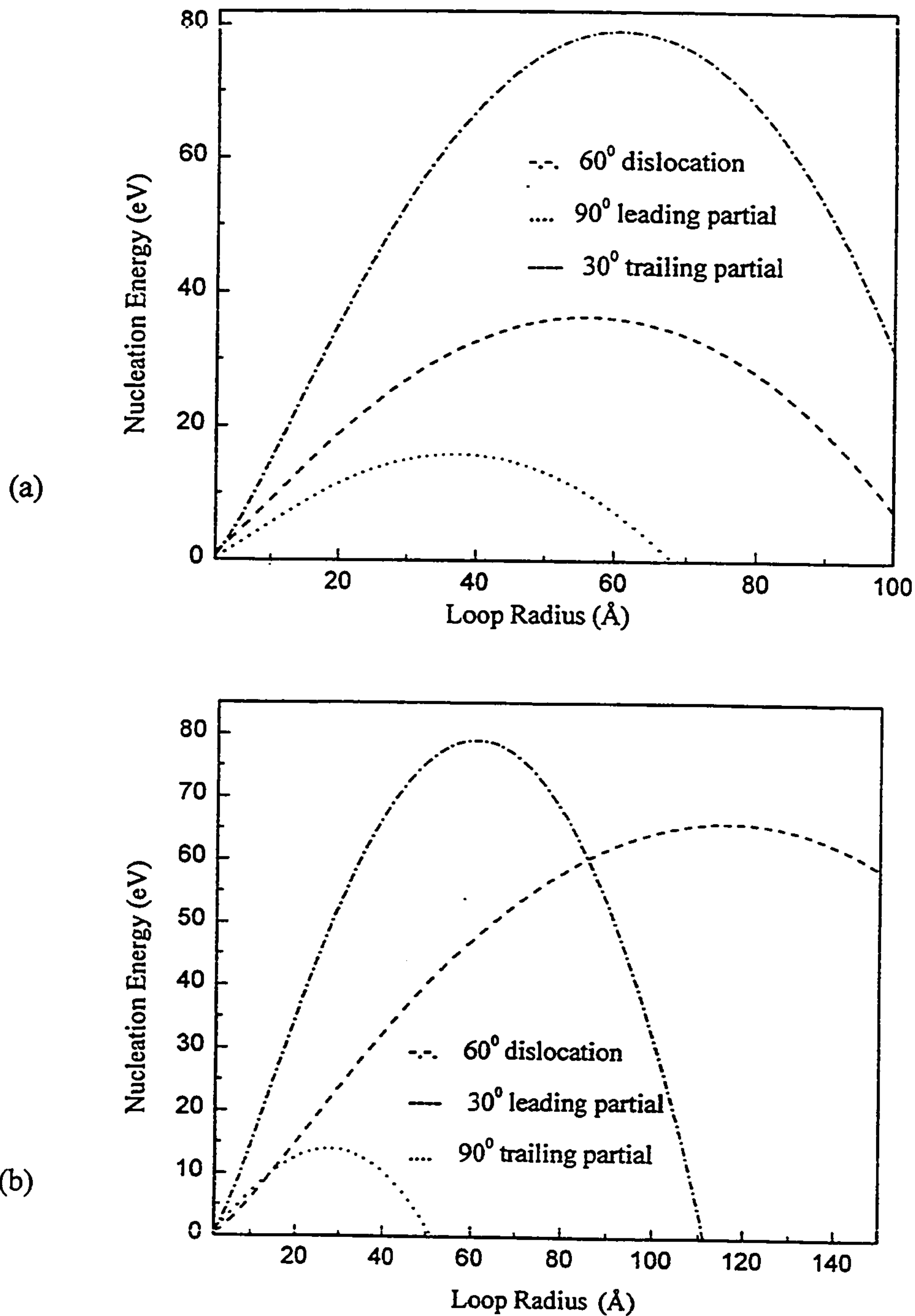

E_{hl} vs. half-loop radius r for the homogeneous nucleation (equations 6.3.1 and 6.3.3) in the tensile strained film (a) and the compressive strained film (b). Data used for plots: $\alpha = 4$, $\mu = 29.1$GPa, $\nu = 0.322$, $\gamma_{S.F.} = 48.75$ mJ/m^2, $2\gamma = 1.45$J/m^2, f = 0.02, b = 4.0691Å for 60° dislocation and b = 2.3493Å for 90° and 30° dislocations.

concentration occurs as discussed in Chapter 2. If the shape of the undulated surface is described by a sine function y = esin(kx), $\sigma_{xx} = 2\mu\frac{1+\nu}{1-\nu}f[1 - ek(ky-2)\exp(-kr)\sin(kx)]$ where k = 2π/λ (see Fig.2.6c and equation 2.3.2 in Chapter 2). The maximum stress concentration factor 1+2ek occurs at sin(kx) = 1 and y = 0. When sin(kx) = 1, $\sigma_{xx} = 2\mu\frac{1+\nu}{1-\nu}f[1 - ek(ky-2)\cdot\exp(-kr)]$, and the E_τ term now becomes

$$E_\tau = \int \tau b \cdot \pi y dy = \mu\frac{1+\nu}{1-\nu} fb\pi r^2 \cos\varphi\cos\lambda[1 + 2ek\cdot\exp(-kr)] \qquad (6.3.4)$$

Figure 6.6a and b are the plots of E_{hl} vs. r for a sinusoidal surface in a 2% tensile strained $In_{0.25}Ga_{0.75}As$ film for two cases: (a) 60° perfect dislocation, 90° leading partial dislocation and 30° trailing partial dislocation, which corresponds to tensile strained film; (b) 60° perfect dislocation, 30° leading partial dislocation and 90° trailing partial dislocation, which corresponds to a compressively strained film. The values defining the sinusoidal surface are chosen to be λ = 20nm and e = 2.5nm (see Fig.2.6c for the definition of λ and e) to conform to the experimental observation shown in Fig.6.2a). All other values used in Fig.6.6 are the same as those used in Fig.6.5. The changes in E_{hl} with an increase in r follow the same trends shown in Fig.6.5, but the activation energy is reduced for all situations because of the increase in the resolved shear stress. The activation energy for the 90° leading partial dislocation nucleation (Fig6.6a) decreases from 15.8eV to 3.4eV. This value is close to the available energy for surface nucleation given by Frank (1950) and Matthews *et al.* (1976) as 50 kT (3.24 eV at growth temperature 480°C).

Figure 6.6

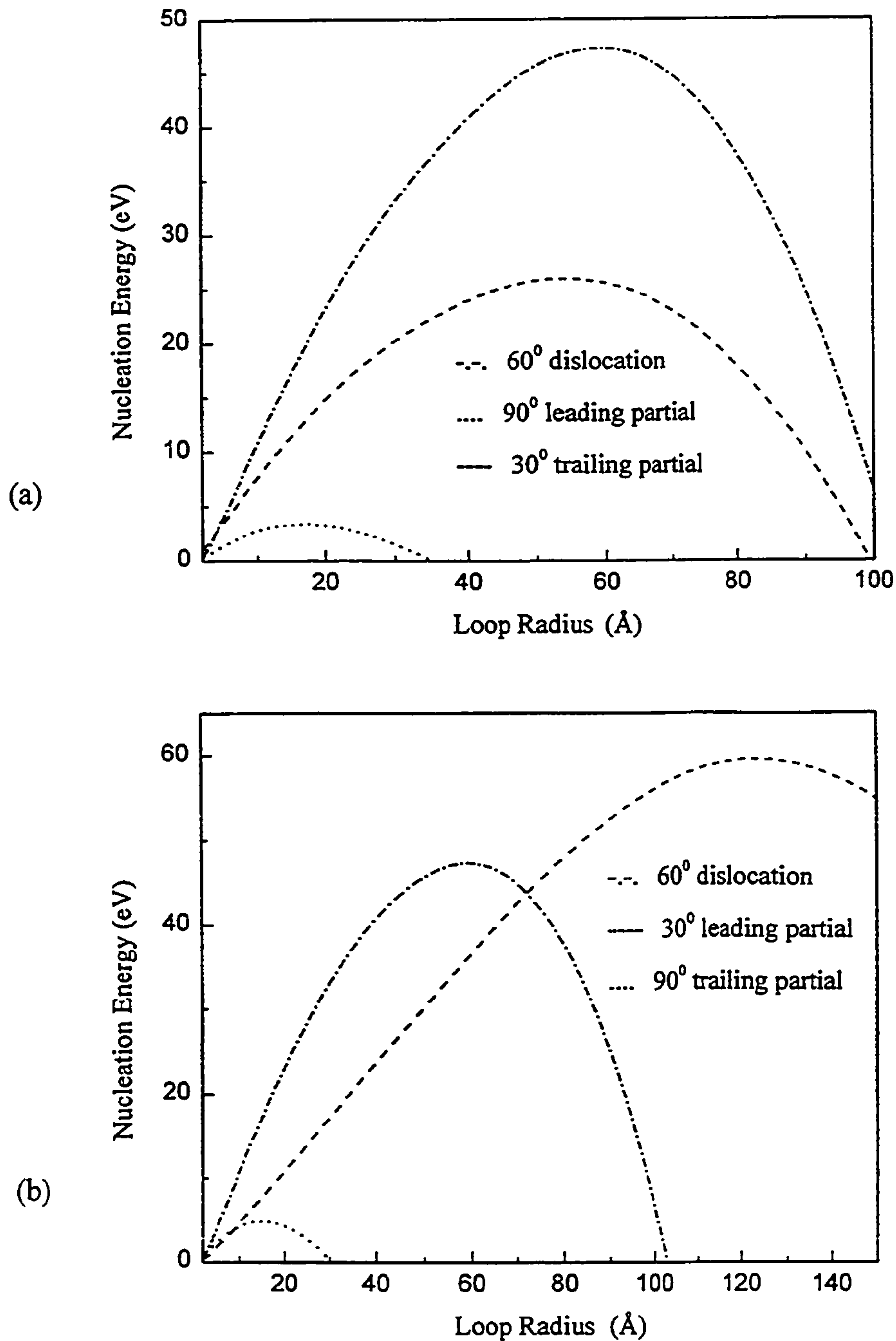

E_{hl} vs. half-loop radius r for heterogeneous nucleation (equations 6.3.1 and 6.3.4) in the tensile strained film (a) and the compressive strained film (b). Data used for plots: $\alpha = 4$, $\mu = 29.1$Gpa, $\nu = 0.322$, $\gamma_{S.F.} = 48.75$ mJ/m^2, $2\gamma = 1.45$J/m^2, f = 0.02, b = 4.0691Å for 60° dislocation, b = 2.3493Å for 90° and 30° dislocations, e = 2.5nm, and λ = 20nm.

6.4 Elastic energy of the film with 60° perfect, 90° partial dislocations and cracks

As discussed in Chapter 2, the total elastic energy of the system with the array of dislocations shown in Fig.2.4 is given by:

$$E_{total} = E_0 + E_{disl} + E_{int,dis/film} + E_{int.dis/dis}$$

$$= 2\mu\frac{1+\nu}{1-\nu}f^2h + \frac{1}{d}\left\{\frac{\mu b^2(1-\nu\cos^2\beta)}{4\pi(1-\nu)}\ln\left(\frac{2h}{r_0}\right) + \frac{\mu b^2\sin^2\beta}{8\pi(1-\nu)}\left[\cos^2\varphi - \sin^2\varphi - \frac{1-2\nu}{2(1-\nu)}\right] + U_{core}\right\}$$

$$-\frac{2\mu(1+\nu)fhbsiin\beta\cos\varphi}{(1-\nu)d} + \frac{\mu b^2(1-\nu\cos^2\beta)}{4\pi(1-\nu)d}\ln\left[\frac{d}{2\pi h}\sinh\left(\frac{2\pi h}{d}\right)\right]$$

$$+\frac{\mu b^2\sin^2\beta\cos^2\varphi}{4\pi(1-\nu)d}\left[\frac{2\pi h}{d}\coth\left(\frac{2\pi h}{d}\right) - \frac{2\pi^2h^2}{d^2}\operatorname{csch}^2\left(\frac{2\pi h}{d}\right) - \frac{1}{2}\right]$$

$$-\frac{\mu b^2\sin^2\beta\sin^2\varphi}{4\pi(1-\nu)d}\left[\frac{2\pi h}{d}\coth\left(\frac{2\pi h}{d}\right) + \frac{2\pi^2h^2}{d^2}\operatorname{csch}^2\left(\frac{2\pi h}{d}\right) - \frac{3}{2}\right] \qquad (6.4.1)$$

for a 60° mixed dislocation array (Fig.2.4a) with $\beta = 60°$ and $\varphi = \cos^{-1}(1/\sqrt{3})$;

and

$$E_{total} = E_0 + E_{disl} + E_{int,dis/film} + E_{int.dis/dis} + E_{S.F.}$$

$$= 2\mu\frac{1+\nu}{1-\nu}f^2h + \frac{1}{d}\left\{\frac{\mu b^2(1-\nu\cos^2\beta)}{4\pi(1-\nu)}\ln\left(\frac{2h}{r_0}\right) + \frac{\mu b^2\sin^2\beta}{8\pi(1-\nu)}\left[\cos^2\varphi - \sin^2\varphi - \frac{1-2\nu}{2(1-\nu)}\right] + U_{core}\right\}$$

$$-\frac{2\mu(1+\nu)fhbsiin\beta\cos\varphi}{(1-\nu)d} + \frac{\mu b^2(1-\nu\cos^2\beta)}{4\pi(1-\nu)d}\ln\left[\frac{d}{2\pi h}\sinh\left(\frac{2\pi h}{d}\right)\right]$$

$$+\frac{\mu b^2\sin^2\beta\cos^2\varphi}{4\pi(1-\nu)d}\left[\frac{2\pi h}{d}\coth\left(\frac{2\pi h}{d}\right) - \frac{2\pi^2h^2}{d^2}\operatorname{csch}^2\left(\frac{2\pi h}{d}\right) - \frac{1}{2}\right]$$

$$-\frac{\mu b^2\sin^2\beta\sin^2\varphi}{4\pi(1-\nu)d}\left[\frac{2\pi h}{d}\coth\left(\frac{2\pi h}{d}\right) + \frac{2\pi^2h^2}{d^2}\operatorname{csch}^2\left(\frac{2\pi h}{d}\right) - \frac{3}{2}\right] + \frac{\gamma_{S.F.}h}{d\sin\varphi} \qquad (6.4.2)$$

for a 90° partial dislocation array + stacking faults (Fig.2.4b) with $\beta = 90°$ and $\varphi = \cos^{-1}\left(1/\sqrt{3}\right)$.

Figure 6.7a shows (E_{total}/E_0) vs. the dislocation spacing d at film thickness h = 100nm for both 60° perfect and 90° partial dislocations in the 2% (f = 0.02) $In_{0.25}Ga_{0.75}As$ film. $E_0 = 2\mu\frac{1+\nu}{1-\nu}f^2h$ is the elastic energy per unit area of the system without defects. All data used for the plots are listed in the figure caption. It can be seen from Fig.6.7a that there is an equilibrium dislocation spacing (d_{eq}) that gives a minimum energy $(E_{total}/E_0)_{min}$. At a given film thickness h, the value of d_{eq} can be obtained by finding the minimum in the total elastic energy of the system, i.e. solving the equation $\partial(E_{total}/E_0)/\partial d = 0$. The plots of equilibrium dislocation spacing d_{eq} vs. film thickness h for both 60° perfect and 90° partial dislocations in the 2% (f = 0.02) $In_{0.25}Ga_{0.75}As$ film are shown in Fig.6.7b. It can be seen that d_{eq} decreases with an increase in the film thickness over a small film thickness range, and quickly reaches a near constant value when the film thickness increases to the large value. Moreover, the 60° perfect dislocation array is more widely spaced than the 90° partial dislocation array. This is primarily due to the nature of the screw components in the 60° perfect dislocation array – as a whole they have a long-range stress field and a repulsive interaction with each other while there is no screw component in the 90° partial dislocation array. The observed 90° partial dislocation spacing in $[0\bar{1}1]$ cross-section of the 20nm and 100nm thick films is included in Fig.6.7b for comparison. The observed dislocation spacing is found to be much larger than the equilibrium spacing (d_{eq}) predicted by equation (6.4.2), i.e. the density of dislocations has not yet reached the equilibrium status. The energy barrier of dislocation nucleation process

Figure 6.7

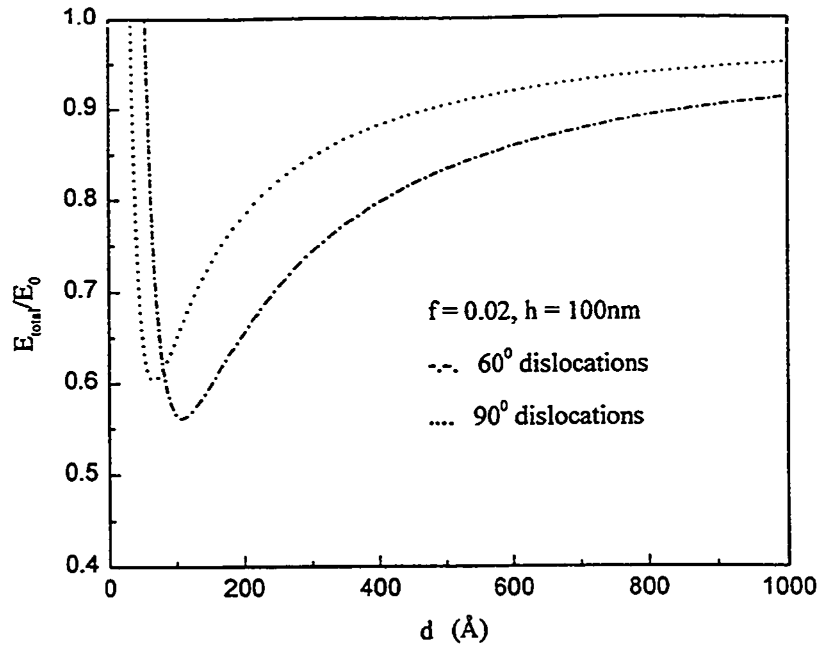

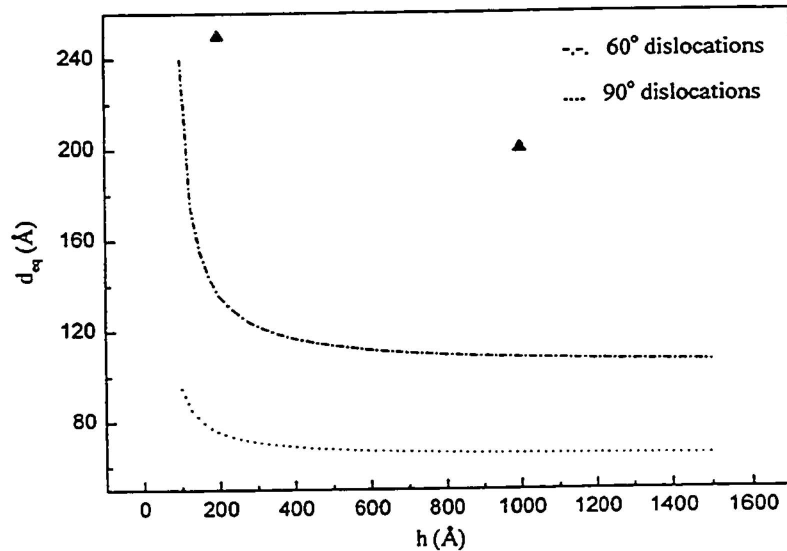

The calculation of the total elastic energy of the system with 60° perfect dislocation and 90° partial dislocation arrays (a) E_{total}/E_0 vs. d for h = 100nm and f = 0.02; (b) d_{eq} vs. h. Solid triangles in (b) are the observed 90° dislocation spacing. Data used for plots: μ = 29.1GPa, ν = 0.322, $\gamma_{S.F.}$ = 48.75 mJ/m^2, f = 0.02, b = 4.0691Å for 60° dislocation and b = 2.3493Å for 90° and 30° dislocations, and r_0 = b.

prevents dislocation from reaching equilibrium because part of the strain was relieved by previously formed dislocations, which increases the E_{hlc}. Strain relaxation by cracking and surface roughening may also contribute to the observed dislocation spacing, i.e. dislocations only account for part of the stress relaxation.

The minimum total elastic energy of the system $(E_{total}/E_0)_{min}$ vs. the film thickness h for both 60° perfect and 90° partial dislocations in the 2% (f = 0.02) $In_{0.25}Ga_{0.75}As$ film are shown in Fig.6.8. Also included in Fig.6.8 is the minimum total elastic energy of the system $(E_{total}/E_0)_{min}$ vs. the film thickness h for cracks, obtained from the following analysis. A complete discussion of this figure is presented later in this sub-section.

As discussed in Chapter 2, for the crack array shown in Fig.2.2c, with cracks confined in the film, the stress intensity factor K is given as a function of s, where s = 2c/(2c+d) by (Bowie 1973):

$$K = Q(s)\sqrt{1-s}\,\sigma\sqrt{\pi c} \tag{6.4.3}$$

with

$$Q(s) = \frac{1}{\sqrt{\pi}}\left[1+\frac{1}{2}(1-s)+\frac{3}{8}(1-s)^2+\frac{5}{16}(1-s)^3+\frac{25}{128}(1-s)^4+\frac{63}{256}(1-s)^5+\frac{231}{1024}(1-s)^6\right]$$
$$+22.501(1-s)^7-63.502(1-s)^8+58.045(1-s)^9-17.577(1-s)^{10} \tag{6.4.4}$$

The plot of K vs. s is shown in Fig.6.9. Equation (6.4.3) is rather complicated, but it can be approximately expressed using the two simpler equations:

Figure 6.8

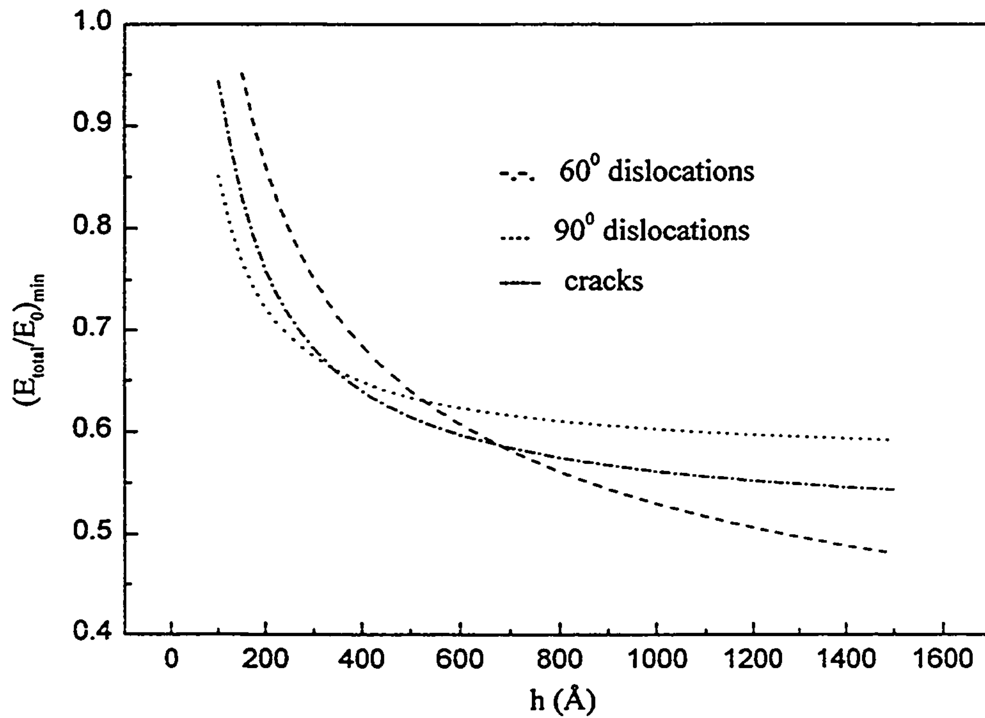

$(E_{total}/E_0)_{min}$ vs. h for 60° perfect dislocations, 90° partial dislocations + stacking faults and cracks. Data used for plots: μ = 29.1GPa, ν = 0.322, $\gamma_{S.F.}$ = 48.75 mJ/m^2, 2γ = 1.45J/m^2, b = 4.0691Å for 60° dislocation, b = 2.3493Å for 90° and 30° dislocations, and $r_0 = b$.

$$K_1 = \left(1.122 + 0.015s - 2.92s^2\right)\sigma\sqrt{\pi c} = \left[1.122 + 0.015\frac{2c}{2c+d} - 2.92\frac{(2c)^2}{(2c+d)^2}\right]\sigma\sqrt{\pi c},$$

$$0 \le s \le 0.286, \text{ i.e. } d \ge 5c \qquad (6.4.5a)$$

$$K_2 = \sqrt{\frac{1-s}{\pi s}}\sigma\sqrt{\pi c} = \sqrt{\frac{d}{2\pi c}}\sigma\sqrt{\pi c}, \qquad 0.286 \le s \le 1, \text{ i.e. } d \le 5c \qquad (6.4.5b)$$

when $d = 5c$, $K_1 = K_2 = 0.89\sigma\sqrt{\pi c}$. This approximation is shown in Fig.6.9.

The total elastic energy of the system with an array of cracks shown in Fig.2.2c is given by:

$$E_{total} = E_0 + E_e + E_s \qquad (6.4.6)$$

where $E_0 = 2\mu\frac{1+\nu}{1-\nu}f^2h$ is again the elastic energy per unit area of the system without defects, $E_s = \frac{2\gamma h}{d}$ is the increased energy per unit area due to newly formed crack surfaces. The elastic energy per unit area relieved by cracks can be computed using equation (2.1.9) as follows:

when $d \ge 5h$,

$$E_{e1} = -\frac{1}{d}\int_0^h \frac{K_1^{\,2}}{E}dc$$

$$= -\frac{\sigma^2\pi}{Ed}\left[0.73d^2 - 2.18625d^2\ln\left(\frac{d+2h}{d}\right) + \frac{4.9335h^2d + 2.9125hd^2}{2h+d} - \frac{1.783h^3 + 0.73d^3}{2h+d}\right]$$

(6.4.7a)

when $d \le 5h$

Figure 6.9

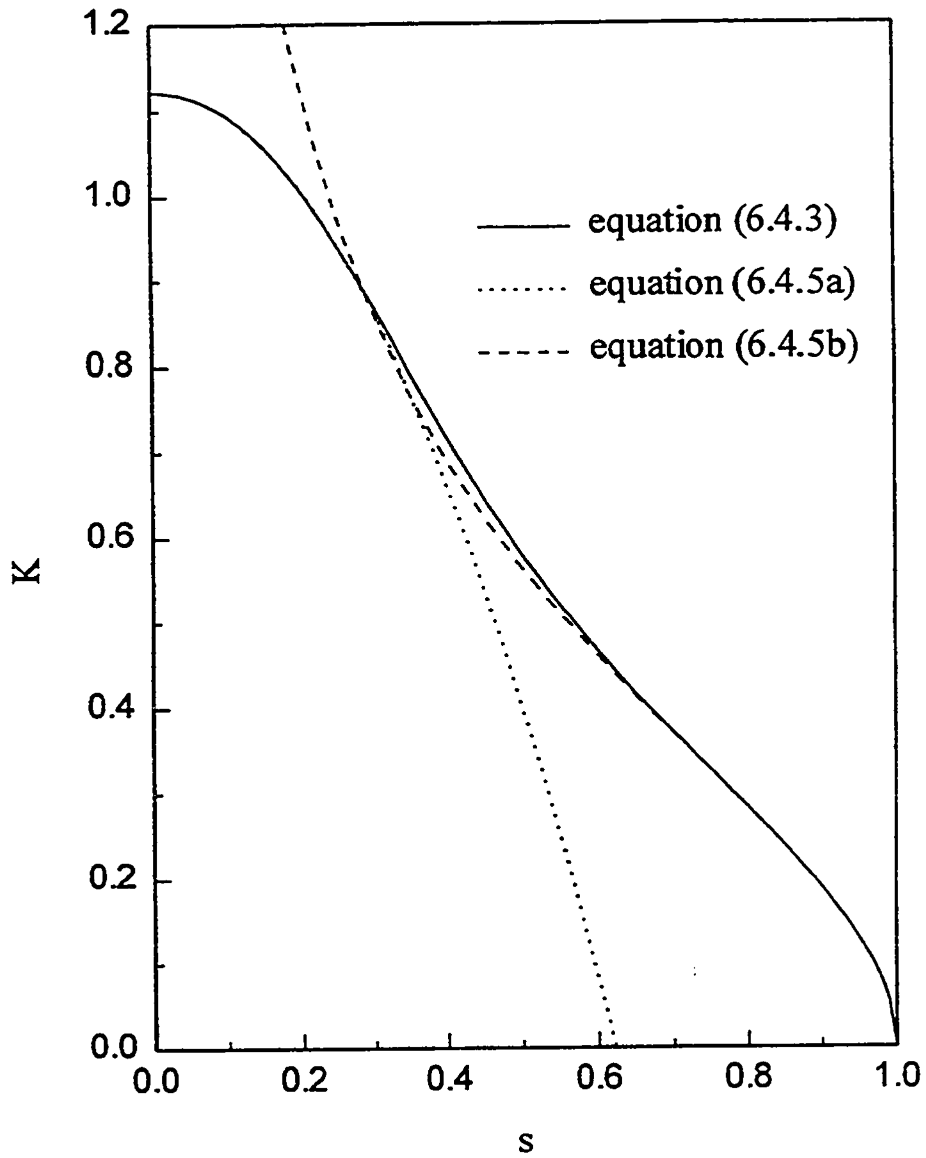

The stress intensity factor K as a function of s (solid line) for the crack array shown in Fig.2.2c, and two approximate expressions (dot line and dash line) (see text).

$$E_{e2} = -\frac{1}{d}\int_0^{d/5}\frac{K_1^2}{E}dc - \frac{1}{d}\int_{d/5}^{h}\frac{K_2^2}{E}dc = -\frac{\sigma^2}{Ed}\left(\frac{d}{2}h - 0.0378d^2\right) \quad (6.4.7b)$$

At $d = 5h$, $E_{e1} = E_{e2} = -1.555(\sigma^2/E)$

Therefore, the total elastic energy per unit area of the system with cracks terminated at the interface may be written as:

$$E_{total} = 2\mu\frac{1+\nu}{1-\nu}f^2h + \frac{2\gamma h}{d}$$

$$-\frac{\sigma^2\pi}{Ed}\left[0.73d^2 - 2.18625d^2\ln\left(\frac{d+2h}{d}\right) + \frac{4.9335h^2d + 2.9125hd^2}{2h+d} - \frac{1.783h^3 + 0.73d^3}{2h+d}\right]$$

$$(d \geq 5h) \quad (6.4.8a)$$

and

$$E_{total} = 2\mu\frac{1+\nu}{1-\nu}f^2h - \frac{\sigma^2}{Ed}\left(\frac{d}{2}h - 0.0378d^2\right) + \frac{2\gamma h}{d} \quad (d \leq 5h) \quad (6.4.8b)$$

with $\sigma = 2\mu\frac{1+\nu}{1-\nu}f$ and $E = 2\mu(1+\nu)$.

Figure 6.10a shows (E_{total}/E_0) vs. the crack spacing d in the 100nm thick, 2% ($f = 0.02$) tensile strained $In_{0.25}Ga_{0.75}As$ film using (6.4.8b). All data used for the plots are listed in the figure caption. Again there is an equilibrium crack spacing (d_{eq}) that gives a minimum energy $(E_{total}/E_0)_{min}$. At a given film thickness h, the value of d_{eq} can be obtained by finding the minimum in the total elastic energy of the system, i.e. solving the equation $\partial(E_{total}/E_0)/\partial d = 0$. Figure 6.10a shows that $d_{eq}/h \approx 2 < 5$ at $h = 100$nm, which is true for all films with thickness larger than 20nm. Therefore, equation (6.4.8b) is used to discuss the equilibrium crack spacing d_{eq} and the minimum total elastic energy $(E_{total}/E_0)_{min}$. Solving $\partial(E_{total}/E_0)/\partial d = 0$ for

equation (6.4.8b) gives

$$d_{eq} = \sqrt{\frac{(1-\nu)^2 \gamma h}{0.0378(1+\nu)\mu f^2}} \tag{6.4.9}$$

This equation is similar to equation (2.1.26) given by Thouless *et al.* (1992). The plot of the equilibrium crack spacing d_{eq} vs. film thickness h of equation (6.4.9) for the 2% (f = 0.02) $In_{0.25}Ga_{0.75}As$ film is shown in Fig.6.10b. Also included in Fig.6.10b are the experimental data of crack spacing for films of thickness h = 20nm, 100nm and 200nm from Table 4.1 in Chapter 4. It can be seen from Fig.6.10b that the observed crack spacing is greater than the equilibrium spacing (d_{eq}) predicted by equation (6.4.9), and the difference between d_{eq} and observed crack spacing increases with the increase in film thickness. Several reasons account for this phenomenon. Firstly, crack nucleation is probably a heterogeneous process, and the system runs out of sites for nucleation as the stress partially drops in a cracked film. Secondly, part of the misfit strain was relieved by plastic-flow and surface roughening before cracks are formed, and this effect increases with the increase in film thickness. Thirdly, some cracks are healed in thicker films as discussed in Chapter 4.

The minimum total elastic energy of the system $(E_{total}/E_0)_{min}$ vs. the film thickness h for cracks in a 2% (f = 0.02) tensile strained $In_{0.25}Ga_{0.75}As$ film is shown in Fig.6.8. In addition to being readily nucleated as discussed in section 6.3, 90° partial dislocations also provide the most effective relief of elastic strain energy, at least for small film thicknesses (h < 350Å), as can be seen from Fig.6.8. Cracking becomes the most effective strain relaxation mechanism at thicker films (h > 700Å). The most effective strain relief mechanism for intermediate film thickness between 350Å and 700Å is 60° perfect dislocation. However throughout the whole

Figure 6.10

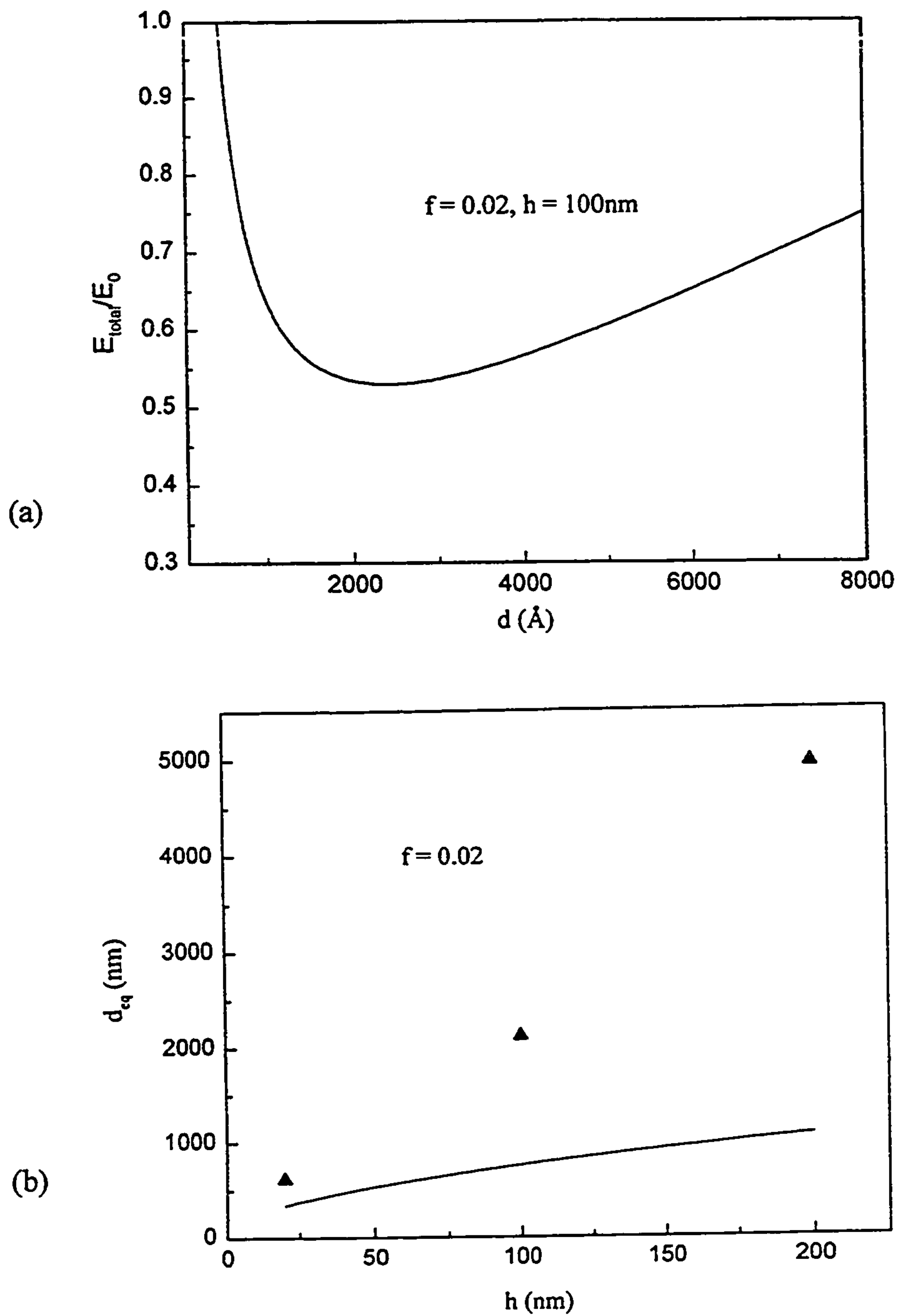

The calculation of the total elastic energy of the system with a crack array. (a) E_{total}/E_0 vs. d calculated using equations (6.4.8b); (b) d_{eq} vs. h computed using equation (6.4.8b). Solid triangles in (b) are the observed crack spacing. Data used for plots: $\mu = 29.1$GPa, $\nu = 0.322$, $2\gamma = 1.45$J/m^2, f = 0.02.

thickness range shown in Fig.6.8, there are not significant differences between the energy of the system for the three stress relief mechanisms.

6.5 Strain relaxation via twinning

As shown in Figs.6.2 and 6.3, twins act to relieve misfit strain and the twin thickness increases with the increase in film thickness. The twin shown in Fig.6.3 arises as a result of the successive glide of 90° (a/6)<211> partial dislocations on {111} planes. An approximate calculation of their energy may be conducted in a manner similar to that of the energy of an array of perfect dislocation (Dynna *et al.* 1997), as discussed in Chapter 2. The total elastic energy per unit area of the twinning system shown in Fig.2.4c is given by (Dynna *et al.* 1997):

$$E_{total} = E_0 + E_{twin} + E_{int,twin/film} + E_{int,twin/twin}$$

$$= 2\mu\frac{1+\nu}{1-\nu}f^2h + \frac{1}{d}\left\{\frac{m\mu b^2(1-\nu\cos^2\beta)}{4\pi(1-\nu)}\ln\left(\frac{2h}{r_0}\right) + \frac{m\mu b^2\sin^2\beta}{8\pi(1-\nu)}\left[\cos^2\varphi - \sin^2\varphi - \frac{1-2\nu}{2(1-\nu)}\right] + mU_{core} + \frac{2\gamma_T h}{\sin\varphi}\right\}$$

$$+\frac{1}{d}\left\{\frac{\mu b^2}{4\pi(1-\nu)}\sum_{k=1}^{m}(m-k)\left[(1-\nu\cos^2\beta)\ln\left(1+\frac{4h^2}{k^2d_p^2}\right) + \sin^2\beta\sin^2\varphi\frac{12k^2d_p^2h^2+16h^4}{(k^2d_p^2+4h^2)^2} - \sin^2\beta\sin^2\varphi\frac{4k^2d_p^2h^2+48h^4}{(k^2d_p^2+4h^2)^2}\right]\right\}$$

$$-\frac{2\mu(1+\nu)fhmb\sin\beta\cos\varphi}{(1-\nu)d} + \frac{\mu(mb)^2(1-\nu\cos^2\beta)}{4\pi(1-\nu)d}\left[\frac{d}{2\pi h}\sinh\left(\frac{2\pi h}{d}\right)\right]$$

$$+\frac{\mu(mb)^2\sin^2\beta\cos^2\varphi}{4\pi(1-\nu)d}\left[\frac{2\pi h}{d}\coth\left(\frac{2\pi h}{d}\right) - \frac{2\pi^2h^2}{d^2}\operatorname{csch}^2\left(\frac{2\pi h}{d}\right) - \frac{1}{2}\right]$$

$$-\frac{\mu(mb)^2\sin^2\beta\sin^2\varphi}{4\pi(1-\nu)d}\left[\frac{2\pi h}{d}\coth\left(\frac{2\pi h}{d}\right) + \frac{2\pi^2h^2}{d^2}\operatorname{csch}^2\left(\frac{2\pi h}{d}\right) - \frac{3}{2}\right]$$

(6.4.10)

All parameters in equation (6.4.10) are defined in Chapter 2. To study the effect of the twin thickness on the total elastic energy of the system, we calculate $(E_{total}/E_0)_{min}$ vs. d at a given value of film thickness h with the number of partials m = 1, 2, 3, 4, ... until the equilibrium twin thickness m_{eq} is found. The results for the film thickness h = 20nm, 100nm, 200nm and 500nm are presented in Fig.6.11 and Table 6.3. All data used for plots are listed in the figure caption. There is no data available for the twin boundary energy γ_T, and the approximation (Hirth and Lothe 1982)

$$\gamma_T = \gamma_{S.F.}/2 \tag{6.4.11}$$

is used in the computation. When m = 1, equation (6.4.10) for twins should be identical to equation (6.4.2) for 90° partial dislocations + stacking faults; equation (6.4.11) passes this test.

Table 6.3 Summary of the equilibrium twin thickness m with different film thickness

Film thickness h (nm)	Equilibrium twin thickness $m_{eq}\times\{111\}$
20	2
100	3
200	5
500	8

It can be seen from Fig.6.11 and Table 6.3 that the equilibrium twin thickness increases with increasing film thickness. The result that m_{eq} = 2 for h = 20nm and m_{eq} = 5 for h = 200nm agrees with the experimental observations reported in this chapter.

Figure 6.12 shows the comparison of strain relaxation by 90° partial dislocations + stacking faults and twinning. It is clear that twinning rather than 90° partial dislocations + stacking faults is a more effective mechanism to relieve the misfit strain. The twin thickness

Figure 6.11

(a)

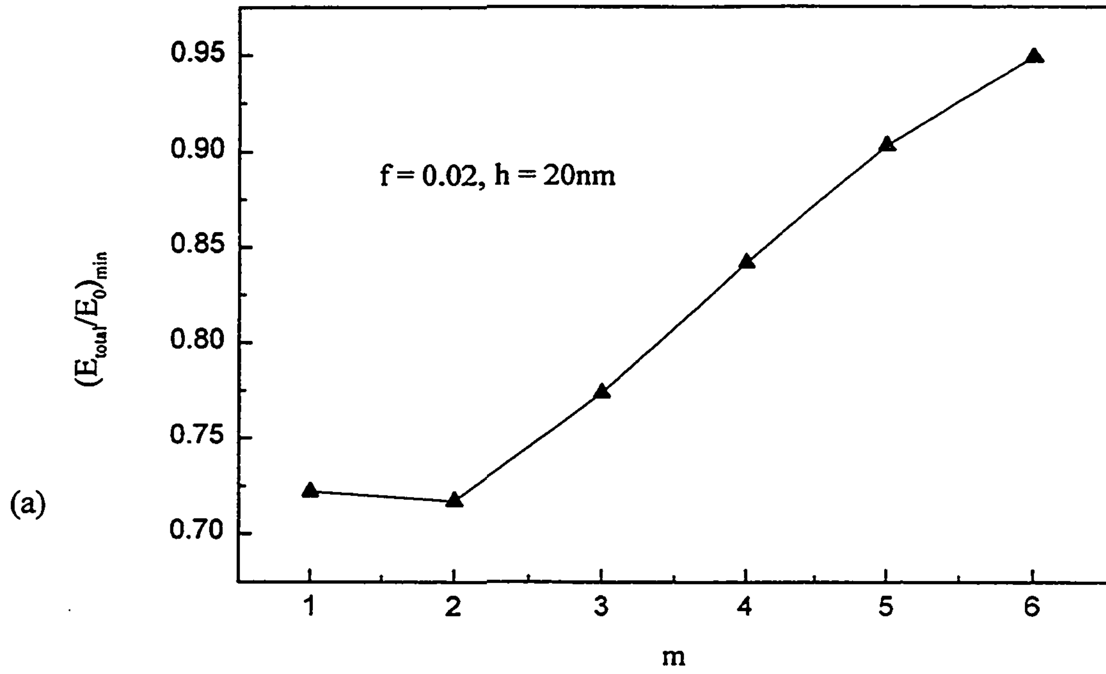

(b)

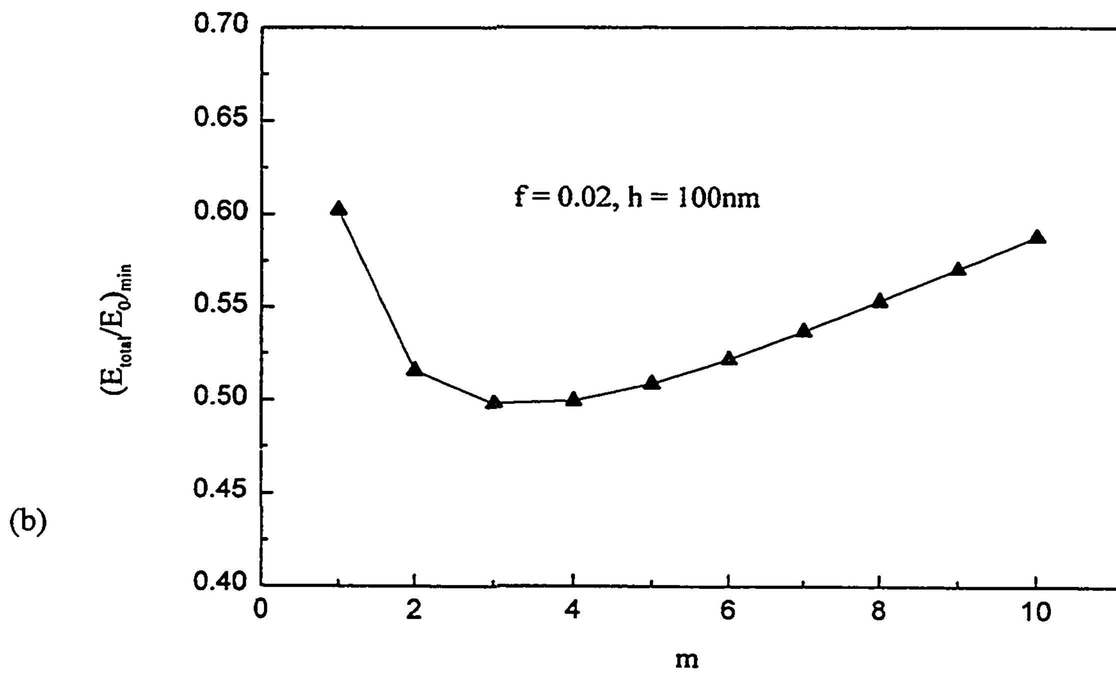

Figure 6.11 (continued)

(c)

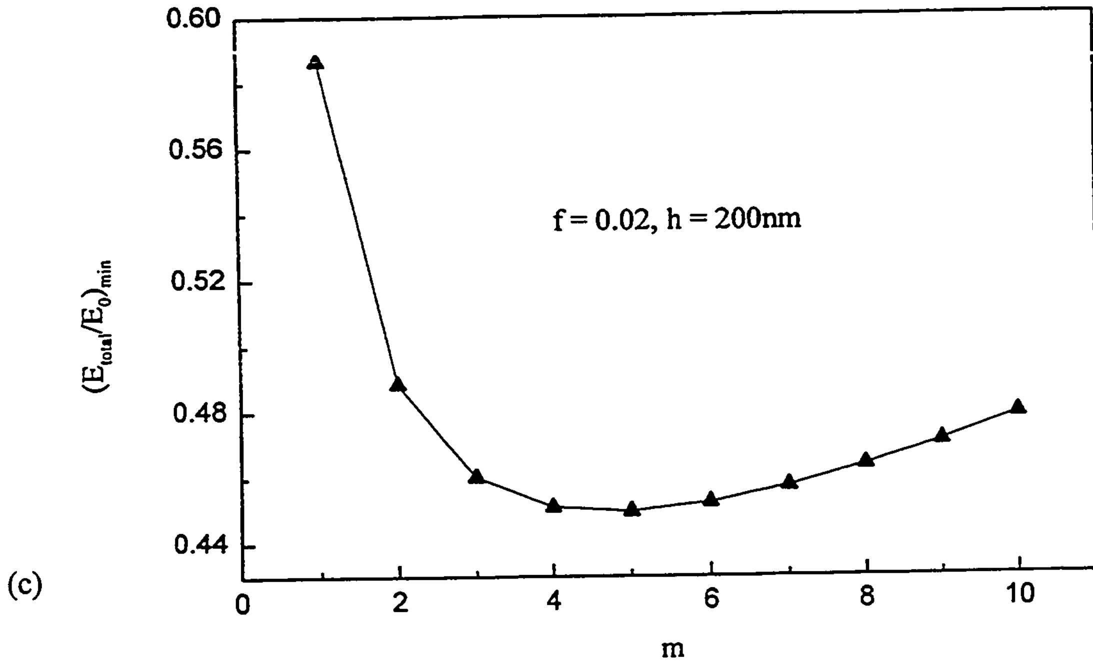

(d)

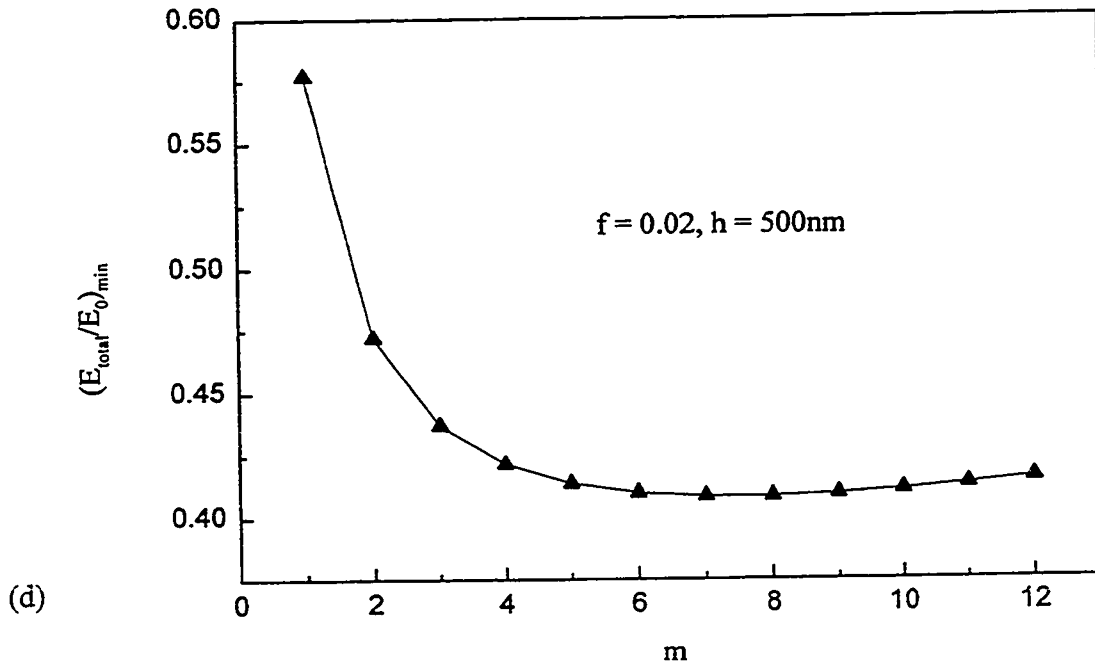

The calculation of total elastic energy of the system with twins $(E_{total}/E_0)_{min}$ vs. twin thickness m for (a) h = 20nm; (b) h = 100nm; (c) h = 200nm and (d) h = 500nm. Data used for plots: μ = 29.1GPa, ν = 0.322, $\gamma_{S.F.}$ = 48.75 mJ/m^2, f = 0.02, b = 2.3493Å, d_p = 4.069 Å, $\gamma_T = \gamma_{S.F.}/2$, $\beta = 90°$, $\varphi = \cos^{-1}\left(1/\sqrt{3}\right)$ and $r_0 = b$.

Figure 6.12

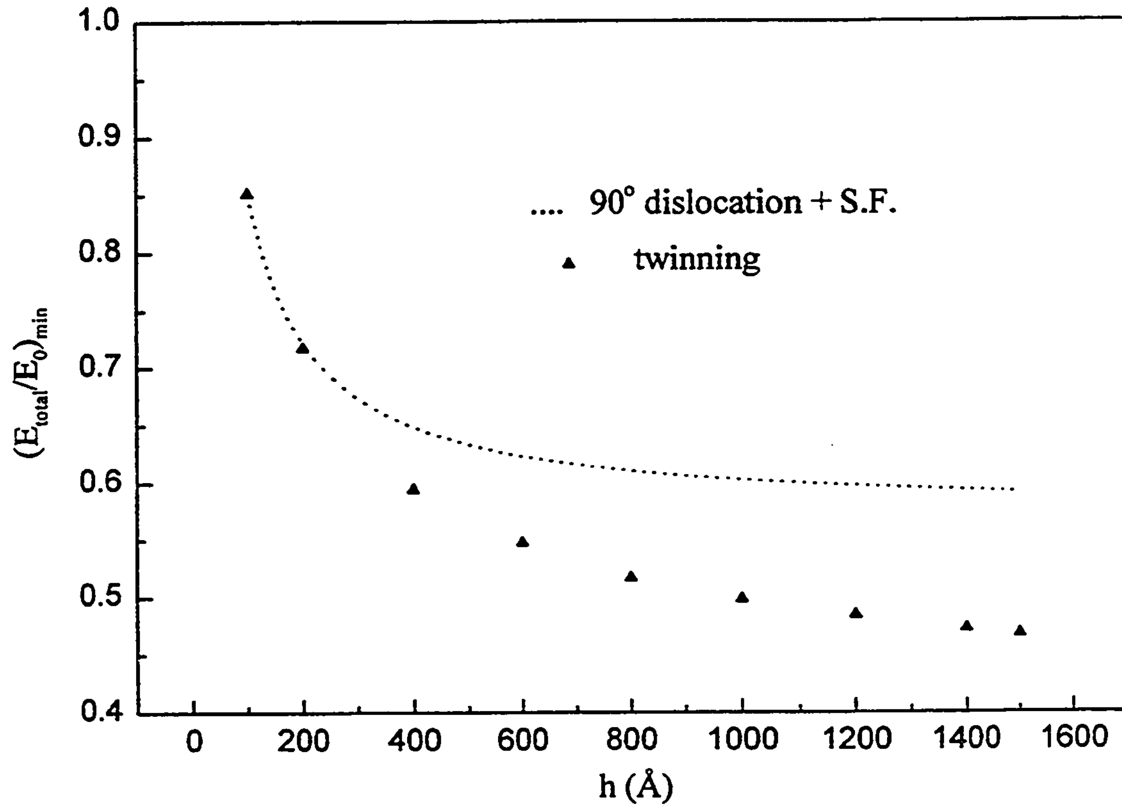

$(E_{total}/E_0)_{min}$ vs. h for 90° partial dislocations + stacking faults and twins. Data used for plots: $\mu = 29.1$GPa, $\nu = 0.322$, $\gamma_{S.F.} = 48.75$ mJ/m^2, $b = 2.3493$Å, $d_p = 4.0691$Å, $f = 0.02$, $\gamma_T = \gamma_{S.F.}/2$, $\beta = 90°$, $\varphi = \cos^{-1}\left(1/\sqrt{3}\right)$ and $r_0 = b$.

increases with an increase in film thickness in order to reduce the contribution of the twin boundary energy to the overall energy of the system. This coarsening takes place even though it leads to an increase in the interaction energy between the partial dislocations acting to relieve the strain in the system because the energy due to twin boundaries increases more rapidly with h than does the interaction energy between twins made up of a cluster of m partials (Dynna *et al.* 1997). Comparing Fig.6.8 with Fig.6.12, it can be concluded that the formation of microtwins in a 2% strained film is the most effective strain relaxation mechanism in all film thicknesses. This is why twins were observed in all the films.

Chapter 7

Equilibrium position of misfit dislocations in thin epitaxial films

7.1 Introduction

As discussed in Chapter 2, the misfit dislocations may not be located directly at the interface if the film has different elastic properties than the substrate. Instead, they shift into the weaker region, i.e. the region where the shear modulus μ is smaller. Semiconductor thin films are usually grown on substrates from the same class of material e.g. $Si_{1-x}Ge_x$/Si, $In_{1-x}Ga_xAs_yP_{1-y}$/InP (or GaAs) systems. The ratio of the shear modulus between the semiconductor film and substrate (μ_f/μ_s or μ_s/μ_f) is then less than 1.5. With such a small difference in shear moduli between the film and substrate, it is expected (Gutkin *et al.* 1989; Mader and Knauss 1992) that the misfit dislocations should be very close to the interface either in the film or substrate, i.e. within a distance of the order of the dislocation core dimensions (a few Å). However, our experimental observations suggest otherwise. Figure 7.1 is a $[0\bar{1}1]$ cross-section TEM image of a 2% tensile strained, 100nm thick $In_{0.25}Ga_{0.75}As$ film grown on a (100) InP substrate. The 90° leading partial dislocations bounded by stacking faults are frequently observed to locate inside the InP substrate over a range of a few hundred angstroms. The ratio of the shear moduli of the $In_{0.25}Ga_{0.75}As$ film and the InP substrate (μ_f/μ_s) is 1.3. Analyses based on two semi-infinite solids (Gutkin *et al.* 1989; Mader and Knauss 1992) cannot be used to predict the position of misfit dislocations in a thin epitaxial film-substrate combination where typically the thickness of the epitaxial film (h) is orders of magnitude smaller than the thickness of the substrate (h_s). Under this condition, the presence of the free surface is extremely important and destroys the symmetry found with the two semi-infinite

Figure 7.1

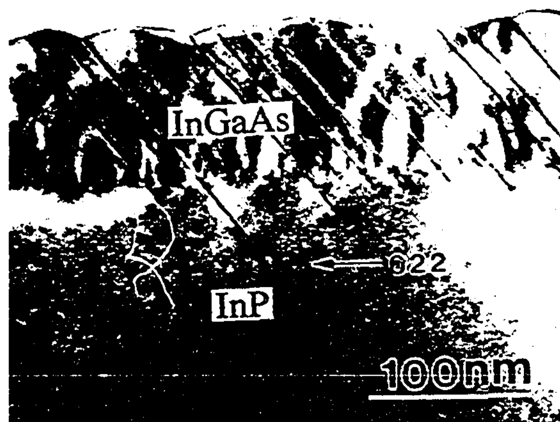

$[0\bar{1}1]$ cross-section TEM bright field image (g = 022) of 100nm thick, 2% tensile strained $In_{0.25}Ga_{0.75}As$ film on InP substrate. The 90° partial dislocations bounded by stacking faults penetrate some distance into the substrate.

crystal geometry.

In this Chapter, the equilibrium position of a mixed dislocation in a thin film is studied. In solving this problem we have followed the approach of Head (1953a,b), who introduced the concept of image dislocations to account for the presence of both a free surface and an interface where there is a discontinuity in the elastic properties (see Chapter 2). The force analysis developed in this chapter is approximate for edge or mixed dislocations, and is only expected to hold for conditions $0.67 < \mu_f/\mu_s < 1.5$, as shown by the more complete analysis of this problem due to Weeks *et al.* (1968). However, this range of μ_f/μ_s covers all practical semiconductor combination of interest in epitaxy.

7.2 Force on dislocation

The geometry of the film-substrate combination is shown in Fig.7.2 for the condition where the substrate is elastically softer and has a larger lattice parameter than the film. The film is then under bi-axial tension, while the substrate is under bi-axial compression. Using the method for uniaxial case (Mader and Knauss 1992), it can be shown that bi-axial stresses are given by

$$\sigma_{xx}^f = \frac{2h_s\mu_f\mu_s(1+\nu)f}{(h_s\mu_s + h\mu_f)(1-\nu)}$$

$$\sigma_{yy}^f = 0 \qquad (7.2.1)$$

$$\sigma_{xy}^f = 0$$

in the film, and

Figure 7.2

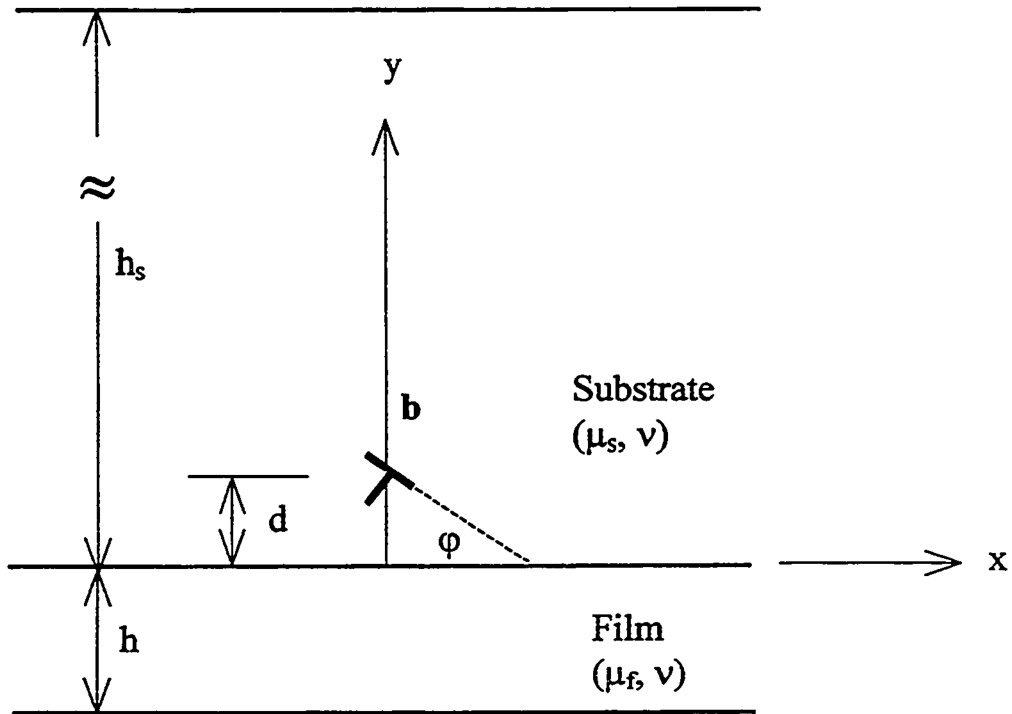

Schematic illustration of film-substrate media containing a misfit dislocation **b**.

$$\sigma_{xx}^{s} = -\frac{h}{h_s}\sigma_{xx}^{f} = -\frac{2h\mu_f\mu_s(1+\nu)f}{(h_s\mu_s + h\mu_f)(1-\nu)}$$

$$\sigma_{yy}^{s} = 0 \qquad (7.2.2)$$

$$\sigma_{xy}^{s} = 0$$

in the substrate.

μ_f and μ_s are the shear moduli of the film and substrate, ν is Poission's ratio (assumed to be the same in both the film and substrate), h and h_s are the thicknesses of the film and substrate, and f is the misfit between the lattice parameters of the bounding phases.

A single edge dislocation **b** = (bcosφ,bsinφ,0) is introduced into the softer phase, lying at a point (0,d) from the interface and at a distance (h+d) from the free surface (Fig.7.2). Since the dislocation slip and climb directions are of interest, a new co-ordinate system x', y' is established where x' direction is parallel to the dislocation slip direction and y' direction is parallel to the dislocation climb direction. By a standard transformation procedure (see equation (A11) in Appendix), the stresses in the new co-ordinate system x',y' are given by

$$\sigma_{x'x'}^{f} = \frac{\sigma_{xx}^{f}}{2}(1+\cos 2\varphi) = \frac{h_s\mu_f\mu_s(1+\nu)f}{(h_s\mu_s + h\mu_f)(1-\nu)}(1+\cos 2\varphi)$$

$$\sigma_{y'y'}^{f} = \frac{\sigma_{xx}^{f}}{2}(1-\cos 2\varphi) = \frac{h_s\mu_f\mu_s(1+\nu)f}{(h_s\mu_s + h\mu_f)(1-\nu)}(1-\cos 2\varphi) \qquad (7.2.3)$$

$$\sigma_{x'y'}^{f} = -\frac{\sigma_{xx}^{f}}{2}\sin 2\varphi = -\frac{h_s\mu_f\mu_s(1+\nu)f}{(h_s\mu_s + h\mu_f)(1-\nu)}\sin 2\varphi$$

in the film, and

$$\sigma^s_{x'x'} = \frac{\sigma^s_{xx}}{2}(1+\cos 2\varphi) = -\frac{h\mu_f\mu_s(1+\nu)f}{(h_s\mu_s + h\mu_f)(1-\nu)}(1+\cos 2\varphi)$$

$$\sigma^s_{y'y'} = \frac{\sigma^s_{xx}}{2}(1-\cos 2\varphi) = -\frac{h\mu_f\mu_s(1+\nu)f}{(h_s\mu_s + h\mu_f)(1-\nu)}(1-\cos 2\varphi) \qquad (7.2.4)$$

$$\sigma^s_{x'y'} = -\frac{\sigma^s_{xx}}{2}\sin 2\varphi = \frac{h_s\mu_f\mu_s(1+\nu)f}{(h_s\mu_s + h\mu_f)(1-\nu)}\sin 2\varphi$$

in the substrate.

The total climb force (F_y) acting on the dislocation shown in Fig.7.2 arises from three factors: (a) the interaction between the dislocation and the stress in the substrate, (b) the interaction between the dislocation and the free surface, and (c) the interaction between the dislocation and the interface. The solution to (a), the Peach-Koehler force, is given by (Hirth and Lothe 1982)

$$F_y^{p-k} = \sigma^s_{x'x'} b\cos\varphi + \sigma^s_{x'y'} b\sin\varphi = \sigma^s_{xx} b\cos\varphi\cos 2\varphi = -\frac{2h\mu_f\mu_s(1+\nu)fb}{(h_s\mu_s + h\mu_f)(1-\nu)}\cos\varphi\cos 2\varphi \qquad (7.2.5)$$

The solutions to (b) and (c) can be obtained from Head and Mura's analysis (Head 1953a and 1953b; Mura 1968) and are presented in the Appendix (see equation A15). The total force acting on the dislocation is given by

$$F_y = -\frac{2h\mu_f\mu_s(1+\nu)fb}{(h_s\mu_s + h\mu_f)(1-\nu)}\cos\varphi\cos 2\varphi + \frac{\mu_s b^2}{4\pi(1-\nu)d}\left[m - (1-m^2)\sum_{i=1}^{\infty}\frac{d}{d+ih}m^{i-1}\right]\cos 2\varphi \qquad (7.2.6)$$

m, which can be thought of as the strength of the first image dislocation (see Appendix),

located at (0,-d), is given by $-\frac{1}{2}(A+B)$, where $A=\frac{1-\Gamma}{1+\kappa\Gamma}$, $B=\frac{\kappa(1-\Gamma)}{\kappa+\Gamma}$, $\kappa=3-4\nu$, and $\Gamma=\frac{\mu_f}{\mu_s}$.

From equations (7.2.6) and (A17), we can readily obtain the total force acting along the y direction for a mixed dislocation lying in the substrate as:

$$F_y=-\frac{2h\mu_f\mu_s(1+\nu)fb}{(h_s\mu_s+h\mu_f)(1-\nu)}\sin\beta\cos\varphi\cos2\varphi$$

$$+\frac{\mu_s b^2\sin^2\beta}{4\pi(1-\nu)d}\left[m-(1-m^2)\sum_{i=1}^{\infty}\frac{d}{d+ih}m^{i-1}\right]\cos2\varphi+\frac{\mu_s b^2\cos^2\beta}{4\pi d}\left[p-(1-p^2)\sum_{i=1}^{\infty}\frac{d}{d+ih}p^{i-1}\right]$$

(7.2.7)

where β is the angle between the Burgers vector of the dislocation and the dislocation line, φ is the angle between the slip plane and the free surface (interface), and $p=\frac{\Gamma-1}{\Gamma+1}$ with $\Gamma=\frac{\mu_f}{\mu_s}$.

The situation where the film is softer than the substrate follows the same reasoning, but now the dislocation core is located in the film. In this case the force F_y is given by

$$F_y=\frac{2h_s\mu_f\mu_s(1+\nu)fb}{(h_s\mu_s+h\mu_f)(1-\nu)}\sin\beta\cos\varphi\cos2\varphi$$

$$-\frac{\mu_f b^2\sin^2\beta}{4\pi(1-\nu)d}\left[n-(1-n^2)\sum_{i=1}^{\infty}\frac{d}{ih-d}n^{i-1}\right]\cos2\varphi-\frac{\mu_f b^2\cos^2\beta}{4\pi d}\left[q-(1-q^2)\sum_{i=1}^{\infty}\frac{d}{ih-d}q^{i-1}\right]$$

(7.2.8)

where $n = -\frac{1}{2}(A'+B')$, with $A' = \frac{1-\Gamma'}{1+\kappa\Gamma'}$, $B' = \frac{\kappa(1-\Gamma')}{\kappa+\Gamma'}$, $\kappa = 3-4\nu$, $q = \frac{\Gamma'-1}{\Gamma'+1}$ and $\Gamma' = \frac{\mu_s}{\mu_f}$.

For an edge dislocation in the substrate with Burger vector parallel to the free surface or interface, $\beta = 90°$, $\varphi = 0°$, equation (7.2.7) becomes

$$F_y = -\frac{2h\mu_f\mu_s(1+\nu)fb}{(h_s\mu_s + h\mu_f)(1-\nu)} + \frac{\mu_s b^2}{4\pi(1-\nu)d}\left[m - (1-m^2)\sum_{i=1}^{\infty}\frac{d}{d+ih}m^{i-1}\right] \tag{7.2.9}$$

If $h_s \gg h$, equation (7.2.9) becomes

$$F_y = \frac{\mu_s b^2}{4\pi(1-\nu)d}\left[m - (1-m^2)\sum_{i=1}^{\infty}\frac{d}{d+ih}m^{i-1}\right] \tag{7.2.10}$$

This is the equation for the dislocation in the unstrained substrate because $\sigma_{ij}^s \approx 0$ when $h_s \gg h$.

Some well known results can be recovered from equation (7.2.10) in the following limiting cases:

(1) $\Gamma = 0$, (i.e. $\mu_f = 0$, $A = B = 1$, $m = -1$).

$$F_y = -\frac{\mu_s b^2}{4\pi(1-\nu)d} \tag{7.2.11}$$

This is the force acting on an edge dislocation, a distance d from a free surface in a semi-infinite solid.

(2) $\Gamma = 1$, (i.e. $\mu_f = \mu_f$, $A = B = 0$, $m = 0$).

$$F_y = -\frac{\mu_s b^2}{4\pi(1-\nu)(d+h)} \tag{7.2.12}$$

This is the force acting on an edge dislocation, a distance (d+h) from a free surface in a semi-infinite solid.

(3) $\Gamma=\infty$, ($A=-1/\kappa$, $B=-\kappa$, $m=\frac{\kappa^2+1}{2\kappa}$).

$$F_y=\frac{\mu_s b^2}{4\pi(1-\nu)}\frac{\kappa^2+1}{2\kappa} \tag{7.2.13}$$

This is the result of having a rigid boundary at y = 0. Since $F_y > 0$, the dislocation would always be repelled from the interface in this case.

(4) $h=\infty$,

$$F_y=\frac{\mu_s b^2}{4\pi(1-\nu)}m \tag{7.2.14}$$

This is the result for the two semi-infinite crystals case given by Mader and Knauss (1992).

7.3 Equilibrium position of misfit dislocation

For a dislocation to be at equilibrium, the total force acting on the dislocation must vanish. Therefore the equilibrium position can be determined by solving $F_y = 0$. For simplification, we discuss an edge dislocation with Burgers vector parallel to the free surface or interface. In this case $\beta = 90°$, $\varphi = 0°$. The equilibrium position is given by:

$$-\frac{2h\mu_f\mu_s(1+\nu)fb}{(h_s\mu_s+h\mu_f)(1-\nu)}+\frac{\mu_s b^2}{4\pi(1-\nu)d}\left[m-(1-m^2)\sum_{i=1}^{\infty}\frac{d}{d+ih}m^{i-1}\right]=0 \quad (\text{if } \mu_f>\mu_s) \tag{7.3.1}$$

for the dislocation located in the substrate, and

$$\frac{2h_s\mu_f\mu_s(1+\nu)fb}{(h_s\mu_s+h\mu_f)(1-\nu)}-\frac{\mu_f b^2}{4\pi(1-\nu)d}\left[n-(1-n^2)\sum_{i=1}^{\infty}\frac{d}{ih-d}n^{i-1}\right]=0 \qquad (\text{if } \mu_s>\mu_f) \tag{7.3.2}$$

for the dislocation located in the film.

If $h_s = h \gg d$, equations (7.3.1) and (7.3.2) become

$$\frac{d}{b}=\frac{(1+\Gamma)m}{8\pi(1+\nu)\Gamma f} \tag{7.3.3}$$

and

$$\frac{d}{b}=\frac{(1+\Gamma')n}{8\pi(1+\nu)\Gamma' f} \tag{7.3.4}$$

Equations (7.3.3) and (7.3.4) are identical to Mader and Knauss's (1992) solution for the equilibrium position of the dislocation for the case of two semi-infinite crystals (see equation (2.2.26) in Chapter 2). (Mader and Knauss (1992) considered a uniaxial misfit; taking their expression for σ^s_{xx} leads to $\frac{d}{b}=\frac{(1+\Gamma)m}{8\pi\Gamma f}$ and $\frac{d}{b}=\frac{(1+\Gamma')n}{8\pi\Gamma' f}$ in our terminology.) If $\mu_f = \mu_s$, then $m = n = 0$, and both equations (7.3.3) and (7.3.4) give $d/b = 0$, i.e. the dislocation is located in the interface as expected.

If $h_s \gg h$, equations (7.3.1) and (7.3.2) become

$$m-(1-m^2)\sum_{i=1}^{\infty}\frac{d}{d+ih}m^{i-1}=0 \qquad (\text{if } \mu_f>\mu_s) \tag{7.3.5}$$

for the dislocation located in the substrate, and

$$8\pi(1+\nu)f\frac{d}{b}-n+(1-n^2)\sum_{i=1}^{\infty}\frac{d}{ih-d}n^{i-1}=0 \qquad (\text{if } \mu_f<\mu_s) \tag{7.3.6}$$

for the dislocation located in the film.

Equations (7.3.5) and (7.3.6) clearly demonstrate the asymmetry in the behavior anticipated in the Introduction. If the dislocation lies in the substrate, the climb force due to the misfit f (driving it back to the interface) is essentially zero ($|\sigma^f_{xx}| \gg |\sigma^s_{xx}|$), and the equilibrium position

is given by Head's original analysis (Head 1953b). On the other hand if the dislocation lies in the film, there is a substantial climb force (due to σ^f_{xx}) driving the dislocation towards the interface. At large values of f, this term dominates the behavior and the equilibrium position of the dislocation is very close to the interface.

Figures 7.3 and 7.4 compare the predictions of the equilibrium position of the isolated edge dislocation given by the two expressions, equations (7.3.1) and (7.3.2), assuming ν = 0.3, (i.e. κ = 1.8), b = 4Å and h_s = 375μm. In Figure 7.3, the equilibrium position (d/b) is compared for a film thickness h = 100nm over a range of values of shear modulus ratio from 1 to 2 for values of misfit f from 1×10^{-3} to 2×10^{-2}. If the dislocation lies in the film ($\mu_s > \mu_f$) (Fig.7.3b), the equilibrium position is closer to the interface by at least an order of magnitude in comparison to the situation where $\mu_f > \mu_s$ (with the dislocation in the substrate) (Fig.7.3a), over the whole range of misfit values considered. Figure 7.4 shows the influence of the film thickness h in the range 20 to 200nm at a misfit of $f = 10^{-2}$ for the two situations. There is a strong dependence of the equilibrium position on h when the dislocation lies in the substrate (Fig.7.4a), but little variation when the dislocation lies in the film for this value of f (Fig.7.4b).

Figure 7.5 is a comparison of the equilibrium position of an edge dislocation (equation (7.3.5)) and a screw dislocation (F_s = 0 from equation (A16)) vs. μ_f/μ_s, assuming $\nu_f = \nu_s = 1/4$ for values of $\mu_f/\mu_s < 3.5$. For small values of μ_f/μ_s (< 1.5), there is little difference in the equilibrium position between edge and screw dislocations. This agrees with results obtained by Weeks *et al.* (1968) who studied the equilibrium position of an edge dislocation near an

Figure 7.3

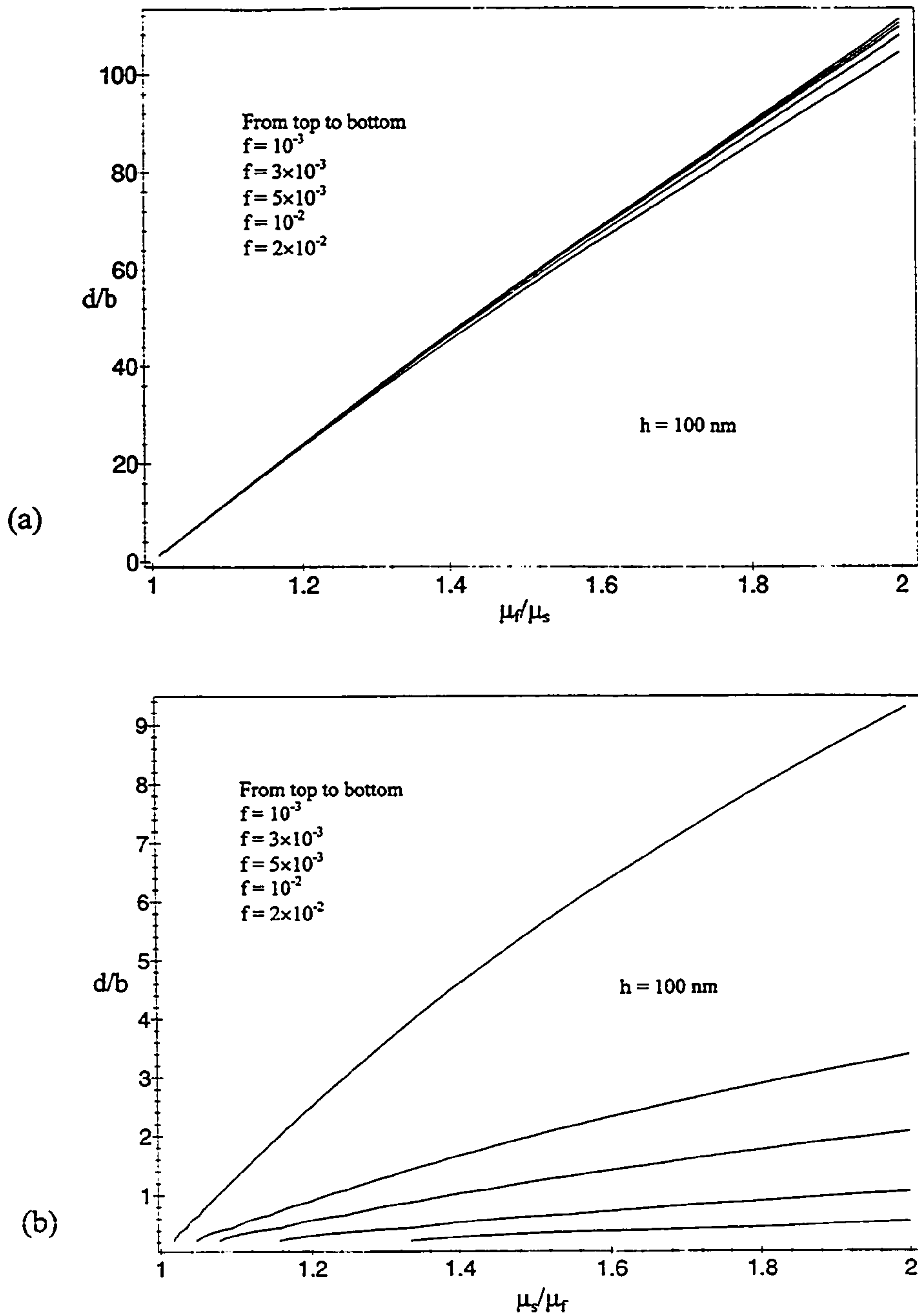

The dependence of dislocation equilibrium position on the ratio of shear modulus at various misfit (h_s = 375μm, h = 100nm, ν = 0.3 and b = 4Å). (a) d/b vs. μ_f/μ_s for the isolated dislocation located in the substrate. (b) d/b vs. μ_s/μ_f for the isolated dislocation located in the film.

Figure 7.4

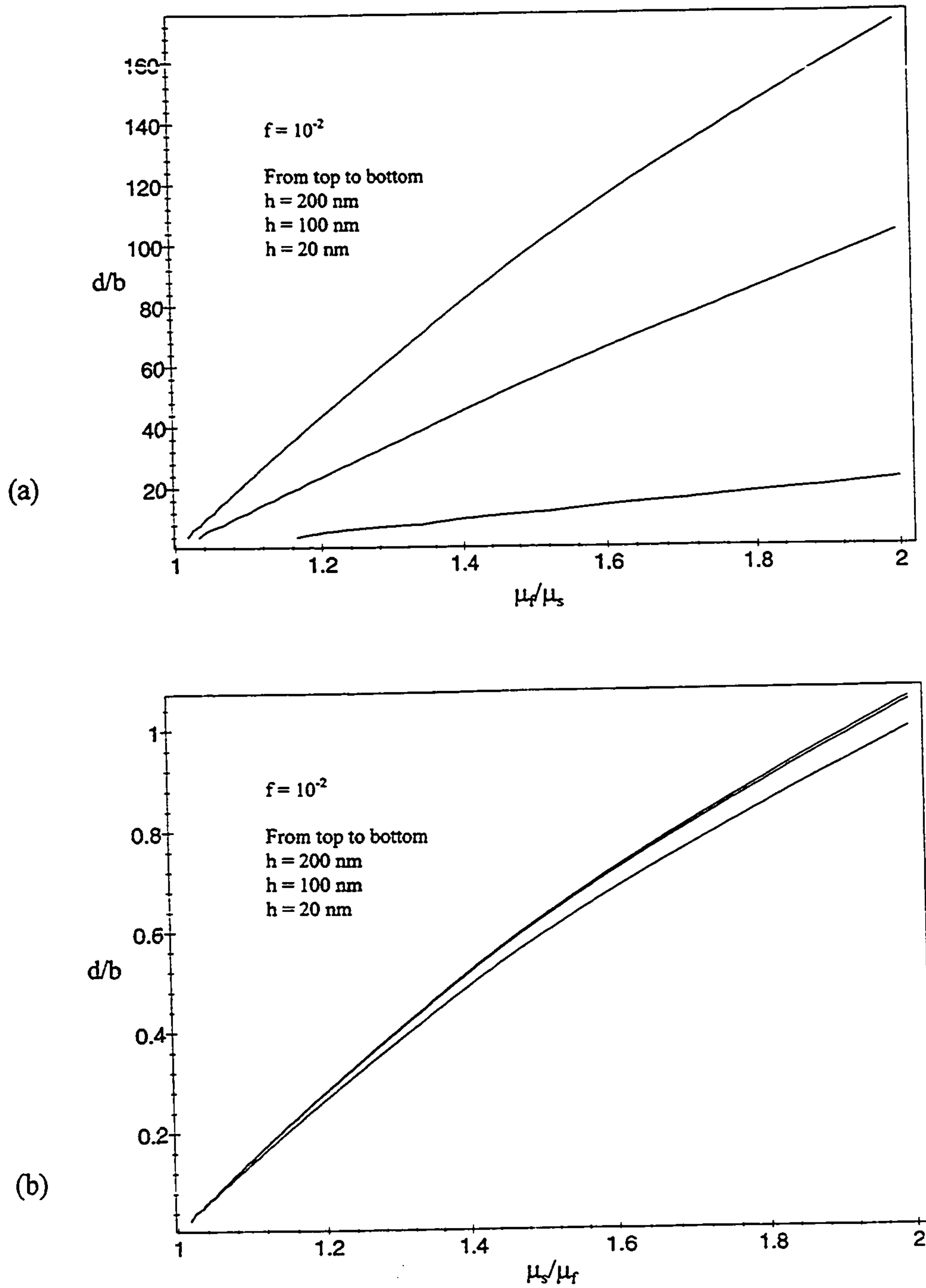

The dependence of dislocation equilibrium position on the ratio of shear modulus at various film thickness ($h_s = 375\mu m$, $f = 10^{-2}$, $\nu = 0.3$ and $b = 4Å$). (a) d/b vs. μ_f/μ_s for the isolated dislocation located in the substrate. (b) d/b vs. μ_s/μ_f for the isolated dislocation located in the film.

Figure 7.5

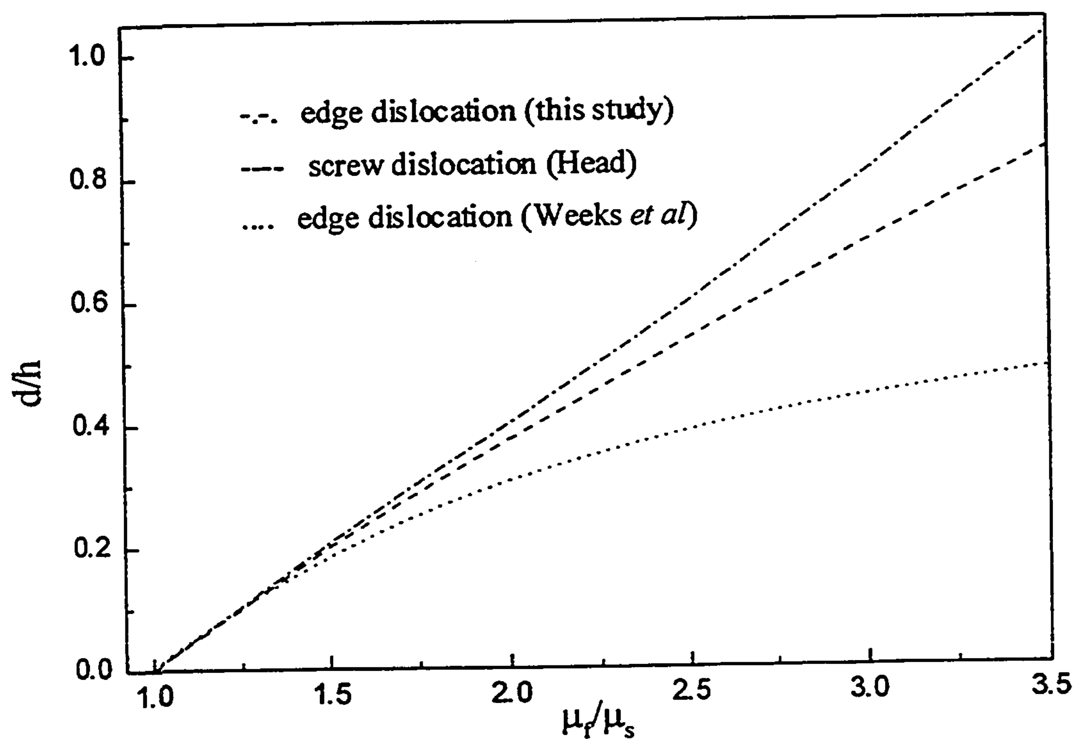

Equilibrium position vs. μ_f/μ_s for an edge dislocation and a screw dislocation lying in the substrate.

surface layer using the Papkovich-Neuber potential method. However, Fig.7.5 shows that the difference in the equilibrium positions between edge and screw dislocations increases slightly with an increase in μ_f/μ_s, and the screw dislocation is always slightly closer to the interface. This is very different than the result of Weeks *et al.* (1968) who found that at large values of μ_f/μ_s, an edge dislocation is predicted to be much closer to the interface than a screw dislocation (see Fig.7.5). However, as noted earlier, in the growth of semiconducting (group IV or III-V) epitaxial films, the ratio of shear moduli between semiconductor film and substrate (μ_f/μ_s or μ_s/μ_f) is less than 1.5. Therefore we believe that the predictions made in this study should be reasonable for semiconductor film growth.

7.4 Application to III-V films

Consider first the role of partial dislocations. As discussed in Chapter 4,5,6 and this chapter, a frequently observed plastic strain relaxation mechanism in III-V thin films is the formation of 90° partial dislocations bounded by stacking faults/microtwins lying on {111} fault (slip) planes. Figure 7.6 shows the force (F) vs. d for a 90° partial dislocation on a {111} plane lying in the substrate ($\mu_f > \mu_s$) (the solid line in Fig.7.6, using equation (7.2.7) with β = 90° and φ = 54.74°). The data used for this plot are taken from the $In_{0.25}Ga_{0.75}As$(f)/InP(s) system and are listed in the figure caption. The dislocation is repelled from the interface (positive F) for d < 137Å, while it is attracted to the interface (negative F) for d > 137Å. However, to predict the equilibrium position of the dislocation precisely, the force due to the stacking fault should be added to the total force expression in equation (7.2.7). Taking this force into account, the equilibrium position of the dislocation is predicted to be d = 59Å,

Figure 7.6

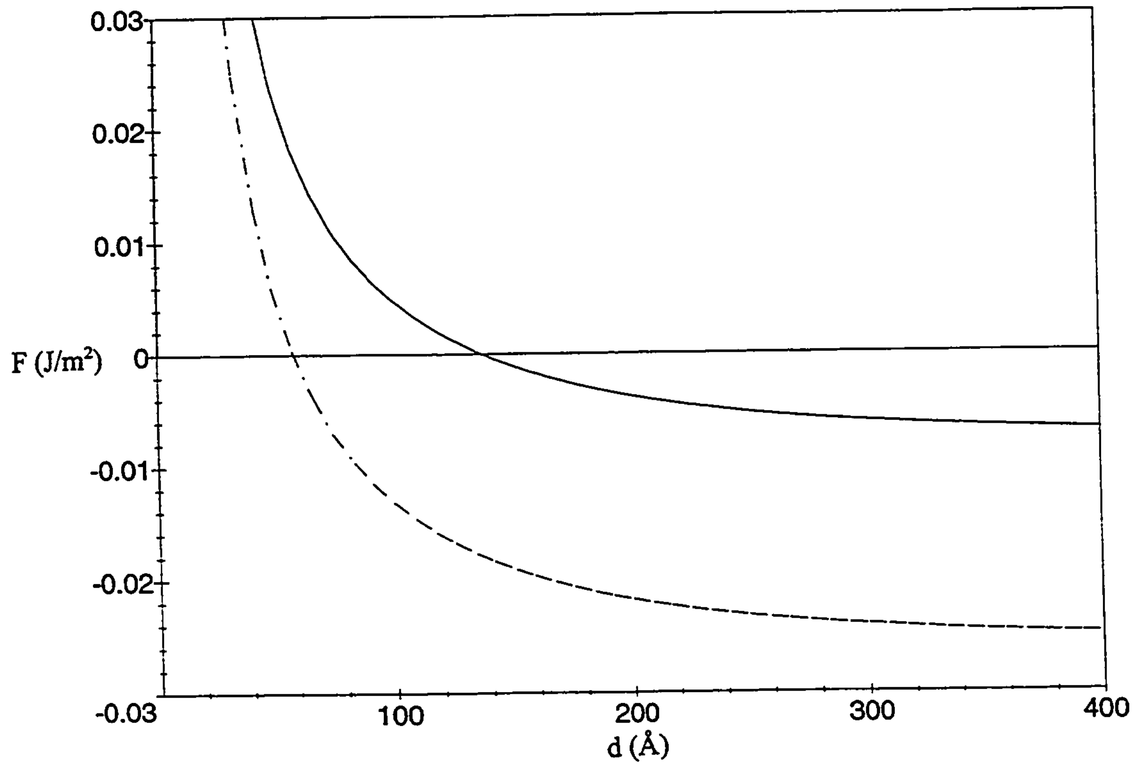

The dependence of the total force (F) on the dislocation position (d) for the isolated 90° dislocation located in the substrate. The solid line: without the force due to stacking fault; the dash line: with the force due to stacking fault. (μ_f= 29.1GPa, μ_s = 22.3GPa, ν = 0.34, h_s = 375μm, h = 100nm, b = 2.3493Å f = 10^{-2} and $\gamma_{S.F.}$ = 18mJ/m^2).

using $\gamma_{S.F} = 18mJ/m^2$ (Hottschalk *et al.* 1978). Note that in this case, the stacking fault energy used is the value for InP, as the partial dislocation bounding the fault is extended into the InP substrate. We believe that this is the explanation for the observation that the stacking faults/microtwins relieving the misfit strains are often extended into the substrate in the InGaAs/InP system.

Another plastic strain relaxation mechanism in the growth of semi-conducting (group IV or III-V) epitaxial layers, on <100> oriented substrate, is the formation of 60° (a/2)<011> dislocations gliding on {111} planes, i.e. β = 60°, φ = 54.74°. Figure 7.7 compares the predictions of the equilibrium position d/b for the edge dislocation and the 60° dislocation (from equation (7.3.1) and (7.2.7)) for a film thickness h = 100nm and a substrate thickness h_s = 375μm over the same range of μ_f / μ_s and misfit (f) values shown in Fig.7.3 and 7.4. It is clear that the offset of the edge and 60° dislocations from the interface is very similar.

Figure 7.7

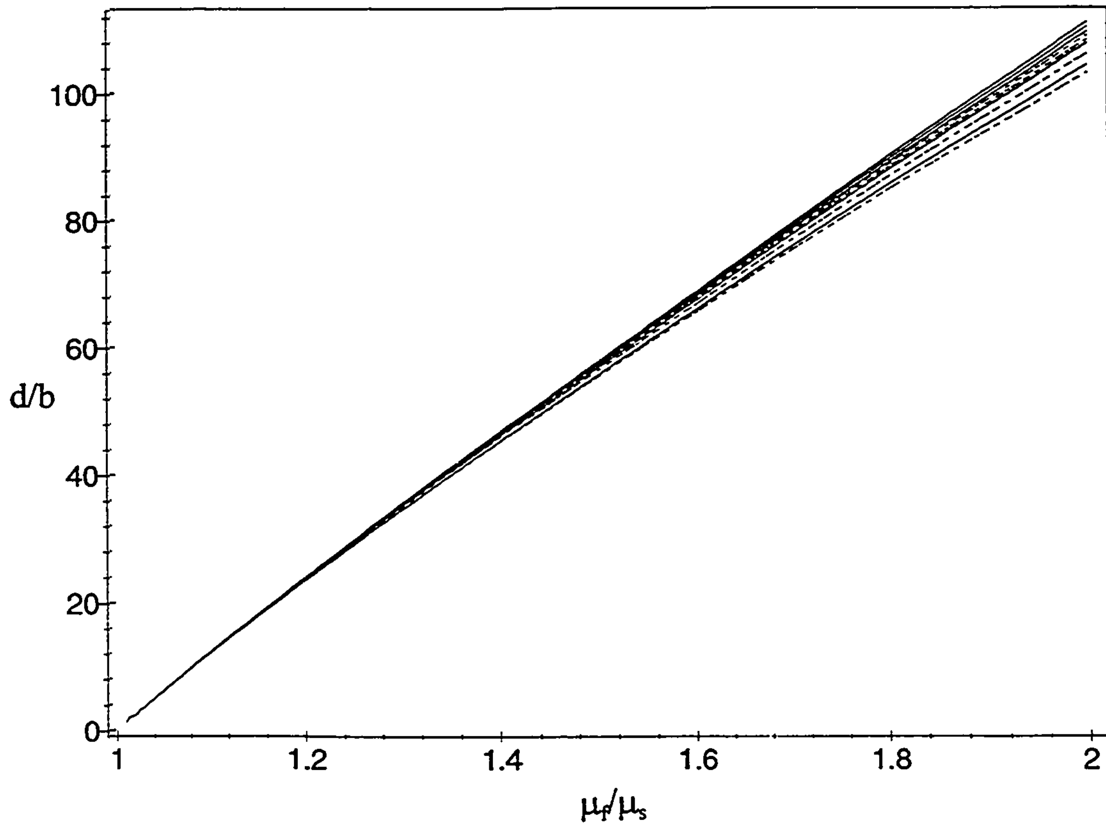

Comparison of the dependence of the equilibrium position (d/b) on the ratio of shear modulus (μ_f/μ_s) at various misfit (see figure 7.3a) for the isolated dislocation located in the substrate. The dash line: edge dislocation; the solid line: 60° dislocation ($h_s = 375\mu m$, $h = 100nm$, $\nu = 0.3$ and $b = 4Å$).

Chapter 8

Composition modulations in tensile strained InGaAsP films

8.1 Observations

In this chapter, a study of the composition modulations in III-V heteroepitaxial films is presented. 0.6% tensile strained $In_{0.45}Ga_{0.55}As$ layers, 2% tensile strained $In_{0.25}Ga_{0.75}As$ layers and 2% tensile strained $In_{0.5}Ga_{0.5}As_{0.5}P_{0.5}$ layers were chosen for this study. Figure 8.1 are the TEM images of an 0.5 μm thick, 0.6% tensile strained $In_{0.45}Ga_{0.55}As$ film capped by a lattice-matched $In_{0.53}Ga_{0.47}As$ film. The faceted growth surface of the 0.6% tensile strained $In_{0.45}Ga_{0.55}As$ film can be seen in Fig.8.1a,b; it is composed of facets with plane indices close to (411) and $(4\bar{1}\bar{1})$. Composition modulation scaling with the size of facets aligned normal to the [011] direction is visible in the lattice-mismatched $In_{0.45}Ga_{0.55}As$ film (Fig.8.1a): the compositional modulations are the lines of black and white contrast seen in the peak and valley regions of the faceted surface respectively. In this film, a composition modulation along [411] and $[4\bar{1}\bar{1}]$ directions was also observed, which is well defined by the faceted surface (Fig.8.1a,b). When a lattice-matched layer is grown on top of a tensile strained layer surface, the fine scale composition modulation with wavelength of about 10 nm re-appears (Fig.8.1c). Furthermore, this fine scale composition modulation remains for the whole film thickness, and no large-scale composition modulation was observed in this lattice-matched layer.

Figure 8.2 is a series of $[0\bar{1}1]$ cross-sectional TEM images of a 2 μm thick, 0.6% tensile strained $In_{0.45}Ga_{0.55}As$ film. The composition modulation is not uniform in this film. A fine scale composition modulation with a wavelength of about 10 nm aligned normal to the

Figure 8.1

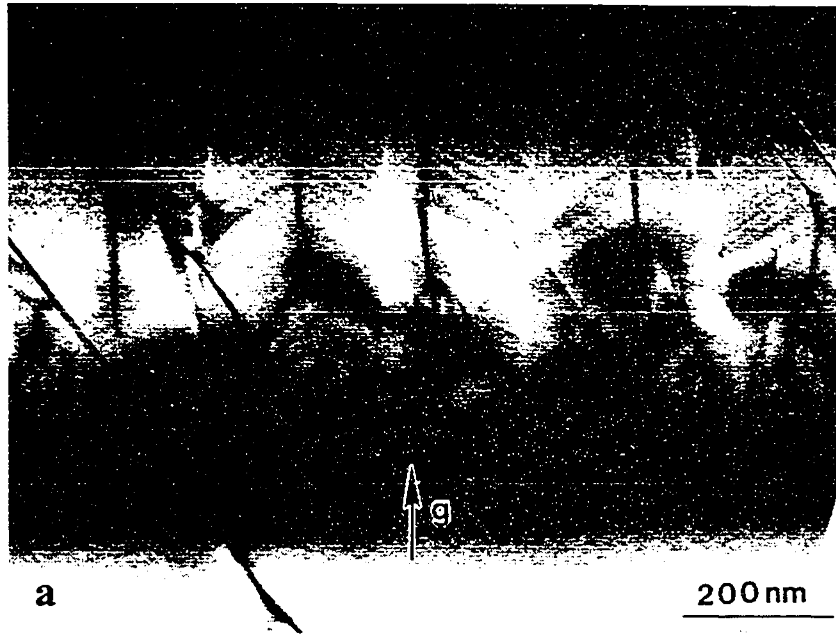

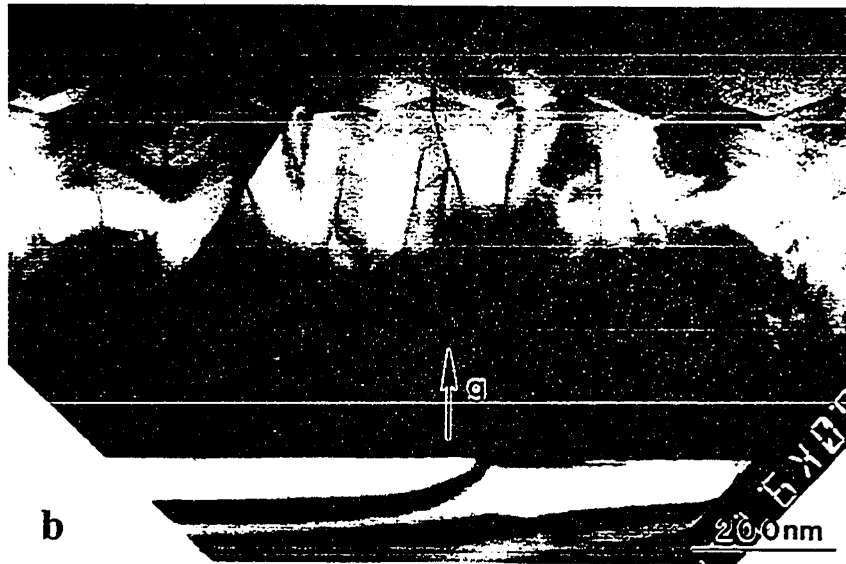

Figure 8.1 (continued)

$[0\bar{1}1]$ cross-section TEM images of 0.5 μm thick, 0.6% tensile strained $In_{0.45}Ga_{0.55}As$ film capped by lattice-matched $In_{0.53}Ga_{0.47}As$. g = 200 for all images.

[011] direction was observed at the initial stage of strained film growth (Fig.8.2a,b,c). The behavior of the composition modulation changes drastically after the film thickness reaches about 100 nm. Composition modulation scaling with the size of facets aligned normal to the [011] direction is visible in the film thickness of 100 nm to 1 μm (Fig.8.2a,b,c). However, in the upper part (1 μm to 2 μm) of this film, the wavelength of composition modulation is gradually reduced as the film thickness increases (Fig.8.2d,e,f). At the top of the film, fine scale composition modulations with wavelength about 10 nm re-appear (Fig8.2f), which is identical to those found in the unstrained film (Fig.8.1c). In addition to the composition modulation along [011] direction, composition modulation along [411] and $[4\bar{1}\bar{1}]$ directions, well defined by the faceted growth surface, was again observed in the film thickness range of about 0.2 μm to 1 μm.

Figure 8.3 is a $[0\bar{1}1]$ cross-section TEM image of 0.5 μm thick, 2% tensile strained $In_{0.25}Ga_{0.75}As$ film. No composition modulation was observed in this film. The morphology of the surface of this film is the same as that of the 0.6% tensile strained $In_{0.45}Ga_{0.55}As$ film, composed of facets with plane indices close to (411) and $(4\bar{1}\bar{1})$. Another distinct feature in this higher tensile strained sample is a high-density of twins and dislocations, which implies that considerable plastic relaxation has occurred.

The 2% tensile strained quaternary $In_{0.5}Ga_{0.5}As_{0.5}P_{0.5}$ film shows different structures than the ternary $In_{0.25}Ga_{0.75}As$ film with the same magnitude of strain. Throughout the whole 0.5 μm thickness of the film, only a fine scale composition modulation is visible (Fig.8.4). The contrast associated with a composition modulation is not obvious with g = 200 reflection (Fig.8.4b), while strong contrast appears with g = 022 reflection (Fig.8.4a). The surface of the

Figure 8.2

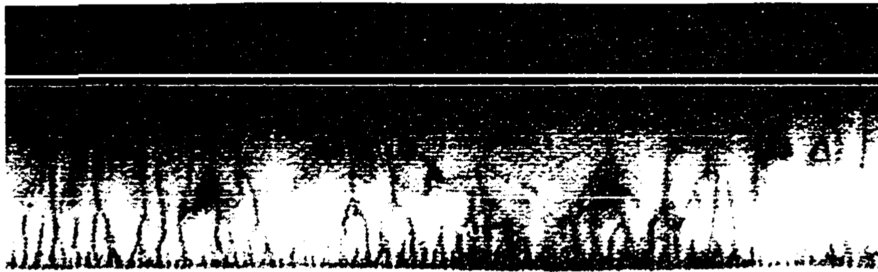

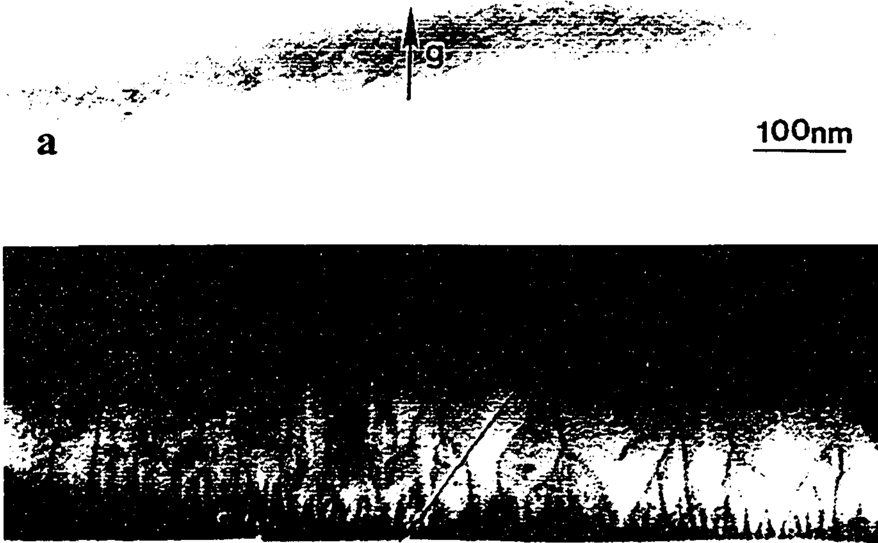

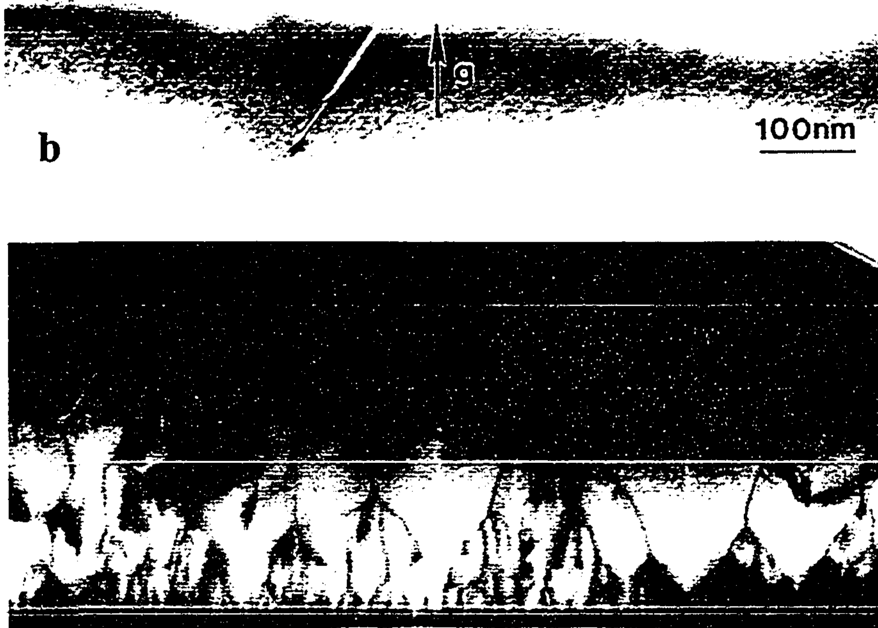

Figure 8.2 (continued)

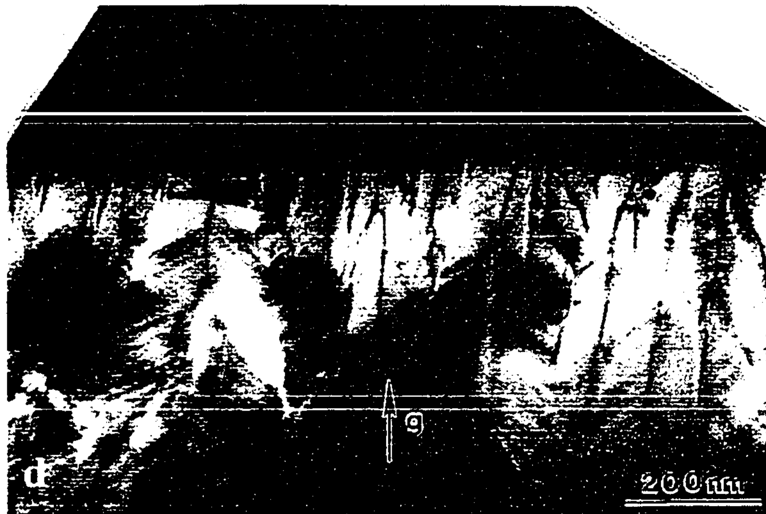

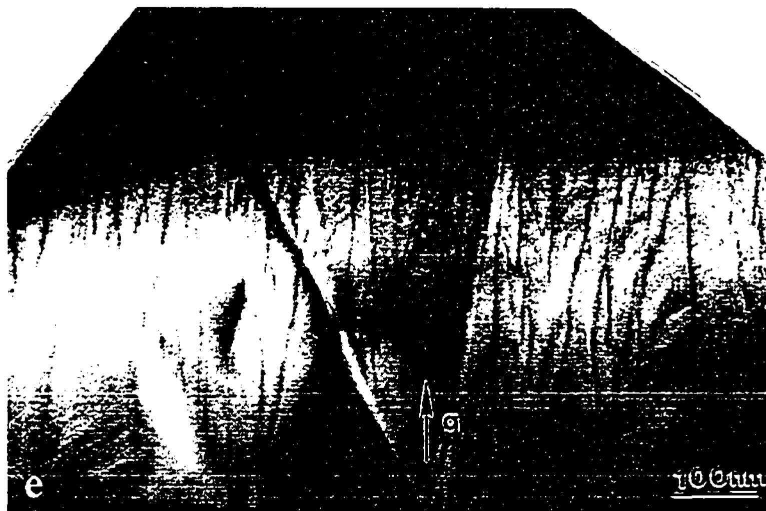

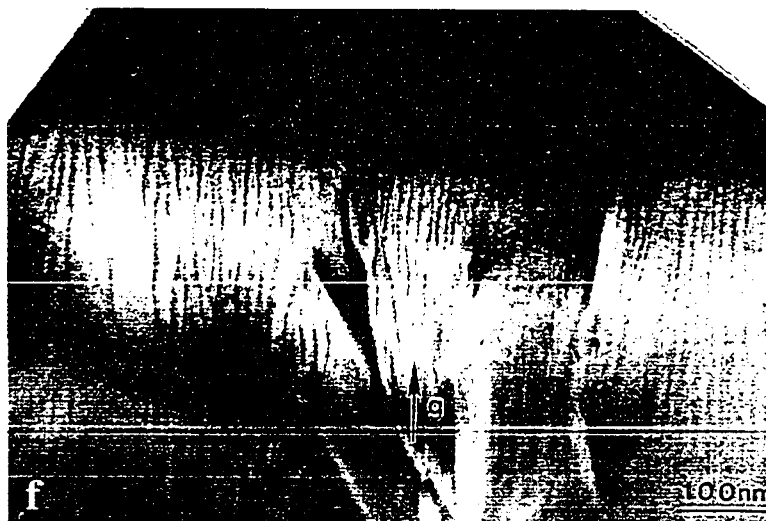

$[0\bar{1}1]$ cross-section TEM images of 2 μm thick, 0.6% tensile strained $In_{0.45}Ga_{0.55}As$ film. g = 200 for all images. Note that distances between the top of image and interface are 1 μm for (d), 1.6 μm for (e) and 2 μm for (f).

Figure 8.3

$[0\bar{1}1]$ cross-section TEM image of 0.5 μm thick, 2% tensile strained $In_{0.25}Ga_{0.75}As$ film, **g** = 200. (Compare to Fig.8.1 and 8.2, where evidence of compositional modulations was noted)

Figure 8.4

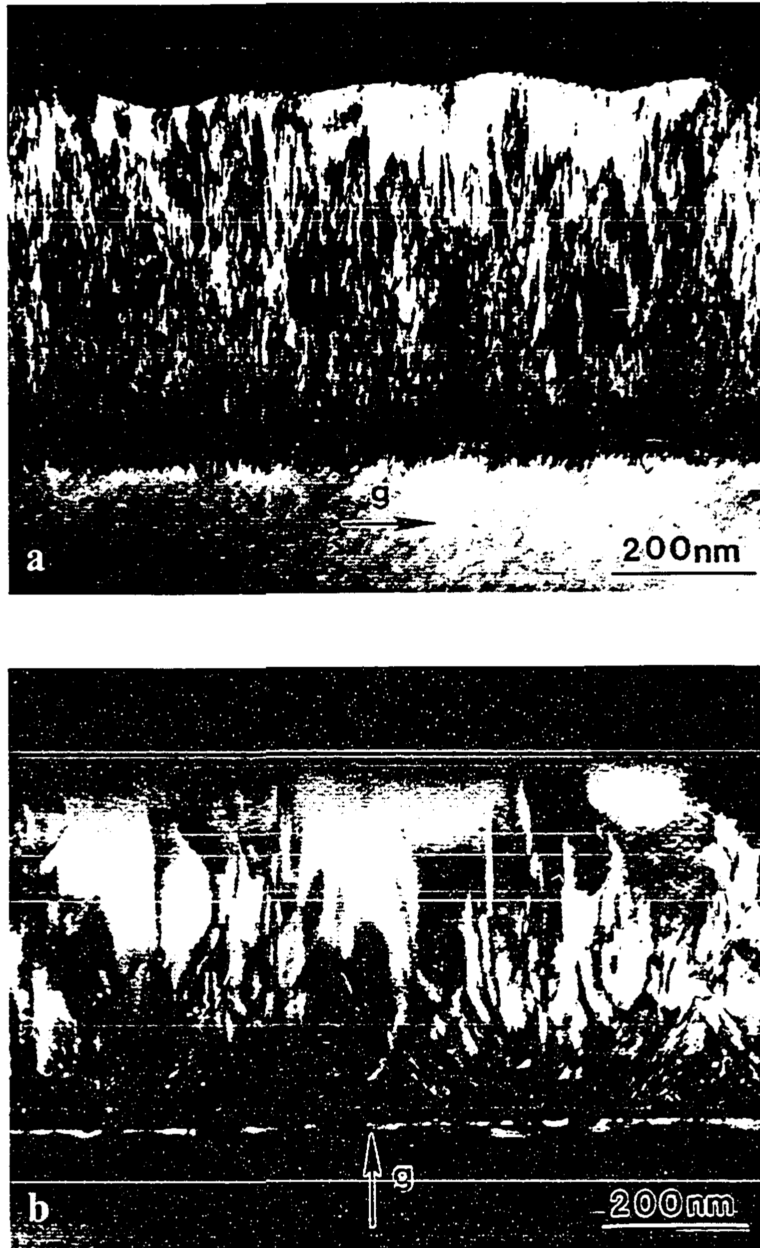

$[0\bar{1}1]$ cross-section TEM image of 0.5 μm thick, 2% tensile strained $In_{0.5}Ga_{0.5}As_{0.5}P_{0.5}$ film. (a) g = 022 and (b) g = 200.

0.5 μm thick, 2% tensile strained quaternary $In_{0.5}Ga_{0.5}As_{0.5}P_{0.5}$ film is not faceted, but undulated. Figure 8.5 compares AFM images of the surfaces of the 0.5 μm thick, 2% tensile strained ternary $In_{0.25}Ga_{0.75}As$ and quaternary $In_{0.5}Ga_{0.5}As_{0.5}P_{0.5}$ films. A faceted surface along one of the <011> direction is clearly visible in ternary InGaAs film (Fig.8.5a), while the surface is undulated along both <011> directions in the quaternary InGaAsP film (Fig.8.5b).

8.2 Application of the TEM to composition modulation contrast in III-V compound semiconductors

As discussed in Chapter 3, two beam diffraction theory shows that the intensity of the Bragg-diffracted beam (I_g) is proportional to the square of the structure factor (F_g), i.e.

$$I_g \propto F_g^2 \qquad (8.2.1)$$

For III-V compound semiconductors with the zinc-blende structure, the structure factor of the 200 reflection is given by

$$F_{200}(\mathrm{III-V}) = 4\left(f_v - f_{III}\right) \qquad (8.2.2)$$

where f_V and f_{III} are the atomic scattering amplitudes of group V and III elements respectively.

For an $In_{1-x}Ga_xAs$ alloy, the possible decomposition is

$$In_{1-x}Ga_xAs \rightarrow In_{1-x-\Delta x}Ga_{x+\Delta x}As + In_{1-x+\Delta x}Ga_{x-\Delta x}As \qquad (8.2.3)$$

If Δx is positive, the first term on the right hand side of equation (8.2.3) represents Ga-rich regions, while second term represents In-rich regions. On the other hand if Δx is negative, the first term on the right hand side of equation (8.2.3) represents In-rich, the second term Ga-rich regions. The structure factors are given by

$$F_{200}\left(In_{1-x}Ga_xAs\right) = 4\left[f_{As} - (1-x)f_{In} - xf_{Ga}\right] \qquad (8.2.4)$$

Figure 8.5

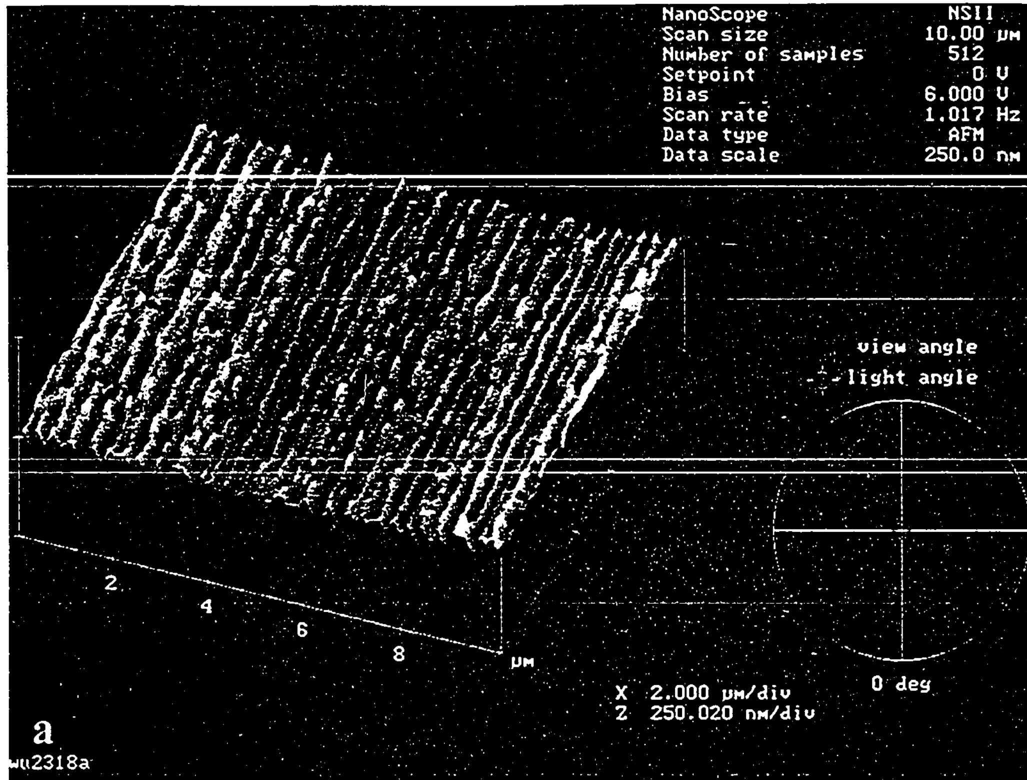

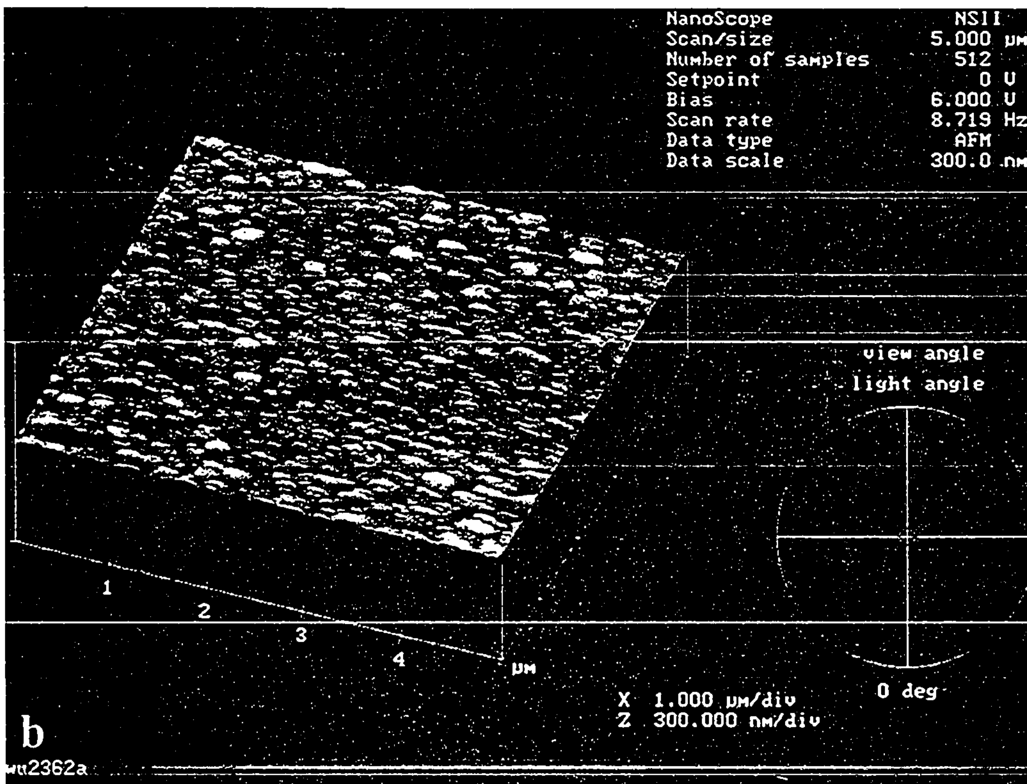

AFM images showing different surface morphologies of 0.5 µm thick, 2% tensile strained layers of $In_{0.25}Ga_{0.75}As$ (a), and $In_{0.5}Ga_{0.5}As_{0.5}P_{0.5}$ (b).

and

$$F_{200}\left(In_{1-x-\Delta x}Ga_{x+\Delta x}As\right) = 4\left[f_{As} - (1 - x - \Delta x)f_{In} - (x + \Delta x)f_{Ga}\right] \quad (8.2.5)$$

Therefore

$$\Delta F_{200} = \text{equation}(8.2.4) - \text{equation}(8.2.5) = 4\Delta x\left(f_{Ga} - f_{In}\right) \quad (8.2.6)$$

Equation (8.2.6) shows that contrast difference in the ternary alloy with **g** = 200 will depend on (f_{Ga}-f_{In}) and the sign of Δx (Ga-rich or In-rich).

The values of the atomic scattering amplitude of In, Ga, As and P at $\theta = \theta_B$ for **g** = 200 are listed in Table 8.1 (Williams and Carter 1996). The TEM images were taken at 120 kV, but the values in Table 8.1 can be used for qualitative discussion. These same values have also been used for the case where **g** = 022 in the end of this section.

Table 8.1 The atomic scattering amplitude at $\theta = \theta_B$ for **g** = 200 at 100 kV

Element	P	Ga	As	In
F(θ) (Å)	2.59	3.64	4.07	5.70

It is clear that there is a significant difference between f_{In} and f_{Ga}. Therefore, according to equation (8.2.6), the contrast from the Ga-rich and In-rich regions is black or white relative to the InGaAs background contrast. This is the composition modulation contrast seen in Fig.8.1 and 8.2, and agrees with the EDS analysis of composition fluctuations of $In_{1-x}Ga_xAs$ film reported by Okada *et al.* (1997): i.e. Ga-rich in the peak and In-rich in the valley regions.

For quaternary $In_{1-x}Ga_xAs_yP_{1-y}$ alloy, the possible decomposition is

$$In_{1-x}Ga_xAs_yP_{1-y} \rightarrow In_{1-x-\Delta x}Ga_{x+\Delta x}As_{y+\Delta y}P_{1-y-\Delta y} + In_{1-x+\Delta x}Ga_{x-\Delta x}As_{y-\Delta y}P_{1-y+\Delta y} \quad (8.2.7)$$

If Δx is positive and Δy is negative, the first term on the right hand side of equation (8.2.7) represents GaP-rich, the second term InAs-rich regions. While if Δx is negative and Δy is

positive, the first term on the right hand side of equation (8.2.7) represents InAs-rich, the second term GaP-rich regions. The structure factors are given by

$$F_{200}\left(In_{1-x}Ga_xAs_yP_{1-y}\right) = 4\left[yf_{As} + (1-y)f_P - xf_{Ga} - (1-x)f_{In}\right] \tag{8.2.8}$$

and

$$F_{200}\left(In_{1-x-\Delta x}Ga_{x+\Delta x}As_{y+\Delta y}P_{1-y-\Delta y}\right)$$
$$= 4\left[(y+\Delta y)f_{As} + (1-y-\Delta y)f_P - (x+\Delta x)f_{Ga} - (1-x-\Delta x)f_{In}\right] \tag{8.2.9}$$

Therefore

$$\Delta F_{200} = \text{equation}(8.2.8) - \text{equation}(8.2.9) = 4\left[\Delta y\left(f_P - f_{As}\right) + \Delta x\left(f_{Ga} - f_{In}\right)\right] \tag{8.2.10}$$

For the quaternary alloy $In_{0.5}Ga_{0.5}As_{0.5}P_{0.5}$ in this study, the PL results of Lapierre *et al.* (1996) suggest that

$$\Delta y = -\Delta x \tag{8.2.11}$$

i.e. the decomposition leads to InAs and GaP rich regions.

Substituting equation (8.2.11) into equation (8.2.10) leads to

$$\Delta F_{200} = 4\Delta x\left[\left(f_{As} - f_{In}\right) - \left(f_P - f_{Ga}\right)\right] \tag{8.2.12}$$

Equation (8.2.12) shows that any contrast difference in the quaternary alloy with **g** =200 will depend on $\left[\left(f_{As} - f_{In}\right) - \left(f_P - f_{Ga}\right)\right]$ and the sign of Δx (GaP-rich or InAs-rich). The difference between $\left(f_{As} - f_{In}\right)$ and $\left(f_P - f_{Ga}\right)$ is not significant according to Table 8.1. This is probably the reason for the poor composition modulation contrast with **g** = 200 shown in Fig.8.4b.

The structure factor of the 022 reflection is given by

$$F_{022}(III-V) = 4(f_V + f_{III}) \quad (8.2.13)$$

Therefore,

$$F_{022}(In_{1-x}Ga_xAs_yP_{1-y}) = 4[yf_{As} + (1-y)f_P + xf_{Ga} + (1-x)f_{In}] \quad (8.2.14)$$

and

$$F_{022}(In_{1-x-\Delta x}Ga_{x+\Delta x}As_{y+\Delta y}P_{1-y-\Delta y})$$
$$= 4[(y+\Delta y)f_{As} + (1-y-\Delta y)f_P + (x+\Delta x)f_{Ga} + (1-x-\Delta x)f_{In}] \quad (8.2.15)$$

Thus

$$\Delta F_{022} = \text{equation}(8.2.14) - \text{equation}(8.2.15) = 4[\Delta y(f_P - f_{As}) - \Delta x(f_{Ga} - f_{In})] \quad (8.2.16)$$

Substituting equation (8.2.11) into equation (8.2.16) leads to

$$\Delta F_{022} = 4\Delta x[(f_{As} + f_{In}) - (f_P + f_{Ga})] \quad (8.2.17)$$

Equation (8.2.17) shows that the contrast difference in the quaternary alloy with **g** = 022 will depend on $[(f_{As} + f_{In}) - (f_P + f_{Ga})]$ and the sign of Δx (GaP-rich or InAs-rich). According to Table 8.1, the difference between $(f_P + f_{Ga})$ and $(f_{As} + f_{In})$ (equation (8.2.17) for 022 diffraction) is much larger than that between $(f_{As} - f_{In})$ and $(f_P - f_{Ga})$ (equation (8.2.12) for 200 diffraction). Therefore better composition modulation contrast is expected with **g** = 022 as shown in Fig.8.4a. Additional TEM contrast associated with the composition modulation aligned normal to the [011] direction with **g** = 022 may be due to the strain between the two separated regions because **g** = 022 is parallel to [011] direction, while there is no contrast due to the strain with **g** = 200 since **g** = 200 is perpendicular to [011] direction.

8.3 Composition modulation and surface faceting

Several factors may play important roles in composition modulation behavior in $In_{1-x}Ga_xAs_yP_{1-y}$ heteroepitaxial strained layers: the sign and magnitude of the strain field in the layer, the thermodynamic driving force for decomposition (e.g the alloy composition in relation to the position of the chemical spinodal), and the rate of growth of the film (Guyer and Voorhees 1995). The origin of the composition modulation in the present study appears to be dependent on the position of the composition of the film with respect to the chemical spinodal. The alloy compositions of $In_{0.5}Ga_{0.5}As_{0.5}P_{0.5}$ (2% tensile strain), $In_{0.45}Ga_{0.55}As$ (0.6% tensile strain), and $In_{0.53}Ga_{0.47}As$ (lattice-matched) lie within the chemical spinodal at growth temperature 480°C (see Fig.1.1), and this is believed to be responsible for the fine scale composition modulation in these films. No composition modulation was observed in the 2% tensile strained $In_{0.25}Ga_{0.75}As$ film because the composition of this film lies outside the chemical spinodal at 480°C (Fig.1.1). The magnitude of the strain plays little role on the initial fine scale composition modulation.

As discussed in Chapter 2, surface morphological instability is one of the strain relaxation mechanisms in strained films (Srolovitz 1989; Grilhe 1993; Okada *et al.* 1997). In this study, a faceted surface was observed in both 0.6% and 2% tensile strained, 0.5 μm thick ternary InGaAs films (Figs.8.2b, 8.3 and 8.5a), while the surface is not faceted for the 0.5 μm thick, 2% tensile strained quaternary InGaAsP film (Fig.8.5b). The reason for this phenomenon is unclear. The wavelength of surface faceting is almost the same for 0.5 μm thick, 0.6% and 2% tensile strained InGaAs films although the theory predicts that the wavelength of surface faceting depends on the magnitude of the strain of the film (Okada *et al.* 1997). This can probably be explained because part of the strain was relieved by

microtwins, misfit dislocations, and cracking in the 2% tensile strain film (see Chapters 4 and 6).

For the 0.6% tensile strained $In_{0.45}Ga_{0.55}As$ film with a faceted growth surface, the composition modulation scaled with the size of the facets, i.e. composition modulation and surface faceting are coupled as previously shown by Okada *et al.* (1997). For the 2% tensile strained $In_{0.5}Ga_{0.5}As_{0.5}P_{0.5}$ film with no faceted growth surface, and the fine scale composition modulation with wavelength about 10 nm remains for the whole film. For the 2 μm thick, 0.6% tensile strained $In_{0.45}Ga_{0.55}As$ film, considerable plastic strain relaxation has occurred after the film thickness exceeds 1 μm. Microtwins and misfit dislocations can be seen in this film (Fig.8.6). As the strain is relieved with further film growth, the driving force for the surface faceting is reduced, thus the scaling of the composition modulation is diminished. As a result of this process, the fine scale composition modulation re-appears near the top of this film, almost identical to that found in the first stage of the film growth. Both surface faceting and the compositional modulations associated with it are seen to be mutually dependent on the stresses in the film, as well as the overall film composition.

Figure 8.6

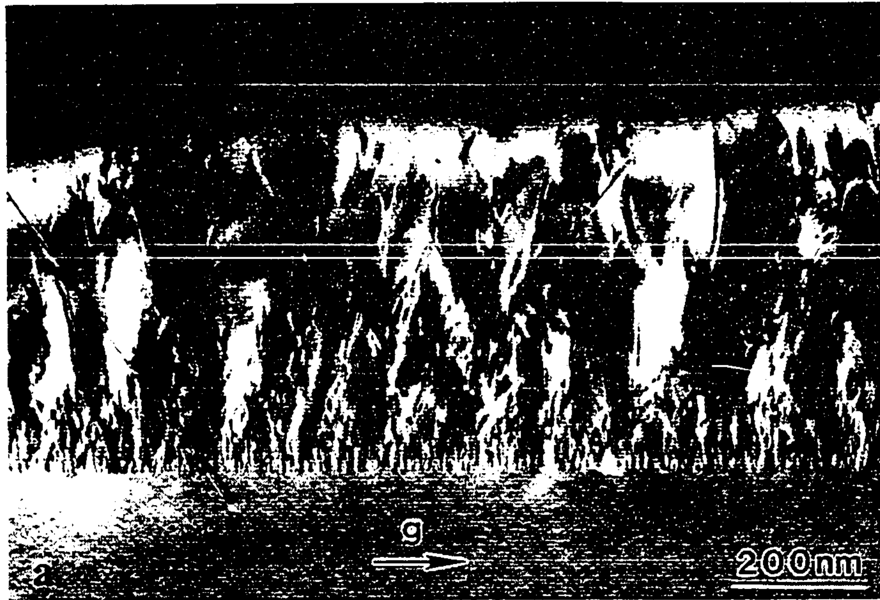

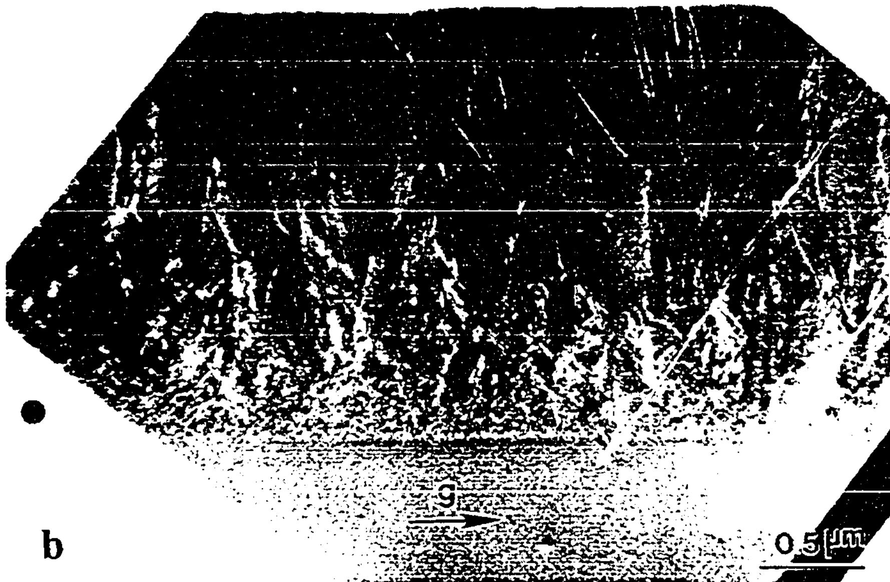

$[0\bar{1}1]$ cross-section TEM images of 2 μm thick, 0.6% tensile strained $In_{0.45}Ga_{0.55}As$ film showing microtwins and dislocations. (a) **g** = 022 DF, and (b) **g** = 022 WBDF.

Chapter 9

Summary and conclusions

In the present thesis, strain relaxation mechanisms were studied in $In_{1-x}Ga_xAs_yP_{1-y}$ heteroepitaxial films grown on (100) InP substrates using gas-source molecular beam epitaxy (MBE). Transmission electron microscopy (TEM) was extensively used to characterize the film growth related phenomena such as cracks, misfit dislocations, microtwins, surface morphology and composition modulation. Other microstructural characterization techniques used in this study were atomic force microscopy (AFM) and scanning electron microscopy (SEM).

Strain relief in 2% tensile strained $In_{0.25}Ga_{0.75}As$ and $In_{0.72}Ga_{0.28}P$ films is highly anisotropic. In the first stages of film growth, the strain along $[0\bar{1}1]$ was relieved by cracking on $(0\bar{1}1)$, while it occurred by (111) and $(\bar{1}11)$ twinning in the orthogonal [011] direction. In the $In_{0.25}Ga_{0.75}As$ film cracking was a transitory phenomenon. 10 and 500 nm thick films were crack free, while a decreasing crack density was observed in the film thickness range from 20 to 200 nm. The critical film thickness for cracking (~ 20 nm) corresponded to a condition where the total energy change (elastic and surface energy) was zero. Crack healing was observed in the 500 nm thick film. This was accompanied by increased dislocation activity relieving the misfit along $[0\bar{1}1]$. Strain relief in this direction (by dislocation activity) must reduce the residual elastic stress acting on the $(0\bar{1}1)$ cracks, so that crack healing by surface diffusion of atoms to the sharp tip of the crack becomes a competitive process. Cracks were observed to penetrate into the substrate and deviate from an $(0\bar{1}1)$ to $(1\bar{1}1)$ or $(\bar{1}\bar{1}1)$ planes. A critical stress intensity argument was developed to explain substrate cracking.

In the $In_{0.72}Ga_{0.28}P$ film, the average value of the ratio of crack opening displacement to normal surface displacement associated with crack was found to be 3.2 by AFM studies. A dislocation analogue for a surface crack was developed to successfully account for this value.

In $In_{0.25}Ga_{0.75}As$ film, 90° partial dislocations were found to form prior to the formation of cracks and 60° dislocations, consistent with the critical thickness and nucleation calculations developed in Chapter 6. Elastic strain energy computations show that 90° partial dislocations also provide the most effective relief of elastic strain energy for a film with smaller thickness, while cracks are the most effective strain relaxation mechanism for thicker films. In addition, the twin thickness is found to increase with an increase in the film thickness. The latter experimental result has also been theoretically predicted.

The role of the free surface in determining the equilibrium position of misfit dislocations in thin epitaxial films was studied based on a force argument. When the film is softer than the substrate, the core of the dislocation is always predicted to lie close to the interface. On the other hand, when the film is elastically stiffer than the substrate, the core of the dislocation is predicted to lie at some distance from the interface in the softer substrate. This explains the experimental observations in this study – the 90° partial dislocations bounded by stacking faults were frequently observed to locate inside the InP substrate over a range of a few hundred angstroms.

The origin of the composition modulation in $In_{1-x}Ga_xAs_yP_{1-y}$ films can be associated with the chemical spinodal in this alloy. Films with compositions lying within the chemical spinodal show fine scale composition modulation contrast. Clear correlation was found between the scaling of composition modulation and strain-induced surface faceting. The composition modulation was found to scale with the size of facets.

Appendix

The interaction of dislocations with the interface and free surface

Consider first an infinite isotropic elastic solid of shear modulus μ_s for $y > 0$, μ_f for $y < 0$, and assume $\nu_s = \nu_f = \nu$. An edge dislocation **b** located at (0,d) (Fig.A1) lies a slip plane making an angle φ with the interface. **b** can be resolved into two components $\mathbf{b}_x$ and $\mathbf{b}_y$ as shown in Fig.A1, following

$$\mathbf{b} = \mathbf{b}_x + \mathbf{b}_y \qquad \text{(A1)}$$

where $b_x = b\cos\varphi$, and $b_y = b\sin\varphi$.

Then the stress field of **b** is the superposition of the stress fields of $\mathbf{b}_x$ and $\mathbf{b}_y$.

The stress field of $\mathbf{b}_x$ in the two regions is as follows (Mura 1968):

In the region $y > 0$,

$$\sigma_{xx} = \frac{\mu_s b_x}{4\pi(1-\nu)}\left\{\frac{6(y-d)}{x^2+(y-d)^2} - \frac{4(y-d)^3}{\left[x^2+(y-d)^2\right]^2} - (5A+B)\frac{y+d}{x^2+(y+d)^2} + 4A\frac{(y+d)^3}{\left[x^2+(y+d)^2\right]^2}\right\}$$

$$+\frac{\mu_s b_x}{4\pi(1-\nu)}\left\{2Ad\left[-\frac{2}{x^2+(y+d)^2} + \frac{16(y+d)^2}{\left[x^2+(y+d)^2\right]^2} - \frac{16(y+d)^4}{\left[x^2+(y+d)^2\right]^3} - \frac{12d(y+d)}{\left[x^2+(y+d)^2\right]^2} + \frac{16d(y+d)^3}{\left[x^2+(y+d)^2\right]^3}\right]\right\}$$

$$\sigma_{yy} = \frac{\mu_s b_x}{4\pi(1-\nu)}\left\{-\frac{2(y-d)}{x^2+(y-d)^2} + \frac{4(y-d)^3}{\left[x^2+(y-d)^2\right]^2} + (A+B)\frac{y+d}{x^2+(y+d)^2} - 4A\frac{(y+d)^3}{\left[x^2+(y+d)^2\right]^2}\right\}$$

$$+\frac{\mu_s b_x}{4\pi(1-\nu)}\left\{2Ad\left[-\frac{2}{x^2+(y+d)^2} - \frac{8(y+d)^2}{\left[x^2+(y+d)^2\right]^2} + \frac{16(y+d)^4}{\left[x^2+(y+d)^2\right]^3} + \frac{12d(y+d)}{\left[x^2+(y+d)^2\right]^2} - \frac{16d(y+d)^3}{\left[x^2+(y+d)^2\right]^3}\right]\right\}$$

Figure A1

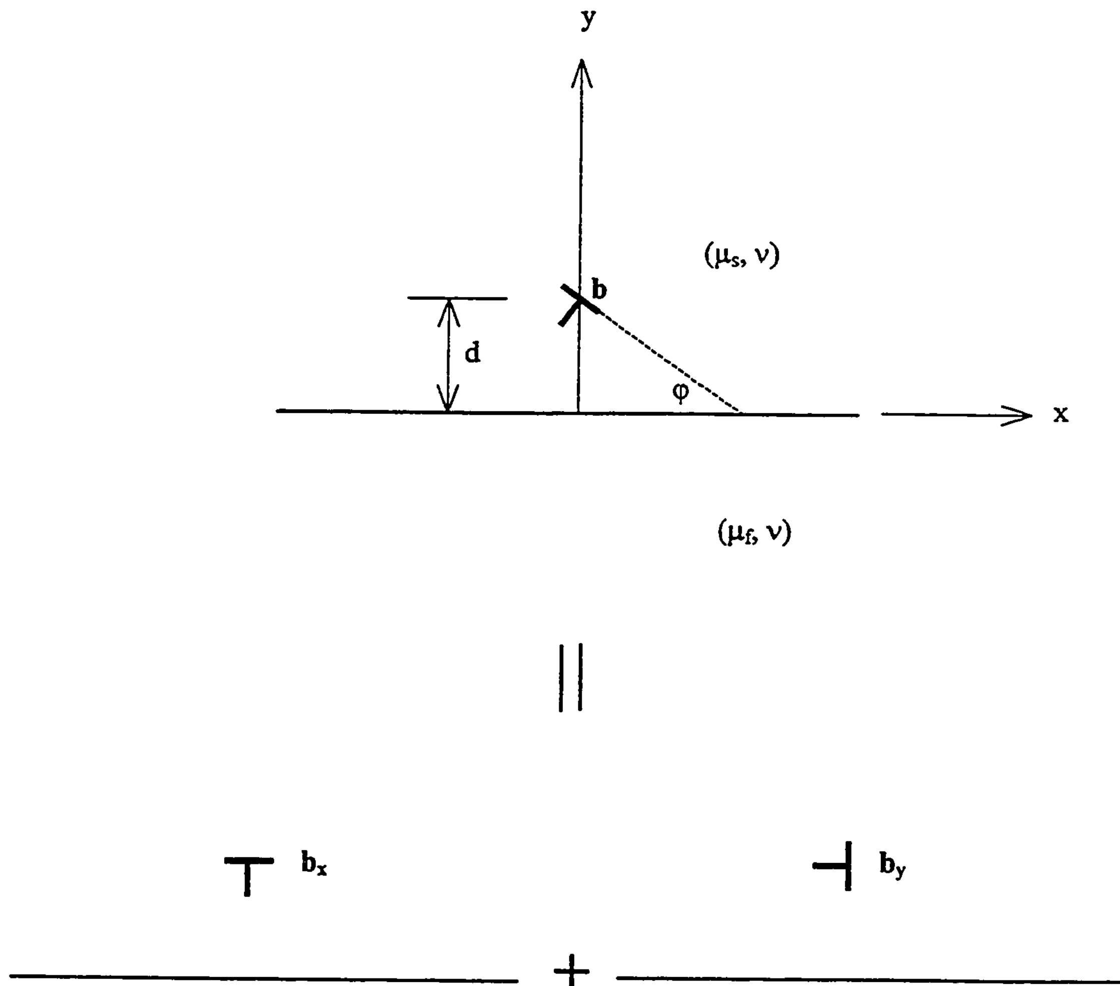

A dislocation **b** near an interface. Burgers vector **b** resolved into two components $\mathbf{b}_x$ and $\mathbf{b}_y$. Note that the dislocation line direction **l** is taken out of the paper.

$$\sigma_{xy} = \frac{\mu_s b_x}{4\pi(1-\nu)}\left\{-\frac{2x}{x^2+(y-d)^2}+\frac{4x(y-d)^2}{\left[x^2+(y-d)^2\right]^2}+(A+B)\frac{x}{x^2+(y+d)^2}-4Ax\frac{(y+d)^2}{\left[x^2+(y+d)^2\right]^2}\right\}$$

$$+\frac{\mu_s b_x}{4\pi(1-\nu)}\left\{2Ad\left[-\frac{4x(y+d)}{\left[x^2+(y+d)^2\right]^2}+\frac{16x(y+d)^3}{\left[x^2+(y+d)^2\right]^3}+\frac{4dx}{\left[x^2+(y+d)^2\right]^2}-\frac{16dx(y+d)^2}{\left[x^2+(y+d)^2\right]^3}\right]\right\}$$

(A2)

In the region $y < 0$,

$$\sigma_{xx} = \frac{\mu_s b_x}{4\pi(1-\nu)}\left\{\frac{(6-5B-A)(y-d)}{x^2+(y-d)^2}-\frac{4(1-B)(y-d)^3}{\left[x^2+(y-d)^2\right]^2}-2d(B-A)\left[\frac{1}{x^2+(y-d)^2}-\frac{2(y-d)^2}{\left[x^2+(y-d)^2\right]^2}\right]\right\}$$

$$\sigma_{yy} = \frac{\mu_s b_x}{4\pi(1-\nu)}\left\{-\frac{(2-A-B)(y-d)}{x^2+(y-d)^2}+\frac{4(1-B)(y-d)^3}{\left[x^2+(y-d)^2\right]^2}+2d(B-A)\left[\frac{1}{x^2+(y+d)^2}-\frac{2(y-d)^2}{\left[x^2+(y+d)^2\right]^2}\right]\right\}$$

$$\sigma_{xy} = \frac{\mu_s b_x}{4\pi(1-\nu)}\left\{-\frac{(2-A-B)x}{x^2+(y-d)^2}+\frac{4(1-B)x(y-d)^2}{\left[x^2+(y-d)^2\right]^2}-4d(B-A)\left[\frac{x(y-d)}{\left[x^2+(y+d)^2\right]^2}\right]\right\}$$

(A3)

where $A = \frac{1-\Gamma}{1+\kappa\Gamma}$, $B = \frac{\kappa(1-\Gamma)}{\kappa+\Gamma}$, $\kappa = 3-4\nu$, and $\Gamma = \frac{\mu_f}{\mu_s}$.

If $\mu_s = \mu_f$, $A = B = 0$, and equations (A2) and (A3) become

$$\sigma_{xx} = \frac{\mu_s b_x}{2\pi(1-\nu)}\left\{\frac{(y-d)\left[3x^2+(y-d)^2\right]}{\left[x^2+(y-d)^2\right]^2}\right\}$$

$$\sigma_{yy} = -\frac{\mu_s b_x}{2\pi(1-\nu)}\left\{\frac{(y-d)\left[x^2-(y-d)^2\right]}{\left[x^2+(y-d)^2\right]^2}\right\}$$

$$\sigma_{xy} = -\frac{\mu_s b_x}{2\pi(1-\nu)}\left\{\frac{x\left[x^2-(y-d)^2\right]}{\left[x^2+(y-d)^2\right]^2}\right\} \qquad \text{(A4)}$$

which is the stress field of an edge dislocation in the infinite homogenous media.

At x = 0, y = d, i. e. at the point (0,d), equation (A2) becomes

$$\sigma_{xx} = \frac{\mu_s b_x}{4\pi(1-\nu)d}\left[-\frac{1}{2}(A+B)\right]$$

$$\sigma_{yy} = \frac{\mu_s b_x}{4\pi(1-\nu)d}\left[\frac{1}{2}(A+B)\right]$$

$$\sigma_{xy} = 0 \qquad \text{(A5)}$$

The stress field of $\mathbf{b}_y$ in the two regions is as follows (Mura 1968):

In the region y > 0,

$$\sigma_{xx} = \frac{\mu_s b_y}{4\pi(1-\nu)}\left\{-\frac{2x}{x^2+(y-d)^2}+\frac{4(y-d)^2 x}{\left[x^2+(y-d)^2\right]^2}+(3A-B)\frac{x}{x^2+(y+d)^2}-4A\frac{(y+d)^2 x}{\left[x^2+(y+d)^2\right]^2}\right\}$$

$$+\frac{\mu_s b_y}{4\pi(1-\nu)}\left\{-2Ad\left[-\frac{12(y+d)x}{x^2+(y+d)^2}+\frac{16(y+d)^3 x}{\left[x^2+(y+d)^2\right]^3}+\frac{4dx}{\left[x^2+(y+d)^2\right]^2}-\frac{16d(y+d)^2 x}{\left[x^2+(y+d)^2\right]^3}\right]\right\}$$

$$\sigma_{yy} = \frac{\mu_s b_y}{4\pi(1-\nu)}\left\{-\frac{x}{x^2+(y-d)^2}-\frac{4(y-d)^2 x}{\left[x^2+(y-d)^2\right]^2}+(A+B)\frac{x}{x^2+(y+d)^2}+4A\frac{(y+d)^2 x}{\left[x^2+(y+d)^2\right]^2}\right\}$$

$$+\frac{\mu_s b_y}{4\pi(1-\nu)}\left\{-2Ad\left[\frac{4(y+d)x}{x^2+(y+d)^2}-\frac{16(y+d)^3 x}{\left[x^2+(y+d)^2\right]^3}-\frac{4dx}{\left[x^2+(y+d)^2\right]^2}+\frac{16d(y+d)^2 x}{\left[x^2+(y+d)^2\right]^3}\right]\right\}$$

$$\sigma_{xy} = \frac{\mu_s b_y}{4\pi(1-\nu)}\left\{-\frac{2(y-d)}{x^2+(y-d)^2}+\frac{4(y-d)^3}{\left[x^2+(y-d)^2\right]^2}+(3A-B)\frac{y+d}{x^2+(y+d)^2}-4A\frac{(y+d)^3}{\left[x^2+(y+d)^2\right]^2}\right\}$$

$$+\frac{\mu_s b_y}{4\pi(1-\nu)}\left\{-2Ad\left[\frac{2}{x^2+(y+d)^2}-\frac{16(y+d)^2}{\left[x^2+(y+d)^2\right]^2}+\frac{16(y+d)^4}{\left[x^2+(y+d)^2\right]^3}+\frac{12(y+d)d}{\left[x^2+(y+d)^2\right]^2}-\frac{16d(y+d)^3}{\left[x^2+(y+d)^2\right]^3}\right]\right\}$$

(A6)

In the region $y < 0$,

$$\sigma_{xx} = \frac{\mu_s b_y}{4\pi(1-\nu)}\left\{\frac{(-2+3B-A)x}{x^2+(y-d)^2} + \frac{4(1-B)x(y-d)^2}{\left[x^2+(y-d)^2\right]^2} - 4d(B-A)\frac{x(y-d)}{\left[x^2+(y-d)^2\right]^2}\right\}$$

$$\sigma_{yy} = \frac{\mu_s b_y}{4\pi(1-\nu)}\left\{-\frac{(2-A-B)x}{x^2+(y-d)^2} - \frac{4(1-B)x(y-d)^2}{\left[x^2+(y-d)^2\right]^2} + 4d(B-A)\frac{x(y-d)}{\left[x^2+(y-d)^2\right]^2}\right\}$$

$$\sigma_{xy} = \frac{\mu_s b_y}{4\pi(1-\nu)}\left\{-\frac{(2+3B-A)(y-d)}{x^2+(y-d)^2} + \frac{4(1-B)(y-d)^3}{\left[x^2+(y-d)^2\right]^2} + 2d(B-A)\left[\frac{1}{x^2+(y-d)^2} - \frac{2(y-d)^2}{\left[x^2+(y+d)^2\right]^2}\right]\right\}$$

(A7)

If $\mu_s = \mu_f$, $A = B = 0$, and equations (A6) and (A7) become

$$\sigma_{xx} = -\frac{\mu_s b_y x}{2\pi(1-\nu)}\left\{\frac{x^2-(y-d)^2}{\left[x^2+(y-d)^2\right]^2}\right\}$$

$$\sigma_{yy} = -\frac{\mu_s b_y x}{2\pi(1-\nu)}\left\{\frac{x^2+3(y-d)^2}{\left[x^2+(y-d)^2\right]^2}\right\}$$

$$\sigma_{xy} = -\frac{\mu_s b_y (y-d)}{2\pi(1-\nu)}\left\{\frac{x^2-3(y-d)^2}{\left[x^2+(y-d)^2\right]^2}\right\} \quad \text{(A8)}$$

which is again the stress field of an edge dislocation in the infinite homogenous medium.

At $x = 0$, $y = d$, i. e. at the point (0,d), equation (A6) becomes

$$\sigma_{xx} = 0$$

$$\sigma_{yy} = 0$$

$$\sigma_{xy} = \frac{\mu b_y}{4\pi(1-\nu)d}\left[-\frac{1}{2}(A+B)\right] \quad \text{(A9)}$$

Superimposing equations (A5) and (A9) leads to the stress field of **b** at (0,d) as follows:

$$\sigma_{xx} = \frac{\mu_s b_x}{4\pi(1-\nu)d}\left[-\frac{1}{2}(A+B)\right] = \frac{\mu_s b\cos\varphi}{2\pi(1-\nu)}\frac{1}{2d}\left[-\frac{1}{2}(A+B)\right]$$

$$\sigma_{yy} = \frac{\mu_s b_x}{4\pi(1-\nu)d}\left[+\frac{1}{2}(A+B)\right] = \frac{\mu_s b\cos\varphi}{2\pi(1-\nu)}\frac{1}{2d}\left[+\frac{1}{2}(A+B)\right] \quad \text{(A10)}$$

$$\sigma_{xy} = \frac{\mu_s b_y}{4\pi(1-\nu)d}\left[-\frac{1}{2}(A+B)\right] = \frac{\mu_s b\sin\varphi}{2\pi(1-\nu)}\frac{1}{2d}\left[-\frac{1}{2}(A+B)\right]$$

Since the dislocation slip and climb directions are of interest, a new co-ordinate system x',y' is established where x' direction is parallel to the dislocation slip direction and y' direction is parallel to the dislocation climb direction. By the transformation of stress conponents, we have (Dieter, 1988)

$$\sigma_{x'x'} = \frac{\sigma_{xx}+\sigma_{yy}}{2} + \frac{\sigma_{xx}-\sigma_{yy}}{2}\cos 2\varphi + \sigma_{xy}\sin 2\varphi$$

$$\sigma_{y'y'} = \frac{\sigma_{xx}+\sigma_{yy}}{2} - \frac{\sigma_{xx}-\sigma_{yy}}{2}\cos 2\varphi - \sigma_{xy}\sin 2\varphi \quad \text{(A11)}$$

$$\sigma_{x'y'} = \frac{\sigma_{yy}-\sigma_{xx}}{2}\sin 2\varphi + \sigma_{xy}\cos 2\varphi$$

Substituting equation (A10) into (A11) gives

$$\sigma_{x'x'} = \frac{\mu_s b}{2\pi(1-\nu)}\frac{1}{2d}\left[-\frac{1}{2}(A+B)\right]\cos\varphi$$

$$\sigma_{y'y'} = \frac{\mu_s b}{2\pi(1-\nu)}\frac{1}{2d}\left[+\frac{1}{2}(A+B)\right]\cos\varphi \quad \text{(A12)}$$

$$\sigma_{x'y'} = \frac{\mu_s b}{2\pi(1-\nu)}\frac{1}{2d}\left[-\frac{1}{2}(A+B)\right](-\sin\varphi)$$

Now consider a semi-infinite isotropic solid of modulus μ_s for $y > 0$, and μ_f for $-h < y$

< 0, having $\nu_s = \nu_f = \nu$, with a free surface at $y = -h$. An edge dislocation **b** located at (0,d) lies on a slip plane making angle φ with the interface. In this case, the force acting on the dislocation due to the interface and free surface arises from the climb force $\sigma_{x'x'}$ and the glide force $\sigma_{x'y'}$, and can be described by an infinite set of image dislocations located at (0,y) with strengths as follows (Head 1953b):

Position of image: value of y	Strength of image	$\sigma_{x'x'}$	$\sigma_{x'y'}$
d	m	$\frac{\mu_s b}{2\pi(1+\nu)}\frac{1}{d+d}m\cos\varphi$	$\frac{\mu_s b}{2\pi(1+\nu)}\frac{1}{d+d}m(-\sin\varphi)$
d+2h	$-(1-m^2)$	$\frac{\mu_s b}{2\pi(1+\nu)}\frac{1}{d+d+2h}\left[-(1-m^2)\right]\cos\varphi$	$\frac{\mu_s b}{2\pi(1+\nu)}\frac{1}{d+d+2h}\left[-(1-m^2)\right](-\sin\varphi)$
d+4h	$-(1-m^2)m$	$\frac{\mu_s b}{2\pi(1+\nu)}\frac{1}{d+d+4h}\left[-(1-m^2)m\right]\cos\varphi$	$\frac{\mu_s b}{2\pi(1+\nu)}\frac{1}{d+d+4h}\left[-(1-m^2)m\right](-\sin\varphi)$
d+6h	$-(1-m^2)m^2$	$\frac{\mu_s b}{2\pi(1+\nu)}\frac{1}{d+d+6h}\left[-(1-m^2)m^2\right]\cos\varphi$	$\frac{\mu_s b}{2\pi(1+\nu)}\frac{1}{d+d+6h}\left[-(1-m^2)m^2\right](-\sin\varphi)$
d+8h	$-(1-m^2)m^3$	$\frac{\mu_s b}{2\pi(1+\nu)}\frac{1}{d+d+8h}\left[-(1-m^2)m^3\right]\cos\varphi$	$\frac{\mu_s b}{2\pi(1+\nu)}\frac{1}{d+d+8h}\left[-(1-m^2)m^3\right](-\sin\varphi)$
Etc.	etc.	etc.	etc.

where $m = -\frac{1}{2}(A+B)$.

Therefore, the total force acting on the dislocation due to the free surface and interface is given by

$$F_c = \sum_{i=1}^{\infty}\sigma_{x'x',i}b = \frac{\mu_s b^2}{4\pi(1-\nu)d}\left[m-(1-m^2)\sum_{i=1}^{\infty}\frac{d}{d+ih}m^{i-1}\right]\cos\varphi \qquad \text{(A13)}$$

for the climb force, and

$$F_g = \sum_{i=1}^{\infty}\sigma_{x'y',i}b = \frac{\mu_s b^2}{4\pi(1-\nu)d}\left[m-(1-m^2)\sum_{i=1}^{\infty}\frac{d}{d+ih}m^{i-1}\right](-\sin\varphi) \qquad \text{(A14)}$$

for the glide force.

The total image force acting along the y direction for an edge dislocation lying in the substrate is given by:

$$F_y^{image} = F_c \cos\varphi + F_g \sin\varphi$$

$$= \frac{\mu_s b^2}{4\pi(1-\nu)d}\left[m - \left(1-m^2\right)\sum_{i=1}^{\infty}\frac{d}{d+ih}m^{i-1}\right]\cos 2\varphi \tag{A15}$$

A screw dislocation with Burgers vector **b** = (0,0,b) at (0,d) has a total image force due to the free surface and interface given by (Head 1953b)

$$F_s = \frac{\mu_s b^2}{4\pi d}\left[p - \left(1-p^2\right)\sum_{i=1}^{\infty}\frac{d}{d+ih}p^{i-1}\right] \tag{A16}$$

where $p = \frac{\Gamma - 1}{\Gamma + 1}$ with $\Gamma = \frac{\mu_f}{\mu_s}$.

From equations (A15) and (A16), we can easily obtain the total image force acting along the y direction for a mixed dislocation lying in the substrate as:

$$F_y^{image} = F_c \cos\varphi + F_g \sin\varphi + F_s$$

$$= \frac{\mu_s b^2 \sin^2\beta}{4\pi(1-\nu)d}\left[m - \left(1-m^2\right)\sum_{i=1}^{\infty}\frac{d}{d+ih}m^{i-1}\right]\cos 2\varphi + \frac{\mu_s b^2 \cos^2\beta}{4\pi d}\left[p - \left(1-p^2\right)\sum_{i=1}^{\infty}\frac{d}{d+ih}p^{i-1}\right] \tag{A17}$$

where β is the angle between the Burgers vector of the dislocation and the dislocation line. The same procedures can be followed for the case where the dislocation lies in the film rather than the substrate.

References

Adachi, S., 1982, *Appl. Phys. Lett.* **53**, 8775.

Besser, P. J., Mee, J. E., Elkins, P. E., and Heinz, D. M., 1971, *Mat. Res. Bull.*, **6**, 1111.

Beuth, J.L., 1992, *Int. J. Solids Structure,* **29**, 1657.

Chu, S.N.G., Nakahara, S., Strege, K.E., and Johnston, Jr., W.D., 1985, *J. Appl. Phys.*, **57**, 4610.

Cottrell, A. H., 1953, *"Dislocations and Plastic Flow in Crystal"*, Oxford University Press, Oxford.

Cullis, A.G., Pidduck, A.J., and Emeny, M.T., 1996, *J. Cryst. Growth.*, **158**, 15.

DeCooman, B. C., and Carter, C. B., 1989, *Acta Metall.*, **37**, 2765.

Dieguez, A., Vila, A., Cornet, A., Clark, S. A., Westwood, D. J., and Morante, J. R., 1997, *J. Vac. Sci. Technol..*, **A15**, 687.

Dieter, G.E., 1988, *"Mechanical Metallurgy"*, McGraw-Hill, New York.

Dundurs, J., and Sendeckyj, G.P., 1965, *J. Appl. Phys.*, **36**, 3353.

Dundurs, J., 1969, *J. Appl. Mech.,* **36**, 650.

Dunstan, D.J., 1997, *J. Mater. Sci.: Materials in Electronics.*, **8**, 337.

Dynna, M., Okada, T., and Weatherly, G.C., 1994, *Acta Mttall. Mater.*, **42**, 1661.

Dynna, M., and Weatherly, G. C., 1994, *J. Cryst. Growth*, **142**, 315.

Dynna, M., Marty, A., Gilles, B., and Patrat, G., 1997, *Acta Mater.* **45**, 257.

Dynna, M., and Marty, A., 1998, *Acta Mater.* **46**, 1087.

Eaglesham, D.J., and Cerullo, M., 1990, *Phys. Rev. Lett.*, **64**, 1943.

Frank, F. C., and van der Merwe., J. H., 1949, *Proc. R. Soc.*, **A198**, 216.

Frank, F. C., 1950, *Symp. On Plastic Deformation of Crystalline Solids*, Carnegie Inst. Of Technology, Pittsburgh.

Fitzgerald, E. A., Watson, G. P., Proano, R. E., Ast, D. G., Kirchner, P. D., Pettit, G. D., and Woodall, J. M., 1989, *J. Appl. Phys.*, **65**, 2220.
Gao, H., *J. Mech. Phys. Solids,* 1991, **39**, 443.

Gao, H., Zhang, L., Nix, W.D., Thompson, C.V., and Arzt, E., 1999, *Acta Mater.* **47**, 2865.

Gottschalk, H., Patzer, G., and Alexander, H., 1978, *Phys. Stat. Sol. (a)*, **45**, 207.

Grilhe, J., 1993, *Acta Metall. and Mater.*, **41**, 909.

Guha, S., Madhukar, A., and Rajkumar, K., 1990, *Appl. Phys. Lett.*, **57**, 2110.

Gutkin, M. Y., Militzer, M., Romanov, A. E., and Vladimirov, V. I., 1989, *Phys. Stat. Sol. (a)*, **113**, 337.

Guyer, J.E., and Voorhees, P.W., 1995, *Phys. Rev. Lett.*, **74**, 4031.

Head, A. K., 1953a, *Phil. Mag.*, **44**, 92.

Head, A. K., 1953b, *Proc. Phys. Soc.*, **66B**, 793.

Henoc, P., Izrael, A., Quillec, M., and Launois, H., 1982, *Appl. Phys. Lett.*, **40**, 963.

Hirsch, P., Howie, A., Nicholson, R., Pashley, D.W., and Whelan, M.J., 1977, *"Electron Microscopy of Thin Crystals"*, Kreiger, New York.

Hirth, J.P., and Lothe, J., 1982, "*Theory of Dislocations*, Wiley, New York.

Hottschalk, H., Patzer, G., and Alexander, H., 1978, *Phys. Stat. Sol. (a)*, **45**, 207.

Hull, R., and Bean, J.C., 1992, *Critical Reviews in Solid State and Materials Sciences*, **17**, 507

Hutchinson, J.W., and Suo, Z., 1991, *Advances in Applied Mechanics,* **29**, 63.

Jain, S.C., Gosling, T.J., Willis, J.R., Totterdell, D.H.J., and Bullough, R., 1992, *Phil. Mag.* A., **65**, 1151.

Knauss, D., and Mader, W., 1991, *Ultramicroscopy*, **37**, 247.

Kavanagh, K. L., Capano, M. A., Hobbs, L. W., Maree, P. M. J., Schaff, W., Mayer, J. W., Pettit, D., Woodall, J. M., Stroscio, J. A., Feenstra, R. M., and Barbour, J. C., 1988, *J. appl. Phys.*, **64**, 4843.

LaPierre,R.R., Okada,T., Robinson,B,J., Thompson,D.A., and Weatherly,G.C., 1995, *J. Cryst. Growth*, **155**, 1.

LaPierre,R.R., 1994, Master's thesis, McMaster University.

LaPierre, R.R., Okada, T., Robinson, B,J., Thompson, D.A., and Weatherly, G.C., 1996, *J. Cryst. Growth*, **158**, 6.

Lawn, B., *"Fracture of Brittle Solids"*, 1993, Cambridge University Press, Cambridge.

Mader, W., 1987, *Mater. Res. Soc. Symp. Proc.*, **82**, 403.

Mader, W., and Knauss, D. 1992, *Acta Metall. Mater.*, **40**, S207.

Matthews, J. W., and Klokholm, E., 1972, *Mat. Res. Bull.*, **7**, 213.

Matthews, J. W., and Blakeslee, A. E., 1974, *J. Cryst. Growth*, **27**, 118.

Matthews, J. W., and Blakeslee, A. E., 1975, *J. Cryst. Growth*, **29**, 273.

Matthews, J. W., Blakeslee, A. E., and Mader, S., 1976, *Thin Solid Film*, 33, 253.

Maree, P.M.J., Barbour, J.C., van der Veen, J.F., Kavanagh, K.L., Bulle-Lieuwma, C.W.T., and Viegers, M.P.A., 1987, *J. Appl. Phys.*, **62**, 4413.

Mura, T., 1968, *Advances in Materials Research*, Vol.3, Interscience, New York

Murray, R. T., Kiely, C. J., and Hopkinson, M., 1996, *Phil. Mag.*, **A74**, 383.

Murray, R. T., Hopkinson, M., and Kiely, C. J., 1997, *Ins. Phys. Conf. Ser.*, **153**, 425.

Nahory, R. E., Pollack, M. A., Johnston, Jr. W. D., and Barns, R. L., 1978, *Appl. Phys. Lett.*, **33**, 659.

Okada, T., Weatherly, G. C., and McComb, D. W., 1997, *J. Appl. Phys.*, **81**, 2185.

Olsen, G. H., Abrdham, M. S., and Zamerouski, T. J., 1974, *J. electrochem. Soc.*, **121**, 650.

Onabe, K., 1982, *Jpn. J. Appl. Phys.*, **21**, 797.

Perovic, D. D., Weatherly, G. C., and Houghton, D.C., 1991, *Phil. Mag.*, **64A**, 1.

Petruzzello, J. and Leys, M.R., 1988, *J. Appl. Phys.*, **53**, 2414.

Ponchet, A., Rocher, A., Ougazzaden, A., and Mircea, A. 1994, *J. Appl. Phys.*, **75**, 7881.

Ponchet, A., Le Corre, A., Godefroy, A., Salaun, S., and Poudouiec, A., 1995, *J. Cryst. Growth*, **153**, 71.

Prigogine, I., and Defay, R., 1954, *"Chemical thermodynamics"*, Longmans, Green and Co., Ltd., London.

Srolovitz, D. J., 1989, *Acta Metall.*, **37**, 621.

Stringfellow,G.B., 1982, *J. Cryst. Growth*, **58**, 194.

Synder, C.W., Orr, B.G., Kessler, D., and Sander, L.M., 1991, *Pyhs. Rev. Lett.*, **66**, 3032.

Tada, H., Paris, P.C., and Irwin, G.R., 1985, *"The Stress Analysis of Cracks Handbook"*, DelResearch, St. Louis, Missouri.

Thouless, M.D., 1990, *J. Am. Ceram. Soc.*, **73**, 2144.

Thouless, M.D. Olsson, E., and Gupta, A., 1992, *Acta metall. mater.*, **40**, 1287.

Tsuchiya, T., Taniwatrai, T., Komori, M., Tsuneta, R., and Kakibayashi, H., 1994, *Jpn. J. Appl. Phys.*, **33**, 230.

Tu, K-N., Mayer, J.W., and Feldman, L.C., 1992, *"Electronic Thin Film Science"*, Macmillan, New York.

Weeks, R., Dundurs, J., and Stippes, M., 1968, *Int. J. Engng. Sci.*, **6**, 365.

Wegscheider, W., Eberl, K., Cerva, H., and Oppolzer, H., 1989, *Appl. Phys. Lett.*, **55**, 448.

Wegscheider, W., Eberl, Abstreiter, G., Cerva, H., and Oppolzer, H., 1990, *Appl. Phys. Lett.*, **57**, 1496.

Williams, D.B., and Carter, C.B., 1996, *"Transmission Electron Microscopy"*, Plenum Press, New York.

Willis, J.R., Jain, S.C., and Bullough, R., 1990, *Phil. Mag.* A., **62**, 115.

Xie, Y.H., Gilmer, G.H., Roland, C., Silverman, P.J., Buratto, S.K., Cheng, J.Y., Fitzgerald, E.A., Kortan, A.R., Schuppler, S., Marcus, M.A. and Citrin, P.H., 1994, *Phys. Rev. Lett.*, **73**, 3006.

Ye, T., Suo, Z., and Evans, A.G., 1992, *Int. J. Solids Structure*, **29**, 2639.

Zory, Jr. P. S., 1993, "*Quantum well lasers*", Academic Press, Boston.

Zou, J., and Cockayne, D. J. H., 1993, *J. Appl. Phys.*, **74**, 925.